RICE UNIVERSITY

Respiratory Motion Correction Techniques in Positron Emission Tomography/Computed Tomography (PET/CT) Imaging

By

GUOPING CHANG

A THESIS SUBMITTED
IN PARTIAL FULFILLMENT OF THE
REQUIREMENTS FOR THE DEGREE

Doctor of Philosophy

APPROVED, THESIS COMMITTEE:

John W. Clark, Jr., Professor, Chair
Electrical and Computer Engineering

Kevin F. Kelly, Associate Professor
Electrical and Computer Engineering

Joe D. Warren, Professor
Computer Science

Osama R. Mawlawi, Associate Professor
Imaging Physics, The University of Texas
M.D. Anderson Cancer Center

HOUSTON, TEXAS
MAY 2010

ProQuest LLC
789 East Eisenhower Parkway
P.O. Box 1346
Ann Arbor, MI 48106-1346

Abstract

Respiratory Motion Correction Techniques in Positron Emission Tomography/Computed Tomography (PET/CT) Imaging

by

GUOPING CHANG

The aim of this thesis is to design, implement, and evaluate respiratory motion correction techniques that can overcome respiratory motion artifacts in PET/CT imaging. The thesis is composed of three main sections. The first section introduces a novel approach (free-breathing amplitude gating (FBAG) technique) to correct for respiratory motion artifacts. This approach is based on sorting the acquired PET data in multiple amplitude bins which is currently not possible on any commercial PET/CT scanner. The second section is focused on the hardware/software design of an in-house respiratory gating device that is necessary to facilitate the implementation of the FBAG technique. Currently there are no commercially available respiratory gating systems that can generate the necessary triggers required for the FBAG technique. The third section is focused on developing a joint correction technique that can simultaneously suppress respiratory motion artifacts as well as partial volume effects (PVE) which represent another source of image degradation in PET/CT imaging. Computer simulations, phantom studies, as well as patient studies are conducted to test the performance of these proposed techniques and their results are shown in this thesis.

Acknowledgements:

I would like to thank Dr. John W. Clark, a good advisor in Rice University, for introducing me into the field of biomedical imaging, for helping me understand what the advances of this field are going on, for recommending me to a hospital environment to conduct my M.S/Ph.D research.

Thanks to Dr. Osama Mawlawi to be a great friend and advisor at the same time, for offering me a position to conduct my research work in MD Anderson Cancer Center, for offering me great opportunities of hands-on experience in various medical imaging modalities, for helping me with difficulties whenever I felt helpless.

Thanks to my parents and families for their greatest support to my studies.

Thanks to all the lab staff in ECE@RICE and DI@MDACC, to help me with various problems I faced in the process of this Ph.D. research work.

Dedicated to my parents

whose love and help are always encouraging me

To my girlfriend

to be always with me whenever I feel difficult

Content

List of Tables

List of Figures

Introduction

In Positron Emission Tomography/Computed Tomography (PET/CT) Imaging, patients' respiratory motion usually causes motion blurring artifacts in PET images as well as mismatch between PET and CT images. Both effects can lead to image degradation which could affect patient management.

Several respiratory gating techniques have recently been proposed in PET/CT imaging to suppress motion artifacts. These techniques are divided into two categories: phase gating and amplitude gating. In phase gating, the respiratory cycle is divided into multiple phase ranges and the acquired data is sorted into each phase range based on its acquisition time within the respiratory cycle. This gating approach works well for patients with regular breathing cycles but results in strong artifacts with patients that have irregular respiration. As an alternative, amplitude gating has been proposed to divide the total respiration amplitude into different amplitude ranges (gate) rather than phase ranges. It has been shown that amplitude gating is better at suppressing respiratory motion artifacts when compared to phase gating. Current PET/CT scanners however, are only capable of phase gating. In this regard, the development of amplitude gating techniques in PET/CT imaging is currently the focus of many research groups.

The aim of this thesis is to design, implement and evaluate respiratory motion correction techniques that can overcome respiratory motion artifacts in PET/CT imaging. The thesis is composed of five chapters. The first chapter provides a description of the fundamentals of PET imaging, including data acquisition, image reconstruction, and PET/CT multi-modality imaging. This chapter also includes a discussion of: respiratory

motion artifacts and partial volume effects that degrade PET/CT image quality and affect the accuracy of PET image quantification. These two effects and their possible correction methods represent the main focus of this thesis. In the following three chapters, we propose two novel approaches to correct for respiratory motion artifacts and partial volume effects.

The second chapter introduces a novel approach to correct for respiratory motion artifacts by proposing a free-breathing amplitude gating (FBAG) technique. This technique has the ability to automatically sort the acquired PET data into multiple amplitude bins. The proposed FBAG technique can automatically match the patient's respiratory motion amplitudes captured during the CT and PET scans with minimal user interactions, patient's radiation exposure and image registration. The methodology behind the FBAG technique, its implementation and automation in current PET/CT scanners with minimum user interactions are described in this chapter. Furthermore, phantom and patients experiments to evaluate the performance of the proposed FBAG technique and their results are also presented in this chapter. The phantom study is used to evaluate the performance of this technique in a pseudo-clinical environment while the patient studies are used to test this FBAG approach in clinical environments.

The third chapter of this thesis focuses on the design of an in-house respiratory gating device (hardware and software) which is necessary to facilitate the implementation of the FBAG technique since currently there are no commercially available respiratory gating systems that can generate the necessary triggers required to implement FBAG. This in-house respiratory gating system consisted of a respiratory sensor coupled to a National Instruments data acquisition device which was controlled by an in-house

Labview® software program. A volunteer study and a phantom study were conducted in this chapter to evaluate the performance of the in-house device. The aim of the volunteer studies is to test the capability of this device to detect respiratory motion waveforms while the aim of the phantom study is to evaluate its performance to suppress respiratory motion artifacts. The results from these studies are presented at the end of this chapter

The fourth chapter of this thesis focuses on developing a technique that can improve the accuracy of PET image quantification by simultaneously suppressing respiratory motion artifacts as well as partial volume effect (PVE) which represents another source of image degradation in PET/CT imaging. In this chapter, a joint motion-PVE correction approach is presented and tested. The proposed approach incorporates a model of motion blurring, PVE and object size/shape and is able to estimate the true tumor activity concentration (AC) and motion blurring kernel (MBK) by using a deconvolution algorithm. A simulation and a phantom study were conducted to evaluate the performance of this joint correction approach. The objective of these studies is to test the performance of this joint correction approach and evaluate its capability to improve the accuracy of PET image quantification. The results from these studies are presented at the end of this chapter.

Conclusions of this thesis are summarized in the fifth chapter with a discussion of possible future work.

Chapter 1

Overview of Positron Emission Tomography

Positron emission tomography (PET) is a non-invasive imaging technique for probing the distribution of cell metabolic activity in the human body. It is clinically utilized for the diagnosis, staging and evaluation of the therapy response for patients with certain conditions that affect the brain, heart as well as certain types of cancer. This imaging technique first appeared in clinical diagnostic medicine in the early 1990s and had the unique capability to produce functional (Figure 1.1a) rather than anatomical or structural images (Figure 1.1b), such as those generated by X-ray computed tomography (CT) or magnetic resonance imaging (MRI). Functional images can reveal biochemical processes within the human body, such as blood flow, receptor density and glucose metabolism. A PET scan is a relatively simple procedure, involving the use of a small amount of radioactive material, similar to those that are used in other nuclear medicine procedures such as Planar Imaging and Single-Photon Emission Computed Tomography (SPECT). In PET imaging, the radioactivity is attached or tagged to a radioactive material that is intrinsic to the human body (e.g. glucose, water, and ammonia). The radioactive material is administered to the patient through injection or inhalation and a specially designed PET scanner monitors how the body processes this material. For instance, ^{18}F labeled fluro-deoxy-glucose (^{18}FDG) is a "glucose analog" that accumulates in regions having high metabolic activity such as brain, liver and malignant tumors (Figure 1.1a). Consequently, accumulation (uptake) of ^{18}F-FDG by the tissue is directly related to its metabolic state (hyper or hypo-metabolic), and an abnormal increase in

uptake would indicate the presence of malignant tumor cells. Thus, PET has the ability to non-invasively detect functional changes in vivo with high sensitivity and specificity [1]. An important additional advantage of PET imaging is its ability to quantify the amount of radioactivity taken up. This aspect is particularly important in the diagnosis, staging, and evaluation of treatment response. These advantages have enabled wide acceptance of PET imaging as a diagnostic and a research tool, with applications in oncology [2, 3], neurology [4], cardiology [5], and pharmacology [6].

This chapter starts with a brief introduction to the fundamentals of PET imaging, including the processes of PET data acquisition and image reconstruction. The closely related topic of PET/CT multi-modality imaging technique is also discussed, followed by the description of respiratory motion artifacts and partial volume effects in PET/CT

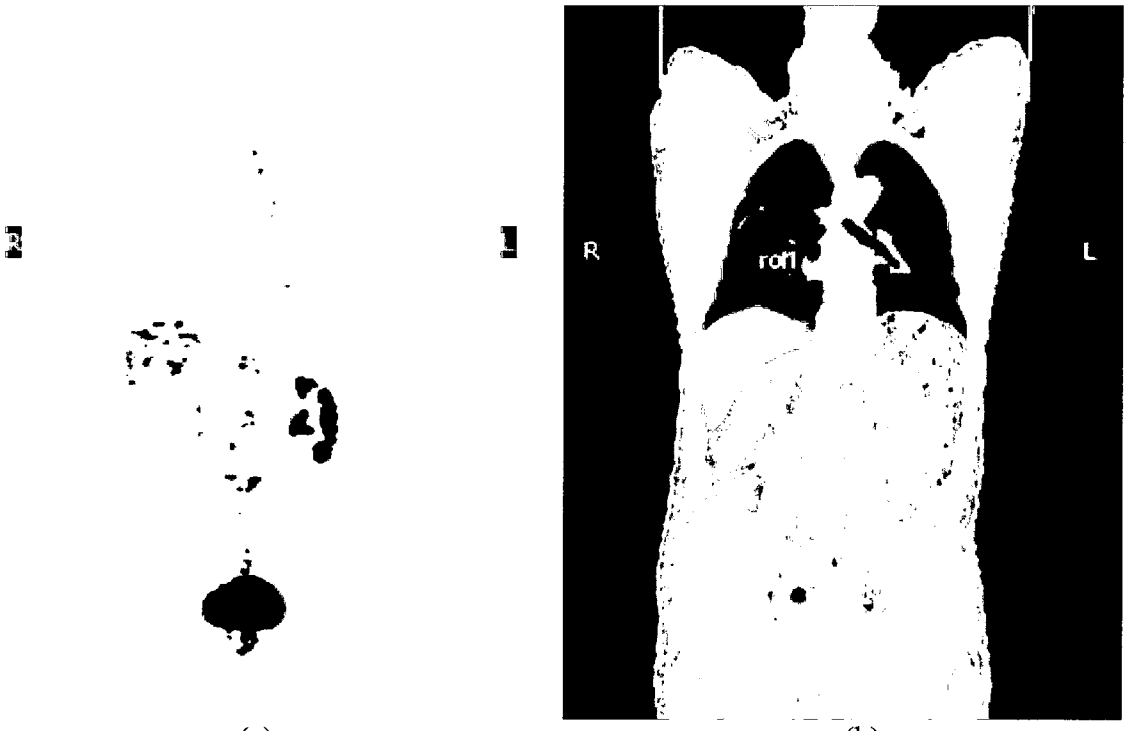

(a) (b)

Figure 1.1: Example of (a) PET image and (b) CT image

imaging as well as approaches that have been implemented to correct for these effects. This chapter ends with an introduction to the proposed respiratory motion correction techniques which will be the primary focus of this dissertation.

1.1 PET data acquisition

A PET scan requires the patient to either inhale or be injected with radioactive materials that are labeled with positron emitting radio-nuclides. The most commonly used positron-emitting nuclides are ^{18}F, ^{15}O, ^{13}N and ^{11}C, which constitute the most abundant elements in human's body. These positron-emitting nuclides can be used to label many compounds to make radio-pharmaceuticals such as ^{11}CO, $^{13}NH3$, ^{15}O-labeled water and

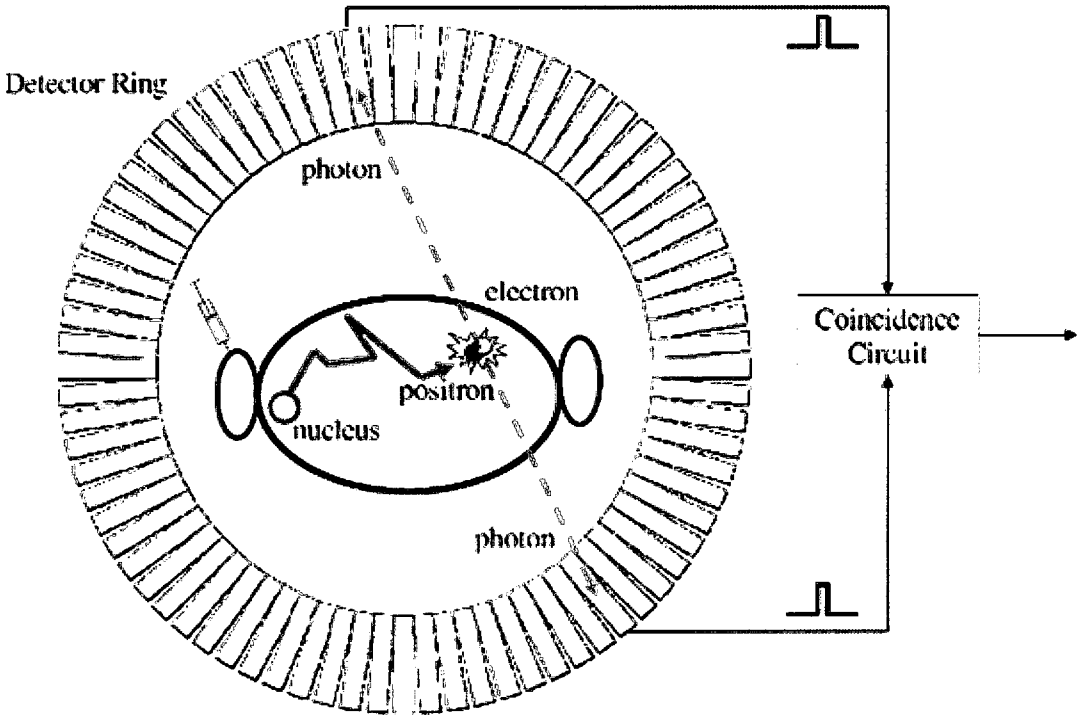

Figure 1.2: Process of PET imaging

^{18}F-FDG. These various radioactive labels decay by emitting positrons, which are the anti-particles of electrons. When positrons and electrons collide, they annihilate with one another, resulting in the production of two gamma photons. From the theorem of energy conservation, each gamma photon has an energy of 511 keV, and the two gamma photons emitted travel in opposite directions due to the conservation of momentum.

The process of PET imaging is illustrated in Figure 1.2. When positron-electron annihilation occurs, the two gamma photons are emitted simultaneously in opposite directions, hitting two detectors within a time frame of several nanoseconds. Consequently, two detections made within such a small timing window are assumed to constitute a "coincidence event" resulting from positron-electron annihilation. A line connecting the two detectors is recorded (a "line-of-response (LOR)"), which indicates that the annihilation occurred somewhere along this line. As the scanning process

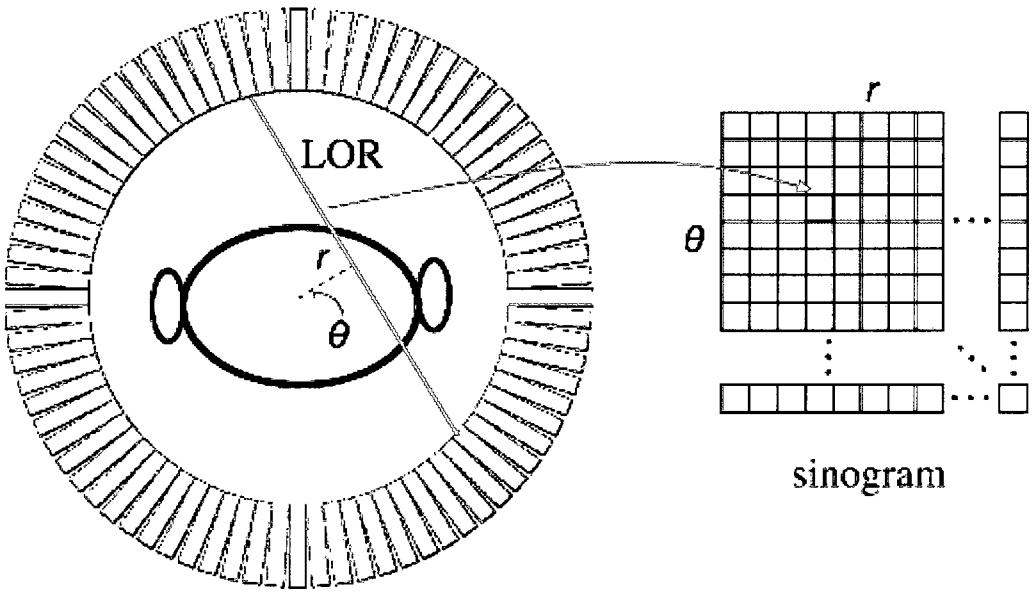

Figure 1.3: Mapping relationship between LOR and sinogram data in 2-D mode

continues, additional coincidence events occur along each possible LOR. Data collection along each LOR is either sorted into a histogram (usually called a Sinogram) according to their locations (e.g., radial distance and view angle in 2-D mode as shown in figure 1.3), or stored on an event-by-event basis known as a List-Mode acquisition. As a rough approximation, the total number of coincidence detections along a specific LOR can be considered proportional to the line integration over the underlying radioactivity distribution. Using such a model, the sinogram constitutes a Radon transform of the original radioactivity distribution [7], which is formulated as:

$$\hat{g}(\rho,\theta) = \int_{-\infty}^{+\infty}\int_{-\infty}^{+\infty} g(x,y)\delta(\rho - x\cos\theta - y\sin\theta)dxdy \qquad (1.1)$$

Here, the Randon transform $\hat{g}(\rho,\theta)$ is the line integration of the image $g(x,y)$, which is specified by the line parameters (ρ, θ), where ρ is the distance from the center of the field of view (FOV) to the specific line and θ is the pitch angle of the line.

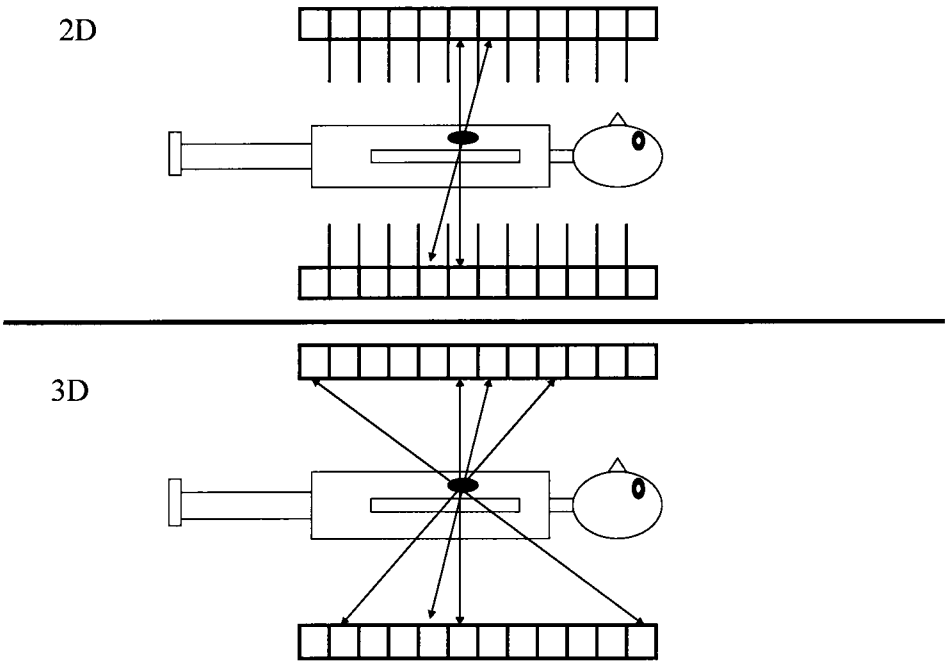

Figure 1.4: 2-D vs. 3-D mode in PET imaging

PET data can be acquired in either 2-D or 3-D mode (Figure 1.4). In 2-D mode, data are collected slice by slice, which is implemented using extendable septal barriers imposed between adjacent slices. These barriers are strips that can be extended from the scanner body to help stop gamma photons coming from other slices. An accepted LOR is therefore limited in the trans-axial plane, axially spanning no more than two adjacent detector rings. In the 3-D whole body mode, data is collected with these same septa retracted enabling a 3-D acquisition. Here, LORs are not constrained in the trans-axial planes and may span across many detector rings. 3-D acquisition affords better detection since it can accept more coincidences. However, the image reconstructed from 3-D acquisition is also corrupted by a greater amount scatter, which will be discussed later in this chapter.

1.2 PET Image Reconstruction

PET image reconstruction represents the inverse problem associated with PET data acquisition (i.e., formation of an estimate of the original object via analysis of the acquired image data). In PET imaging, the acquired PET data (sinogram/histogram or list-mode data sequence which is eventually rebinned as a sinogram) is first reconstructed to images prior to evaluation by a physician and quantitative mathematical analysis. Typically, a filtered back-projection (FBP) algorithm having widespread use in image reconstruction (e.g., [8]) is used to form an image of the distribution of the radio-activities within the body from collected sinogram data. This FBP technique is performed under the assumption that sinogram data can be modeled as a Radon transform of the true

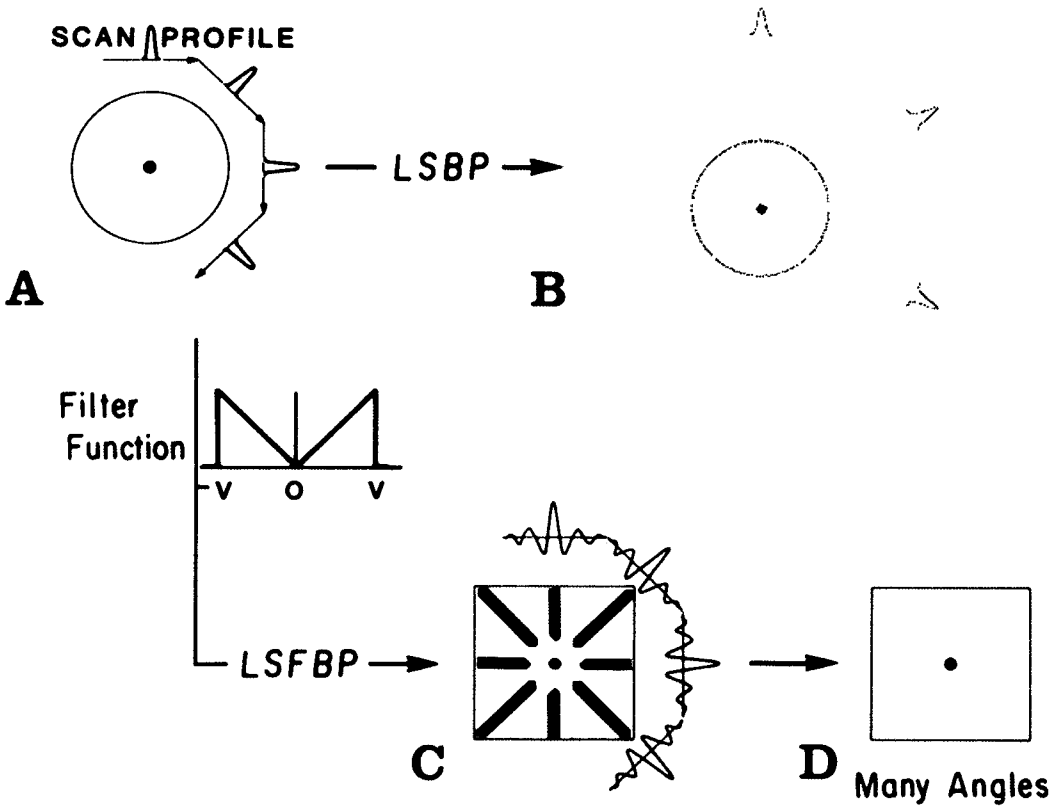

Figure 1.5: Filtered Back-projection (FBP) reconstruction for PET imaging

object being imaged (see previous section). Data collected from each angle are first filtered with a chosen filter and then back-projected to image space (Figure 1.5). As more and more angles are projected, the original object appears. This FBP model, however, is algorithmic and does not adequately describe the various physical processes involved in the photon detection process. It also lacks the ability to account for detection noise.

Statistical image reconstruction techniques provide more accurate system models and have been shown to generate images of better quality [9-11]. In this case, the PET imaging system is usually modeled as a discrete-discrete system [12] described by the expectation:

$$E\{y_n\} = \sum_{n=1}^{N} H_{nm} x_m + r_n \qquad (1.2)$$

Here $\{y_n\}$ is the sinogram data vector. The vector $\{x_m\}$ is the image representation which contains the amount of radioactivity inside each pixel or voxel (3-D pixel), and the term r_n in (1.2) accounts for background noisy counts, including random and scattered coincidences. Due to the statistical nature of PET imaging, r_n is usually modeled as a Poisson noise distribution. Alternatively, random and scattered events can be incorporated into (1.2) via the term r_n because of their statistical nature. Finally, matrix H is called the system matrix, whose elements H_{nm} are proportional to the probability that a photon pair originated from the voxel m can be detected along the LOR n. This design for the system matrix allows one to incorporate significant modeling detail including physical processes such as positron range, non-collinearity, attenuation correction, detector efficiency normalization and depth of interaction. Integrating such modeling detail into the system matrix description produces a product that can better reflect the true photon detection probability [13-14].

Statistical image reconstruction is generally formulated as an optimization problem in which a cost function is introduced that relates the image estimate to the measured data. A popular choice for this formulation is based on the maximum likelihood (ML) method, where an optimal image is the one that maximizes the probability of making a detection of the data that are actually measured:

$$X' = \arg\max_{X} P(Y \mid X) \qquad (1.3)$$

Here Y and X are the sinogram and image vector, respectively, and $P(.)$ is the Poisson likelihood function. It is well-known however, that ML-based image reconstruction is an

ill-conditioned problem, in that small changes in the data can cause large variations in the reconstructed image [15]. When reconstructing a specific data set, it can be observed that as the ML algorithm progresses to high iteration numbers, the image becomes increasingly noisier. Consequently in practice, optimization of the ML cost function is usually terminated before convergence is reached. In addition, smoothing filters are usually applied to the image during or after the optimization process to suppress image noise.

Iterative techniques are usually employed to solve the image reconstruction problem. For ML reconstruction, the most popular iterative technique is the expectation maximization (EM) algorithm [16], which has the advantage of employing a closed form updating equation:

$$x_m^{(p+1)} = \frac{x_m^{(p)}}{\sum_i H_{ij}} \sum_i H_{ij} \frac{y_i}{\sum_j H_{ij} x_j^{(p)} + r_i} \tag{1.4}$$

Here, $x^{(p)}{}_m$ is the value image voxel m after p iterations. A major drawback of the ML-EM algorithm, however, is its slow convergence. To accelerate the optimization process, variants of the EM algorithm based on the concept of subsets have been developed [17-19], wherein a given EM iteration is divided into a number of sub-iterations, and each sub-iteration only deals with a subset of the whole acquired data (sinogram). The image resulting from one sub-iteration is then updated by the next sub-iteration. This variant of the EM algorithm is called the Ordered-Subset Expectation Maximization (OSEM) [17] which works much faster than ML-EM while achieving similar convergence.

After the image reconstruction process, the PET images are displayed so that physicians can evaluate and diagnose patients' tumors based on ^{18}F-FDG activity

concentration (AC, unit: Bq/ml or disintegration/second/ml). The AC can be normalized by the patient's weight (unit: gram) and injected dose (unit: Bq) to generate a standardized uptake value (SUV):

$$SUV(g/ml) = \frac{AC(Bq/ml)}{injected\ dose(Bq)/weight(g)} \tag{1.5}$$

The SUV can be used to indicate the malignancy of the patient's tumor: as this value becomes higher and higher, there is larger and larger probability that the tumor is malignant. In clinical diagnostic PET imaging, a threshold of 2.5 is usually employed to distinct a malignant lesion from being benign. The whole process of PET imaging, including data acquisition, data storage and image reconstruction and display, is summarized in Figure 1.6.

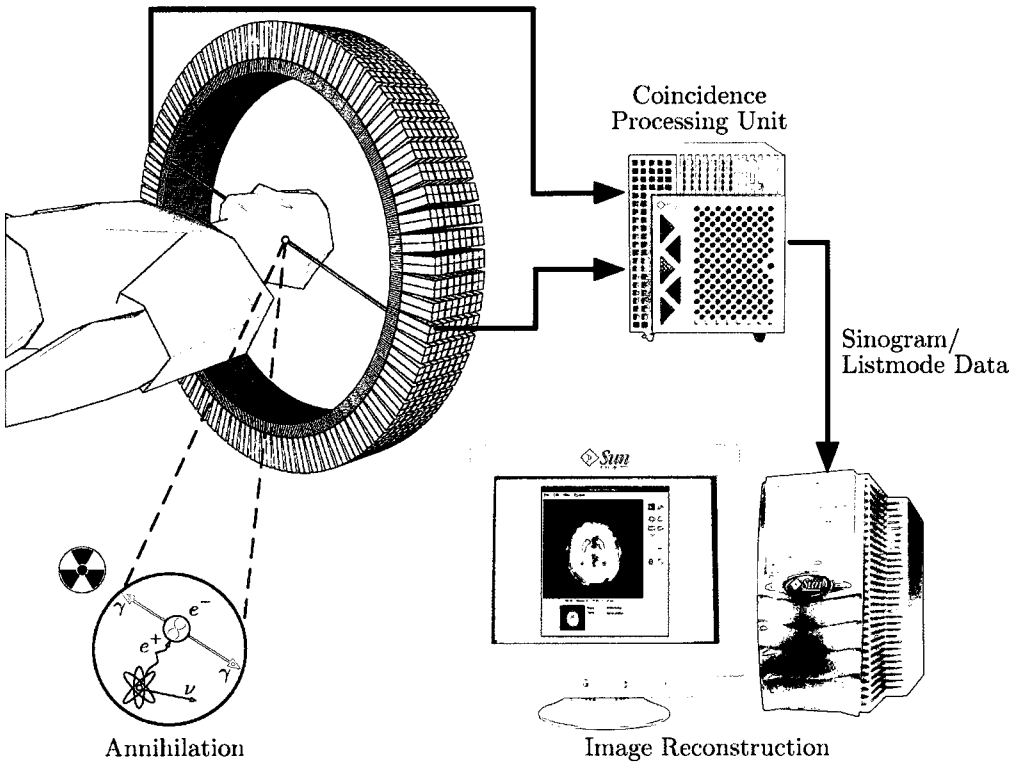

Figure 1.6: The process of PET imaging

1.3 PET/CT multi-modality imaging

PET imaging has great advantages as a functional imaging technique since it measures the bio-radio tracer uptake distribution which is an indicator of patient's body function such as blood flow, glucose metabolism and receptor density. However, PET also has its limitations especially when dealing with anatomy-related tasks such as lesion localization and tumor volume measurement. This is due to its low image resolution and relatively high image noise level when compared to other anatomical imaging modalities such as CT and MRI. Consequently, functional images provided by PET and anatomical images provided by CT or MRI are usually combined/fused together to facilitate the diagnosis, staging and therapy response of various kinds of lesions.

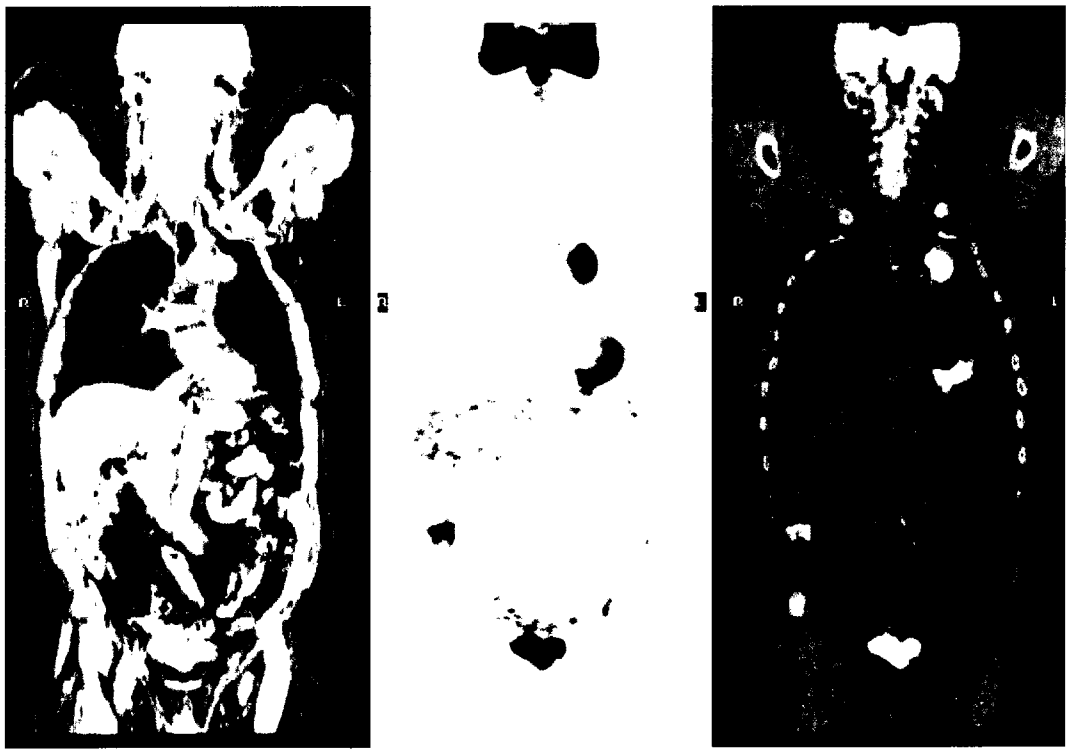

(a) (b) (c)

Figure 1.7: Images generated in a PET/CT for the same patient.
(a) CT, (b) PET, (c) Fused PET/CT.

Figure 1.7 shows an example of the PET/CT multi-modality imaging, where the PET, CT and fused PET/CT images are displayed side by side to provide both functional and anatomical information. An implicit assumption in this practice is that the PET image is properly aligned with the CT image, so that a lesion identified on the PET image can be readily localized on the CT image. If the patient needs to be transported between different scanners (PET & CT), a change in the external pose, as well as internal organ displacement could occur between the two imaging sessions. Consequently, an extra image registration step is often required to register the images acquired from different imaging sessions with one another [20]. This increases the complexity of the imaging process and reduces the reliability of the overall approach. In order to solve this problem, PET/CT combined imaging has been introduced as an alternative to the dedicated PET scanner. In current PET/CT scanners, the PET component is integrated with a modern multi-slice CT scanner while a CT scan followed by a PET scan are acquired for the same patient within the same imaging session (Figure 1.8) This imaging technique minimizes the patient motion between the PET and CT scans and facilitates better co-registration between the acquired PET and CT images. In addition, the well-registered CT image can also be used to correct for the PET data attenuation because some of the gamma photons generated during the PET scan is absorbed by the patient body tissues [23].

Nowadays, dedicated PET scanners are rarely made by major medical imaging equipment manufacturers but rather combined PET/CT scanners are usually supplied. The success of combined PET/CT scanners has motivated the exploration of other multi-modality imaging techniques, such as the single photon emission computed tomography (SPECT)/CT imaging and PET/MRI imaging.

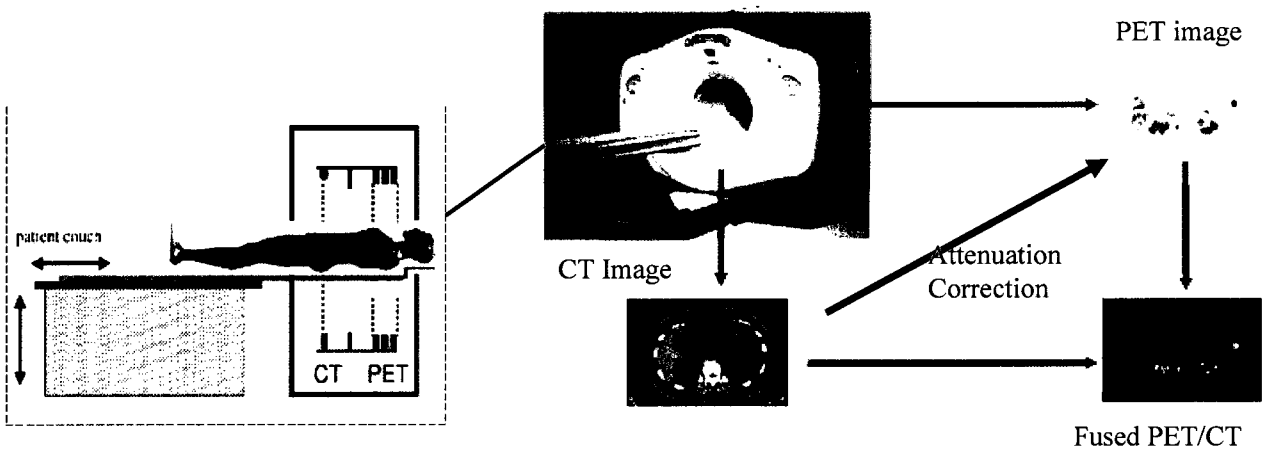

Figure 1.8: A schematic illustration of the PET/CT scanner.

1.4 Primary Focus: Respiratory motion artifacts

In this section, we will introduce the respiratory motion artifacts that are existent in PET/CT images which will be the primary focus of this thesis. Approaches that have been proposed to compensate for the respiratory motion artifacts on either the CT or the PET components of PET/CT imaging are also described and discussed.

1.4.1 Introduction to respiratory motion artifacts

A popular research topic in PET/CT imaging that has recently been attracting people's attention is the motion of the object to be imaged. Due to the low count rate of the data acquisition, long scan durations for PET imaging are required to accumulate a sufficient amount of photon counts in order to achieve reasonable PET image quality (resolution, contrast, noise, signal-to-noise ratio etc). In clinical settings, the scan duration for PET session is typically 3–5 minutes per bed position (around 15 cm axial extent) with a combination of usually 5-8 bed position for a whole-body scan. This is

primarily due to the tradeoffs between photon statistics and patient comfort, i.e. the longer the scan duration is, the more photon counts will be accumulated, but at the same time the more uncomfortable the patient will feel. During the long scan duration of PET session (>20 minutes for a whole-body scan), patient motion is unavoidable which includes accidental voluntary motion such as head movements and involuntary motion such as respiratory and cardiac motion. As a result, the acquired PET data reflects a motion-averaged object and the reconstructed image shows motion blurring artifacts that reduce image resolution and contrast and cause inaccurate image quantification such as the tumor SUV underestimation. Figure 1.9 shows a phantom study that illustrates this effect. In this study, a positron emitting line source is scanned on top of a motor-driven moving platform that can move vertically. The sinogram acquired for the stationary line source show a single sinusoidal curve, which is broadened when the source moves. Figure 1.10 shows another study where a phantom containing six spheres filled with ^{18}F-FDG water is placed on a moving platform that moves in the axial direction of the PET scanner while PET data are being acquired. The spheres on the reconstructed images show elongated shape and decreased contrast due to the existence of the motion.

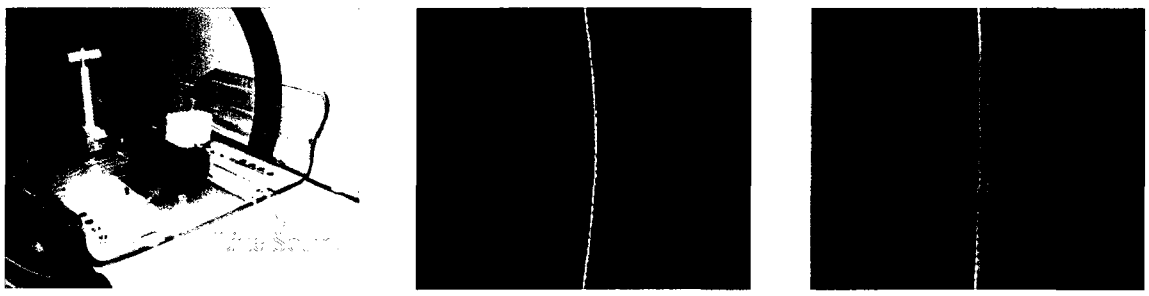

(a) (b) (c)

Figure 1.9: A phantom study showing the effect of motion in acquired PET data. (a) The phantom setup. (b) Sinogram acquired when the line source is stationary. (c) Sinogram acquired when the line source moves. The vertical and horizontal axes in (b) and (c) correspond to projection angle and radial distance respectively.

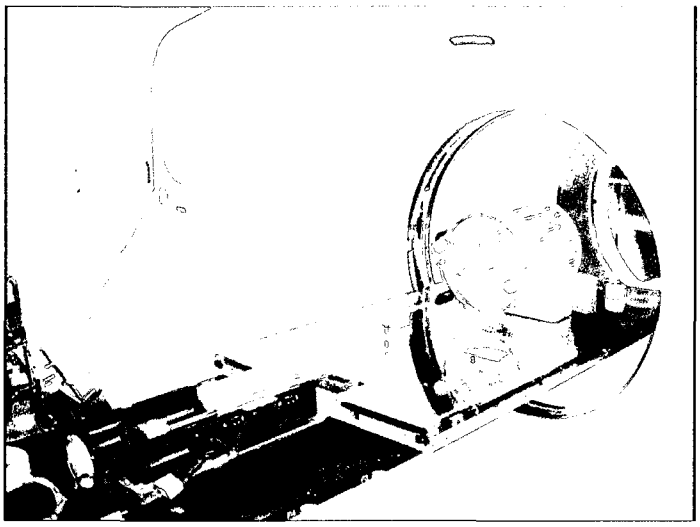

(a)

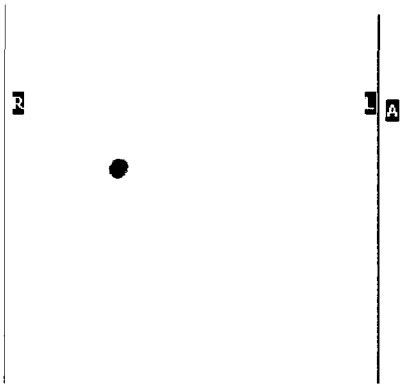

(b)

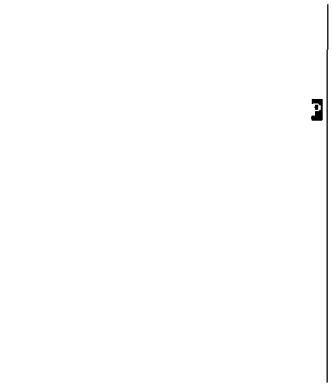

(c)

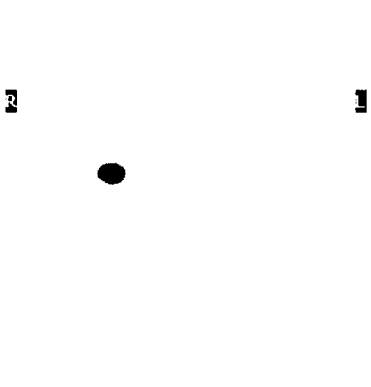

(d)

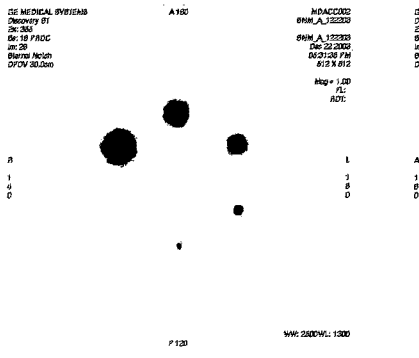

(e)

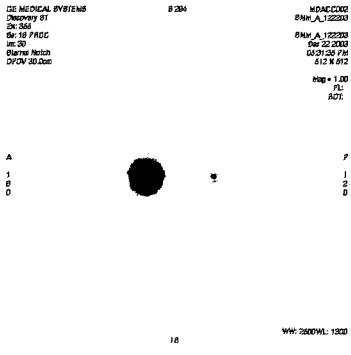

(f)

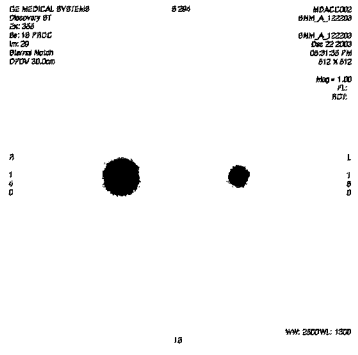

(g)

Figure 1.10: A phantom study showing the effect of motion on the reconstructed PET image. (a) The set-up of the phantom study. The axial, coronal and sagital field-of-view for both the motion-blurred and motion-free PET images are shown in (b)-(d) and (e)-(g), respectively.

Besides the motion blurring effect in PET session itself, PET/CT imaging has an additional motion-induced artifact. Unlike PET, CT acquisition usually has a short scan duration since the CT scan is a "high-count" scan. A whole-body CT scan only takes 1-10 seconds using modern multi-slice CT scanners while the scanning of the chest region is usually performed when the patient is holding his/her breath. In this regard, minimal motion is expected and the CT image can be regarded as a snapshot of the patient which is a "motion-free" image. As a result, there usually exists a mis-match between the respiratory motion amplitudes that are captured during the motion-averaged PET image and the CT snapshot. When the CT is used for attenuation correction of PET data, the mis-match between PET and CT can then cause image artifacts on the corrected PET image. An example of such artifacts is the "banana artifact" in PET/CT imaging of the chest region, whereby a shift of the diaphragm on CT image relative to its average position on PET image can cause a banana-shaped region with either over- or under-estimation of the activity concentration on the attenuation- corrected PET image, depending on whether the diaphragm is shifted upward or downward (Figure 1.11).

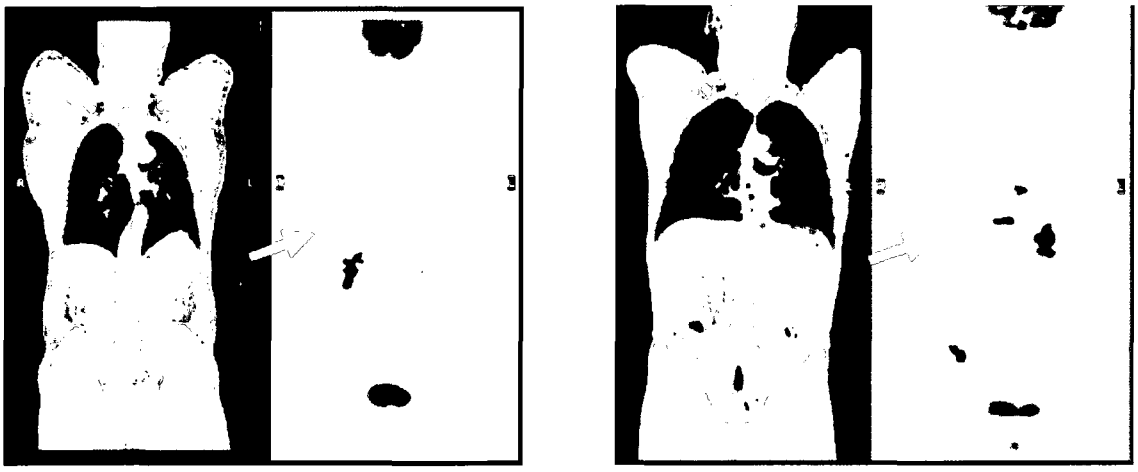

Figure 1.11: Banana artifacts due to the discrepancy between PET and CT.

1.4.2 Motion correction techniques in CT

Approaches to correct for motion artifacts in PET/CT imaging, including both the motion blurring effects in PET images and mis-match between the PET and CT data, have been investigated on both CT and PET imaging modalities. As the CT induced motion artifacts are mainly due to the difference in durations of data acquisition between PET and CT scans, some researchers have suggested the use of a slow rotating gantry in the CT scan of the chest in order to produce a CT image with similar motion blurring effect as in the PET image [24]. The motion averaged CT can then be better aligned with the PET to avoid possible artifacts during the attenuation correction process. A problem with this approach is that the slow rotation of the CT gantry can cause inconsistency in the collected data as the object moves, thus producing new artifacts in the reconstructed CT image. Furthermore, the averaged CT image acquired using this method cannot be used for diagnostic purposes. A better approach is developed in [25] using 4D CT acquisition of the chest. In 4D CT acquisition, CT data are continuously acquired at a fixed bed position using a fast rotating gantry for a duration that lasts at least one motion cycle. The acquired data are then resorted to different time intervals spanning the acquisition period. CT images can then be reconstructed for each time interval, forming a sequence of snapshots of the moving object. This process is illustrated in Figure 1.12. Finally, a motion averaged CT image can then be generated by averaging the 4D CT image sequence and is then used for attenuation correction of the PET data. Since each image of the 4D CT sequence is acquired using a fast rotating gantry, minimal data inconsistency is expected and the resulting snapshots provide motion information about the object which can be used for diagnostic and treatment planning purposes. However,

both CT based motion artifacts correction techniques cannot remove motion blur in the PET image. Rather, they are targeted at the specific motion artifacts induced by CT based attenuation correction, by compromising the CT image quality to suit that of the PET image. Furthermore, the use of 4-D CT scan increases the patient X-ray radiation exposure since it captures multiple snapshots of single CT scan. The increased exposure associated with the 4D CT acquisition compromises its clinical applications in diagnostic PET/CT imaging. Consequently, in order to remove the motion blur effects, corrections have to be made to the PET data themselves.

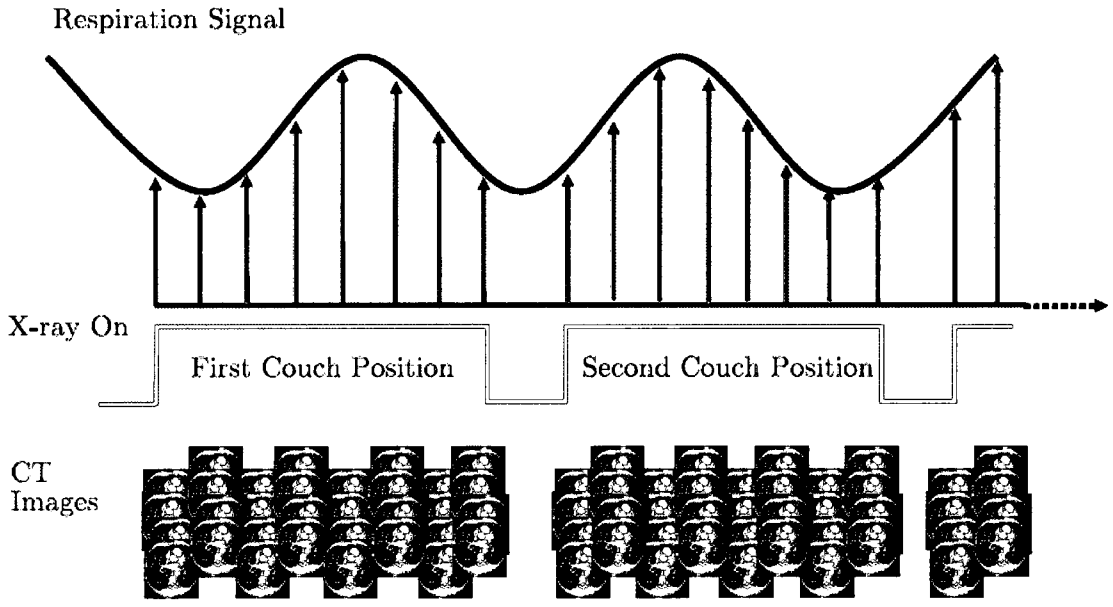

Figure 1.12: Process of 4-D CT data acquisition.

1.4.3 Motion correction techniques in PET

1.4.3.1 Rigid motion

Methods to compensate for motion artifacts in PET imaging is generally divide into two categories: rigid motion correction and non-rigid motion correction. For rigid

motion, Picard and Thompson have proposed a multiple-acquisition-frame (MAF) method [26], whereby motion is monitored by an external device and a separate image frame is acquired whenever the motion of the object exceeds a certain threshold. All image frames are then reconstructed individually and are transformed to a common location to get an averaged image. The main drawback of this method is that it will produce many low-count frames in case of frequent motion, resulting in a large number of noisy images. Another popular approach is to correct the PET data on an event-by-event basis (list-mode) [27]. These types of approach also monitor motion using an external device. However, they differ from the MAF method in the treatment of the acquired data. In these types of approach, each recorded LOR is transformed back to the location it would have been detected had the object remained stationary, according to the measured motion. The motion corrected data can then be used by any image reconstruction algorithms to get the motion corrected image. These types of approach have the advantage that the image is reconstructed using data acquired during the entire scanning period, without generating noisy intermediate images as in the MAF method. In addition, LOR correction can be implemented efficiently using hardware, so that the acquired data can be corrected on-the-fly. The disadvantage of this method is that the transformed LOR may fall on gaps between detectors or go outside the scanner field of view and thus cannot be mapped to a corrected LOR. In such cases, data are either discarded or approximations have to be made. However, these methods can generate a large amount of errors when they are used for non-rigid motion for the following reasons: firstly, it is difficult to measure the internal non-rigid motion using an external

monitoring device; secondly, with non-rigid motion a one-to-one mapping between the measured LOR and the corrected LOR as in event-based approaches does not exist.

1.4.3.2 Respiratory motion: 4-D PET/CT acquisition

The two most important non-rigid motions in PET imaging are the respiratory and cardiac motion, with respiratory motion being more significant in terms of the amplitude of the motion.

In order to compensate for respiratory motion artifact, 4-D PET data acquisition which is similar to 4-D CT acquisition has been traditionally introduced. In a 4-D PET acquisition, an external device is used to send a gating signal or trigger to the scanner each time a certain phase or amplitude of the motion cycle is reached. The scanner then divides the patient's respiratory motion cycle into a sequence of phase or amplitude ranges (bins or gates), and groups the data accordingly into these gates. Images of different phase or amplitude ranges can then be reconstructed from their corresponding data sets. In other words, a 4-D PET scan forms a sequence of snapshots of the moving object, each snapshot can be considered as a motion-free image provided that there is enough number of time bins or amplitude gates. Since each snapshot only constitutes a smaller amount of acquisition time with respect to the whole cycle, each frame of the 4-D PET images is characterized by low signal-to-noise ratio (SNR). In order to improve the image SNR, deformable registration methods are often employed to register and sum together the multiple frames of these image sequences to generate a high-SNR motion-free PET image [28]. This process is illustrated in Figure 1.13 which uses a phase gating and amplitude gating scheme respectively.

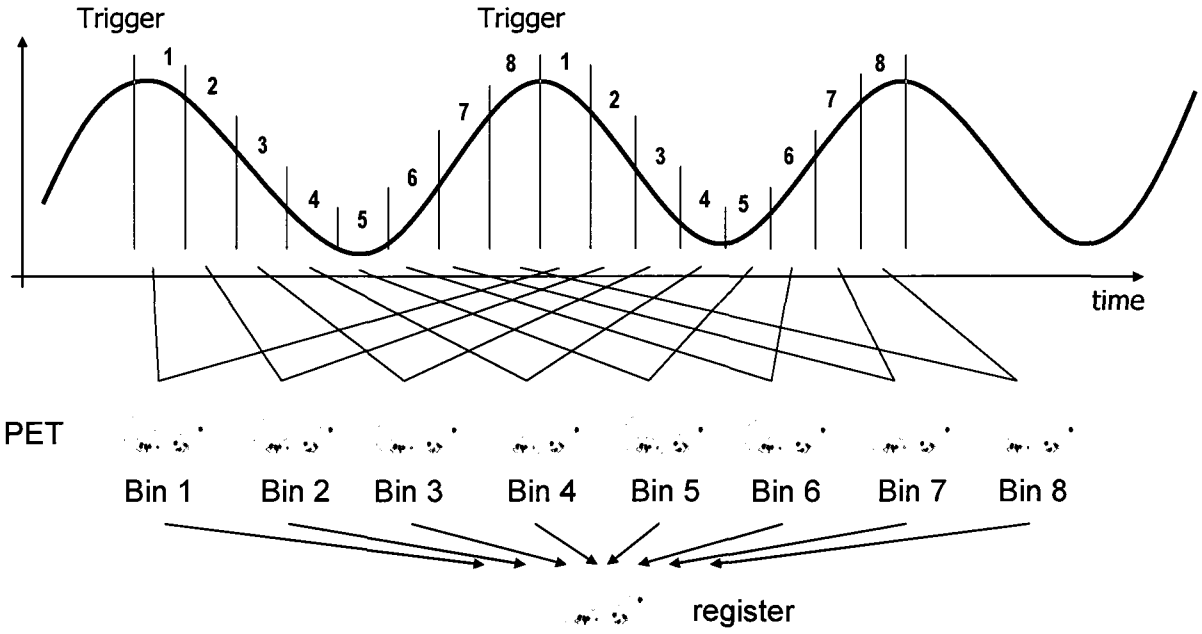

(a)

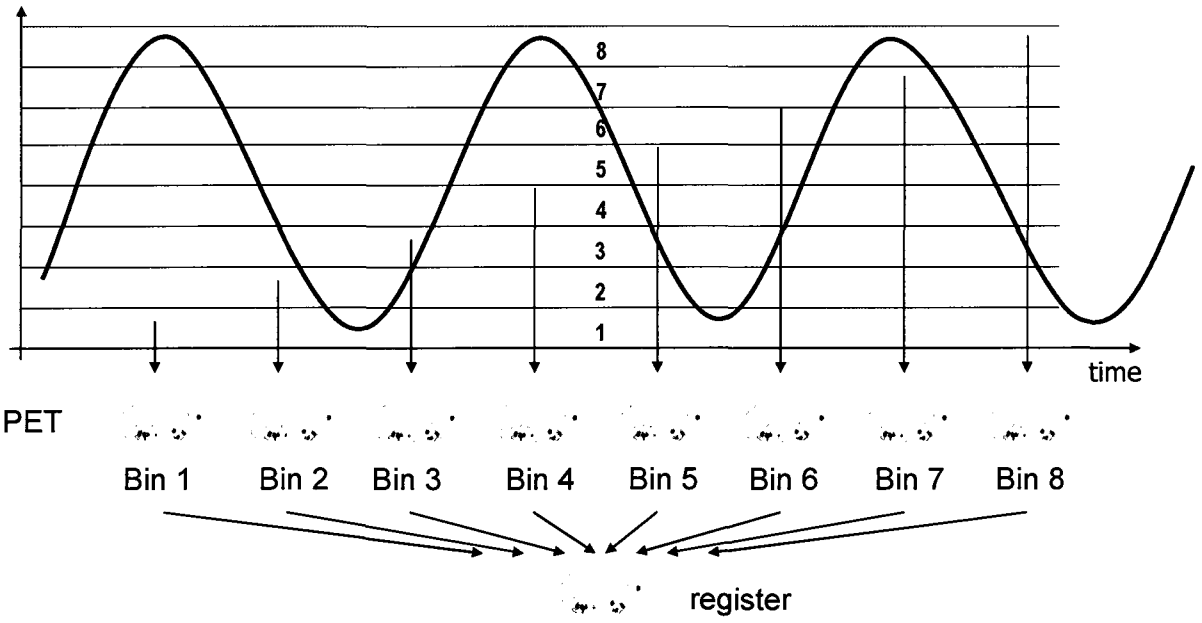

(b)

Figure 1.13: Process of 4-D PET data acquisition using (a) phase gating and (b) amplitude gating scheme respectively.

The 4-D PET data acquisition, also referred to as "PET gating approach", is divided into two categories: phase gating (Figure 1.13(a)) and amplitude gating (Figure 1.13(b)), based on whether the respiratory cycle is divide into multiple time ranges or amplitude ranges. Both of these two gating approaches can work well when the patients have regular respiratory cycles as shown in Figure 1.13. However, when the patient's respiratory cycles become irregular (e.g. varying amplitude or frequence), phase gating method will result in a large amount of error in each time bin since the acquired data within the same phase range but in different amplitudes are combined together to generate each data gate (Figure 1.14). This result has been verified by M. Dawood [29] who showed that amplitude gating approaches are advantageous to phase gating in correcting for respiratory motion artifacts and improving PET image quantification. However, despite its advantages, amplitude gating method is unavailable while phase gating is the only option on current PET/CT scanners

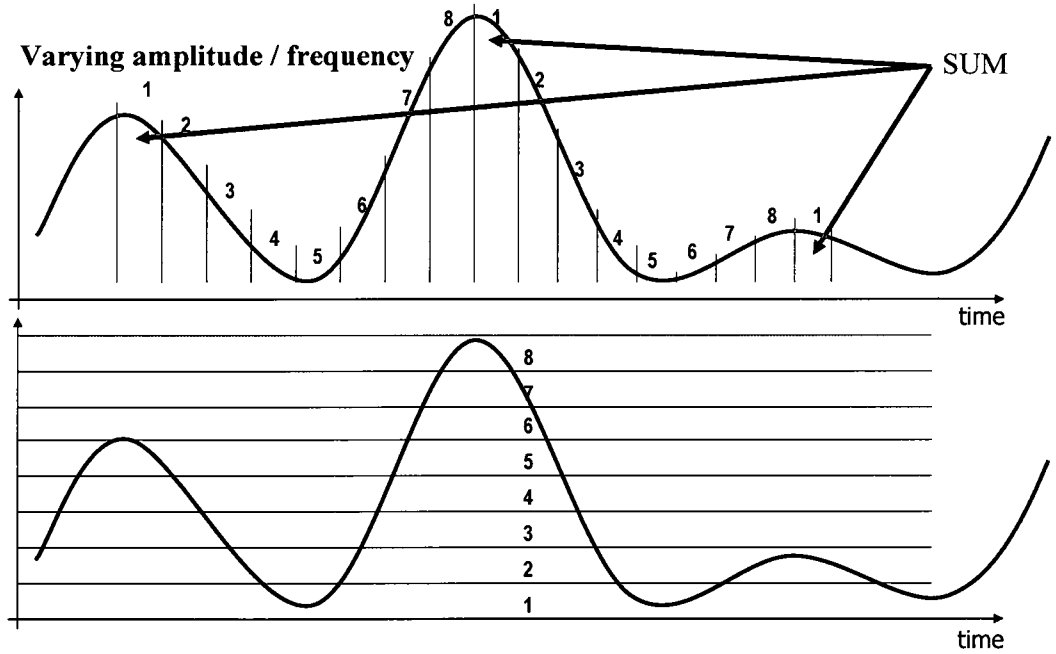

Figure 1.14: Phase gating vs. amplitude gating

In either phase or amplitude gating based 4-D PET acquisition, deformable registration methods are employment to register the 4-D PET image sequences to improve the image SNR. Another approach that has recently been utilized to improve the SNR of 4-D PET image sequence is to incorporate motion information as part of the image reconstruction process [30-36]. These approaches, from here onward, are referred to as "motion-incorporated reconstruction" methods and can be further divided into two categories. Firstly, image reconstructions in [30, 32, 33, 35, 36] are performed in a 4D maximum a posteriori (MAP) or penalized maximum likelihood (PML) framework, whereby the sequence of the 4-D PET image sequences are treated as a single image, and a smoothing prior incorporating motion information is applied on the temporal dimension in a similar way a spatial image prior is applied. Image consistency across the 4-D PET image sequence can then be enforced through this temporal image prior. As a result, each image in the 4-D PET image sequence is reconstructed with contributions from data collected within other time bins as well, thus improving photon statistics and reducing image noise level. Secondly, the approaches employed by Qi et al [31] and Jacobson et al [34], on the other hand, incorporated the motion information into the system matrix without the need of prior parameters.

Although 4-D PET data acquisition has encouraged the proposition of various approaches to correct for respiratory motion artifacts in PET/CT imaging, these methods however all require a corresponding 4-D CT data acquisition which is used to perform attenuation correction for the acquired 4-D PET image sequence. One disadvantage of the 4-D CT data acquisition is that it increases the patient's X-ray radiation exposure, which may eventually result in secondary cancer in the patient's body. Another disadvantage of

the 4-D PET/CT acquisition is that since the patient's respiratory motion is a non-rigid motion, a deformable registration method needs to be applied to either the 4-D PET image sequences in order to improve the image SNR or 4-D CT images (motion-incorporated reconstruction method) in order to derive the motion information among the different bins/gates. The deformable image registration methods, however, suffer from the problem of non-convergence and inaccuracy primarily due to the high noise content of each bin/gate of the 4-D PET data sequence and the mismatch between the corresponding bin/gate of the 4-D CT and 4-D PET data which is caused by the inconsistence of the patient's respiratory motion during the CT scan and the PET scan. Due to these limitations, 4-D PET/CT data acquisition is usually not recommended for diagnostic imaging purposes. Currently, there is a tendency in the field of PET/CT respiratory motion compensation that one single phase or amplitude range is preferred (single-gate scan) when compared to multiple phase/amplitude ranges (4-D image sequence) data acquisition. Using such "single-gate" gating scheme, the problems which are caused by the 4-D PET/CT data acquisition such as the increase in patient's X-ray radiation exposure and the requirement of deformable image registration methods can be automatically resolved since no 4-D CT scan is required in the single-gate PET/CT scan. However, in order to accumulate a sufficient amount of photon counts in the selected gate or phase/amplitude range, longer scan duration is usually required in the PET data acquisition as a tradeoff to the decreased patient radiation exposure and deformable registration. One such method that is employed to compensate for respiratory motion artifacts in PET/CT imaging is called "deep-inspiration breath hold" or "DIBH" technique.

1.4.3.3 Respiratory motion: deep-inspiration breath hold

Recently, the deep-inspiration breath-hold (DIBH) technique has been proposed as a variant of the gating approach without the need to register the 4-D PET images or increase the patient X-ray radiation exposure [37-39]. This technique works as a single-gate amplitude gating approach rather than a phase gating approach due to the proposed advantages of amplitude versus phase gating [29]. In this DIBH technique, patients are requested to hold their breath at deep inspiration for a relatively short period while both the CT and PET data can be acquired within this amplitude range. PET data acquisition in this respiratory state is then repeated multiple times in order to accumulate a sufficient amount of counts per pixel [37, 38]. The resultant multiple PET data sets are then summed together to generate a motion-free sinogram which is then attenuation-corrected by the corresponding CT image and eventually reconstructed into a motion-free image. The whole workflow of the DIBH technique is shown in Figure 1.15.

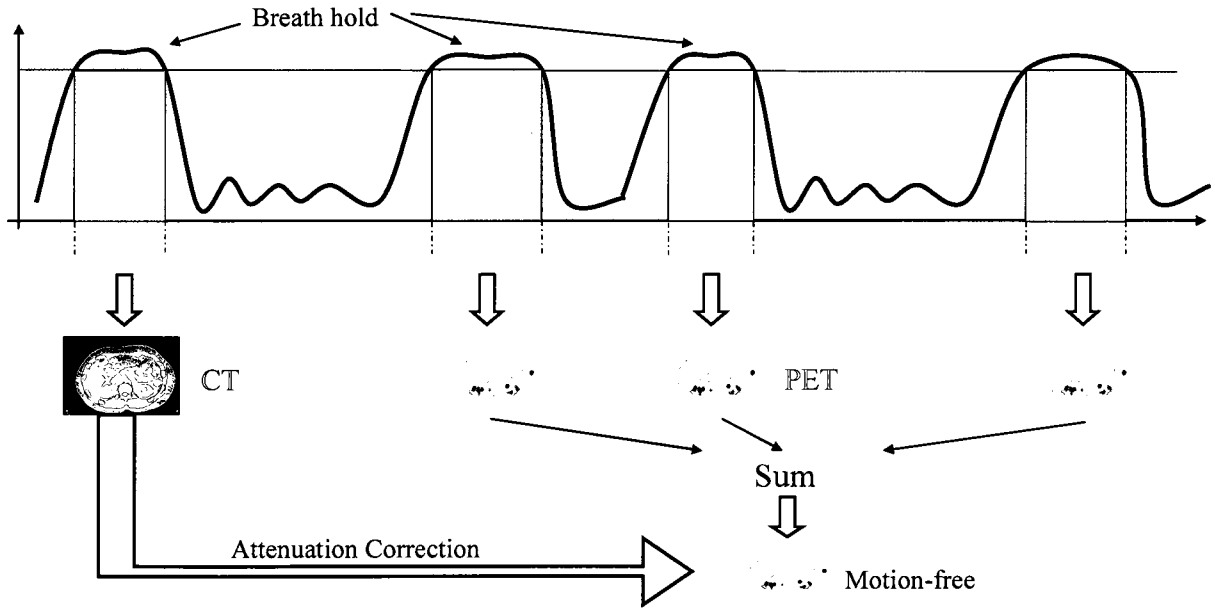

Figure 1.15: Deep-inspiration breath hold (DIBH) technique

The net result from the DIBH technique is a PET image that is matched in respiratory amplitude with a corresponding DIBH CT image since both the CT and PET data are acquired within the breath-hold periods which ensured the automatic match between the motion amplitudes "captured" or "freezed" in CT and PET. DIBH has been demonstrated to be feasible on current PET/CT scanners [37-39]. However, a main disadvantage of this technique is ensuring patient compliance to hold their breath for the specified time and amplitude in each respiratory session particularly when the patients are at an increased state of anxiety due to their medical condition. Another disadvantage of DIBH is its extensive reliance on technologist-patient interaction to coordinate data acquisition during the multiple repetitive times to accumulate the necessary data particularly with patients that have hearing or language barriers. A third disadvantage is that when the patient is holding his/her breath at deep inspiration, the lung is completely inflated with air which can eventually result in a PET/CT image that captures the inaccurate shape and size of the lung. Furthermore, recent studies from a task group in American Association of Physicists in Medicine (AAPM) have shown that approximately 60% of the lung cancer patients can not perform the DIBH technique successfully [40].

In this regard, the objective of this thesis is to propose a novel approach to implement and automate the respiratory amplitude gating technique in current PET/CT scanners that have the following characteristics:

- No patient non-compliance problem (patients breathe freely)
- No extensive interaction between patients and technologists
- No increase in X-ray radiation exposure

- No requirement of deformable registration
- Most important: motion amplitude match in CT and PET scans

This proposed technique has the advantages from both the 4-D PET/CT acquisition and the DIBH technique, and is able to automatically match the motion amplitudes that are captured during the CT and PET scans. This proposed automatic respiratory amplitude gating approach, which will be referred to as the free-breathing amplitude gating (FBAG) technique, will be described and evaluated in Chapter 2. Chapter 3, on the other hand, will introduce an in-house cost-efficient respiratory gating device that is used to facilitate the implementation of the proposed FBAG approach.

1.5 Secondary Focus: Partial Volume Effect

1.5.1 Introduction to partial volume effect in PET/CT imaging

Besides respiratory motion artifacts, partial volume effect (PVE) is another important factor in PET/CT imaging that can degrade PET/CT image quality and image quantification. This effect is primarily caused by the finite spatial resolution of the PET scanners which prevents accurate quantification for objects with size comparable and smaller than about two to three times the full width at half-maximum (FWHM) of the scanner's point spread function (PSF). This loss of quantitative accuracy for hot and cold spot contrast recovery is first recognized by Hoffman and Kessler [41-43]. Due to the existence of the partial volume effect in PET imaging, a small object will look blurred

and its activity concentration will spread into its surrounding image pixels in the resultant PET image as shown in Figure 1.16.

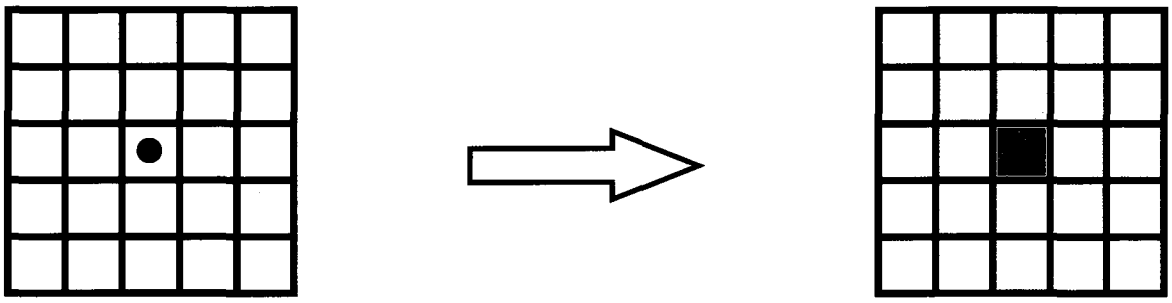

Figure 1.16: Partial Volume Effect due to the finite spatial resolution of PET scanners.

The PVE in PET/CT imaging is primarily caused by the finite spatial resolution of PET scanners. Compared to other imaging modalities such as CT, MRI and Ultrasound, the spatial resolution of PET scanners is pretty low. Currently, high-resolution PET scanners usually have a spatial resolution of 4.5 to 6 mm, while CT scanners can achieve a spatial resolution of less than 1 mm. PET image resolution is limited by physical parameters such as random, scatter, quantum noise, positron range, non-colinearity, motion as well as by the intrinsic spatial resolution of PET detectors [21]. The resolution of the final reconstructed PET image is even poorer than the best obtainable, intrinsic resolution because reconstruction algorithms typically trade off resolution for reduced noise. Either reconstructed using back-projection or EM-type algorithms, PET images contain much higher noise than the corresponding CT images, since the total counts of gamma photons that PET detectors accept are limited due to the short period of scan (usually 3-5 minutes scan clinically for each bed position).

Due to the existence of PVE in PET imaging, small objects will look blurred and its activity concentration will spread into its surrounding image pixels in the resultant PET images. As a matter of fact, even large object can be affected by this partial volume effect while the sharp edges of the objects will become blurred. A good example of such effect is shown in Figure 1.17. This figure clearly shows that the object size has a very influential impact on the partial volume effect. When the object size is larger, i.e. larger than twice of the full width at half-maximum (FWHM) of the PET scanner, the edges of the object will look blurred, however, the center part of the object still can display the same activity concentration as originally injected. On the other hand, when the object size becomes smaller, i.e. smaller than twice of the FWHM of the PET scanner, the object can not even recover the true activity concentration as originally injected. This under-estimation of the PET activity concentration will result in inaccurate PET quantification which eventually leads to incorrect tumor diagnosis and treatment.

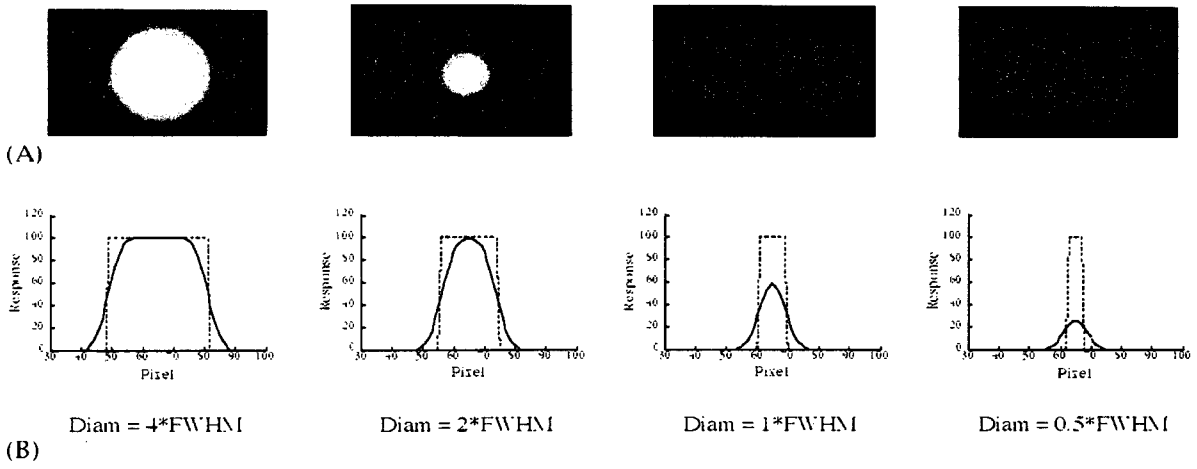

Figure 1.17: Partial Volume Effects in PET images due to the finite spatial resolution of PET scanners. As the object size becomes smaller and smaller, the object in the PET images will become more and more blurred. When the object size is less than twice the full width at half-maximum (FWHM) of the PET scanner, the original activity concentration can not even be recovered and thereby introducing quantification errors in the resultant PET images.

1.5.2 Partial volume correction techniques

In an attempt to minimize the quantification errors due to the partial volume effects, the maximum activity concentration (ACmax) or maximum standardized uptake value (SUVmax) within a region of interest is often preferred over the volumetric mean activity concentration (ACmean) or mean SUV (SUVmean). Both are semi-quantitative measures of radiopharmaceutical uptake but PVE can cause more pronounced underestimations of mean values than of the maximum values. However, the choice of ACmax/SUVmax can be problematic because it is sensitive to noise and will be biased by definition. In addition, ACmax/SUVmax indicates uptake only in a single pixel or a small group of pixels. The tumor, however, may have very heterogeneous uptake, and its heterogeneity may change with time or therapy. A further advantage of the ACmean/SUVmean is that there is faster convergence of mean values compared with maximum values with iterative reconstruction. Thus, a measurement over the entire volume of interest (VOI) with correction for partial volume effects would be ideal.

Approaches that were proposed for correcting PVE can be classified into two categories. The first category uses a higher-resolution anatomic image from CT or MRI to define the tumor boundaries. In this case, correction for partial volume effect involves using the anatomic information in the image reconstruction [44] or as a model to simulate the spill-in and spill-out effects of radioactivity to and from the VOI [45,46]. One disadvantage of these methods is that they require very accurate registration of the PET and the CT or MR images at the region of interest. Inaccurate segmentation or mis-registration can contribute to errors in the correction of partial volume effect. The error due to the mis-registration between the PET data and CT data is especially obvious in

lung canner patients because lung lesions are moving along with the organs due to the patient's respiratory motion. The second category of correction techniques also uses anatomic information, either from an additional modality (CT or MRI) or from the PET data itself. In this method, one corrects for partial volume effect from knowledge of how PVEs affect radionuclide quantification in tumors of various sizes and background levels. A common correction technique uses a calibrated table of correction factors [47] based on phantom measurements to adjust the ACs or SUVs. However, it is not easy to estimate the true metabolic size from the apparent size of the PET image and frequently one must assume that the tumor shape is the same as the phantom shapes studied. In addition, one needs to know the background level in the vicinity of the tumor to account for spillover from background to tumor, which can be problematic if the tumor is located close to organs with high uptake.

Since the patient's lung lesions suffer from both the respiratory motion artifact and partial volume effect in PET/CT imaging, we will propose and test a joint correction approach that can simultaneously compensate for both of the two effects. The description and evaluation of this joint correction approach will be discussed in Chapter 4.

1.6 Forward to the Thesis

In this Ph.D thesis, the author will propose, implement and evaluate approaches to compensate for the respiratory motion artifact as well as partial volume effect in PET/CT images. This thesis consists of three sections: (1) Automation of a Respiratory Amplitude Gating Implementation in Whole-body PET/CT Imaging, (2) Design and Performance of

a Respiratory Amplitude Gating Device for PET/CT Imaging, and (3) Joint-correction of Respiratory Motion and Partial Volume Effect in PET/CT Imaging. The first section focused on the methodology design of an automated respiratory amplitude gating approach that is used in whole-body PET/CT scanners. This respiratory amplitude gating approach is referred to as the free-breathing amplitude gating (FBAG) approach. In this section, phantom and patient studies are performed to evaluate this approach and the results from these studies are also discussed in this section. The second section of this thesis focused on the hardware and software design and implementation of an in-house cost-efficient respiratory gating device. This respiratory gating device can be used to facilitate the implementation and automation of the proposed FBAG approach in the first topic. This section will also describe the volunteer and phantom studies which are conducted to test the performance of this in-house device. This device has the added advantage of low cost and easy-to-use when compared to commercial respiratory gating devices that have similar performances. The third section of this thesis focused on the mathematical manipulation and algorithm design for a joint correction approach that can simultaneously compensate for the respiratory motion artifacts and partial volume effect (PVE) in PET/CT imaging. A simulation study as well as a phantom study is performed in this section to evaluate this technique. Conclusions and future works about this thesis will be discussed in the final chapter. With the description of the three sections, the primary contributions of this thesis are listed as follows:

1. An automated respiratory amplitude gating approach is proposed in order to implement the amplitude gating technique which is current unavailable in any PET/CT scanners. This approach can automatically match the respiratory

amplitude capture during CT and PET acquisition. This proposed approach does not suffer from the limitations of other existing respiratory gating techniques: increase of patient radiation exposure, inaccuracy of deformable registration, patient non-compliance problem, and extensive interaction between patients and technologists during PET/CT acquisition.

2. An in-house respiratory gating hardware/software system is designed and implemented. Compared to other commercially available device, this system is able to generate the necessary triggers while simultaneously monitoring the accumulated time within the preset amplitude range in order to facilitate the implementation of amplitude gating. This trigger generation scheme is unavailable in any other commercially available device.
3. A joint motion blurring and partial volume blurring correction approach is proposed which can improve the accuracy of PET image quantification by simultaneously eliminating the effects from the respiratory motion and PET finite spatial resolution in lung/thoracic PET/CT imaging. This joint correction approach is the first approach that simultaneously compensates for all of the following effects in one single correction process: PET-CT mismatch, PET motion blurring, and finite spatial resolution of PET scanner.

Chapter 2

Automation of Respiratory Amplitude Gating Implementation in Whole-body PET/CT Imaging

Objective Amplitude gating techniques have recently been shown to be better at suppressing respiratory motion artifacts than phase gating. However, most commercial PET/CT scanners are equipped with only phase gating capabilities. The objective of this project is to propose and evaluate using phantom and patient studies an automated respiratory amplitude gating technique that can be implemented on current whole-body PET/CT scanners. A primary design feature of the proposed technique is to automatically match the respiratory amplitude captured during the CT scan with a corresponding amplitude during the PET scan.

Methods The proposed amplitude gating technique consists of a CT scan followed by a list-mode PET scan. The CT scan is acquired while the patient's respiratory motion is recorded by a monitoring device that determines the respiratory amplitude captured during the CT scan. A Labview® software program is designed to inject triggers into the PET list stream whenever the patient's respiration crossed a selected amplitude range determined by the captured amplitude during CT. To implement this amplitude gating approach in whole-body PET/CT scan, a PET-first protocol is necessary in order to minimize the respiratory baseline drift between the CT and PET scans. In this implementation, a regular PET scan is first acquired over the patient's whole body but excluding the bed position that covers the lesion of interest. The whole-body CT scan is then acquired followed by a list-mode PET acquisition over the bed

position that covers the area of interest (lesion). The above procedures have been automated on current PET/CT scanners using a Labview® software program. The performance of this automation method was tested using a phantom study as well as13 patients with 21 lung/thoracic tumors.

Results The results from the phantom study showed that the amplitude gated image matched the CT anatomic information and had an average of 88%, 37% and 22% improvement in contrast, max and mean activity concentration respectively when compared to the ungated PET images. The spheres in the gated images showed better contrast using visual inspection and line profiles. In the patient studies, statistically significant improvements were whereby the gated images had an average 27% and 28% increase in max and mean SUV for all lesions when compared to the ungated images. Furthermore, the tumors in the gated images showed better contrast using visual inspection and line profiles.

Conclusion The implementation of the proposed respiratory amplitude gating technique has been automated with minimal user interaction on current PET/CT scanners. Amplitude matched CT and PET data are automatically generated using our proposed procedures without requiring patients to hold their breath or increase the X-ray exposure.

2.1 Introduction

PET/CT imaging is increasingly being used to facilitate the diagnosis, staging and restaging of patients with a wide variety of cancers [48-50]. This is largely due to the ability of this imaging modality to provide anatomic and functional information about the

underlying disease state. Furthermore, the addition of the CT component to PET scanners has also provided an efficient attenuation map which has greatly reduced the total scan duration and increased the scanner's throughput [51]. However, the addition of CT to PET imaging has also introduced some disadvantages. In a PET/CT study, the CT scan captures the patient breathing cycle in a single state [52, 53], while the PET scan is usually acquired over many breathing cycles due to its longer acquisition time [54]. This discrepancy introduces a mismatch between the CT and PET images which results in mis-localization of small lesions and inaccurate quantification of the standardized uptake value (SUV) [55-57]. These effects eventually compromise the diagnostic accuracy of PET/CT imaging and might result in patient mismanagement.

To overcome respiratory motion artifacts in PET/CT imaging, PET respiratory gating techniques have been proposed [58-63]. These techniques can be divided into two categories: phase gating and amplitude gating [29], with phase gating being the only option available on current commercial PET/CT scanners. In phase gating, the respiratory cycle is divided into multiple phase ranges (or bins) and the acquired data is sorted into each phase range based on its acquisition time within the respiratory cycle. This approach works well for patients with regular breathing but results in large errors in patients that have irregular respiration (frequency or amplitude) primarily due to the introduction of large amounts of motion in each bin [29]. Recently, amplitude gating has been proposed as an alternative approach to phase gating [29]. Rather than dividing the respiratory cycle into different phase ranges, amplitude gating divides the respiratory amplitude into different amplitude ranges. In this regard, motion artifacts in phase gating are suppressed

with amplitude gating. However, amplitude gating is currently unavailable on any commercial PET/CT scanner.

Approaches to implement amplitude gating on commercial PET/CT scanners are currently being investigated by many research groups [64-67]. Some of the suggested methods rely on 4-D PET imaging whereby the acquired PET data are retrospectively sorted into multiple amplitude ranges by using commercial respiratory gating devices. The corresponding reconstructed images are then also retrospectively registered to one another to generate a motion-free image that is characterized by good signal-to-noise ratio (SNR) [64, 65]. Other methods, known as motion-incorporated reconstruction techniques, are focused on incorporating the motion information between the different bins of the 4-D PET images into the statistical reconstruction algorithm to reduce motion artifacts while maintaining good SNR [66, 67]. Both of these methods, however, require an additional 4-D CT scan, which is characterized by an increased patient radiation exposure, to attenuate-correct the corresponding 4-D PET data. Furthermore, the implementation of these methods also relies on deformable image registration techniques that might not result in accurate image registration due to the low SNR of the different PET bins or inconsistency in respiratory motion between CT and PET images. Recently, deep-inspiration breath-hold (DIBH) techniques have been proposed as a variant of amplitude gating without the need to register the 4-D PET images or increase patient exposure [37-39]. In DIBH, patients are requested to hold their breath at deep inspiration for a relatively short period while both the CT and PET data are acquired. PET data acquisition in this respiratory state is then repeated multiple times in order to accumulate a sufficient amount of counts per pixel [37, 38]. The resultant multiple PET data sets are

then summed together to generate a motion-free sinogram which is then attenuation-corrected by the corresponding CT image and eventually reconstructed into a motion-free image. The net result is a PET image that is matched in respiratory amplitude with a corresponding DIBH CT image. DIBH has been demonstrated to be feasible on current PET/CT scanners [37-39]. However, a main disadvantage of this technique is ensuring patient compliance to hold their breath for the specified time and amplitude in each respiratory session particularly when the patients are at an increased state of anxiety due to their medical condition. Another disadvantage of DIBH is its extensive reliance on technologist-patient interaction to coordinate data acquisition during the multiple repetitive times to accumulate the necessary data particularly with patients that have hearing or language barriers. Furthermore, recent studies have shown that approximately 60% of the lung cancer patients can not perform the DIBH technique successfully [40].

In this project, we propose a novel approach to implement respiratory amplitude gating in whole-body PET/CT scanners that does not require any patient coaching or compliance with specific breathing conditions while maintaining the advantages of DIBH namely no increase in X-ray exposure nor deformable image registration. The main emphasis of this new approach is to perform respiratory amplitude gating with minimal patient and user interaction while at the same time minimizing data post-processing tasks. The proposed approach is similar to DIBH except that the respiratory amplitude range during the PET imaging is automatically selected to match the breathing amplitude captured during the CT scan. In this approach, patients are allowed to breathe freely during the CT acquisition. The respiratory motion amplitude that is captured during the CT scan is then automatically used during PET imaging in such a way that only PET data

falling within a corresponding amplitude range are used to generate the final PET image. In this regard, the drawbacks of the 4-D PET/CT acquisition and DIBH technique such as difficulty of 4-D PET registration, high patient X-ray exposure, and patient's non-compliance will be eliminated. The objective of this project is to describe how such a respiratory amplitude gating scheme can be automated in whole-body PET/CT scanners and evaluate its feasibility in current PET/CT scanners using phantom and patient studies. The proposed automation of the amplitude gating approach and the setup of the phantom and patient studies will be described in section 2.2 and the results of these studies will be presented in section 2.3. Further considerations regarding this approach are discussed in section 2.4. Section 2.5 concludes this project.

2.2 Materials and Methods

2.2.1 The Automatic Respiratory Amplitude Gating Approach

To automate the proposed amplitude gating approach on current commercial PET/CT scanners, two goals must be achieved without user interaction. First, the motion amplitude captured during CT imaging must be recorded, and second, a corresponding motion amplitude range should be selected during PET image acquisition. The reason for selecting an amplitude range rather than a single amplitude value during the PET scan is primarily to maximize the recorded count statistics at the corresponding CT amplitude while minimizing the total scan duration. In order to achieve these goals, we propose the following amplitude gating approach: (1) acquire a CT scan followed by a list-mode PET scan over the specific area of interest (usually a lesion in the patient's torso), (2) monitor

the patient's respiratory waveform during the CT scan and determine the breathing amplitude when the CT scan reaches the area of interest, and (3) extract from the list-mode PET only the data that are acquired when the patient's respiratory amplitude range coincides with the breathing amplitude captured during the CT scan. In this regard, the motion amplitude captured during the CT and PET scans are automatically matched with one another without any technologist-patient interaction. The list-mode PET scan is designed to be terminated when 3 minutes worth of extracted PET list-mode data is accumulated. The 3 minute worth of accumulated data is used based on our standard scan duration per bed position at our institution. The following paragraphs describe the procedures to implement and automate the proposed amplitude gating approach in whole-body PET/CT imaging as well as the hardware and software configuration needed to facilitate its implementation.

To apply the proposed amplitude gating approach to whole-body PET/CT imaging with multiple bed positions requires modification of the standard protocol of a PET/CT scan. Rather than acquiring the usual whole-body CT followed by a whole-body PET, the implementation of the proposed approach necessitates that the PET and CT scans corresponding to the area of interest (lesion) be temporally acquired as close as possible to one another. This is primarily to ensure that the patient's breathing amplitude pattern during CT remains similar (or as close as possible) to that during PET imaging. Based on our experience as well as others, there exists a baseline drift in the respiratory waveform of the majority of patients imaged with PET/CT. This drift however stabilizes within 10 minutes from the time the patient is positioned on the PET/CT couch. Figure 2.1 shows an example of a breathing waveform without and with baseline drift

respectively. The breathing waveform with baseline drift stabilized within a short period of time (5-10 minutes).

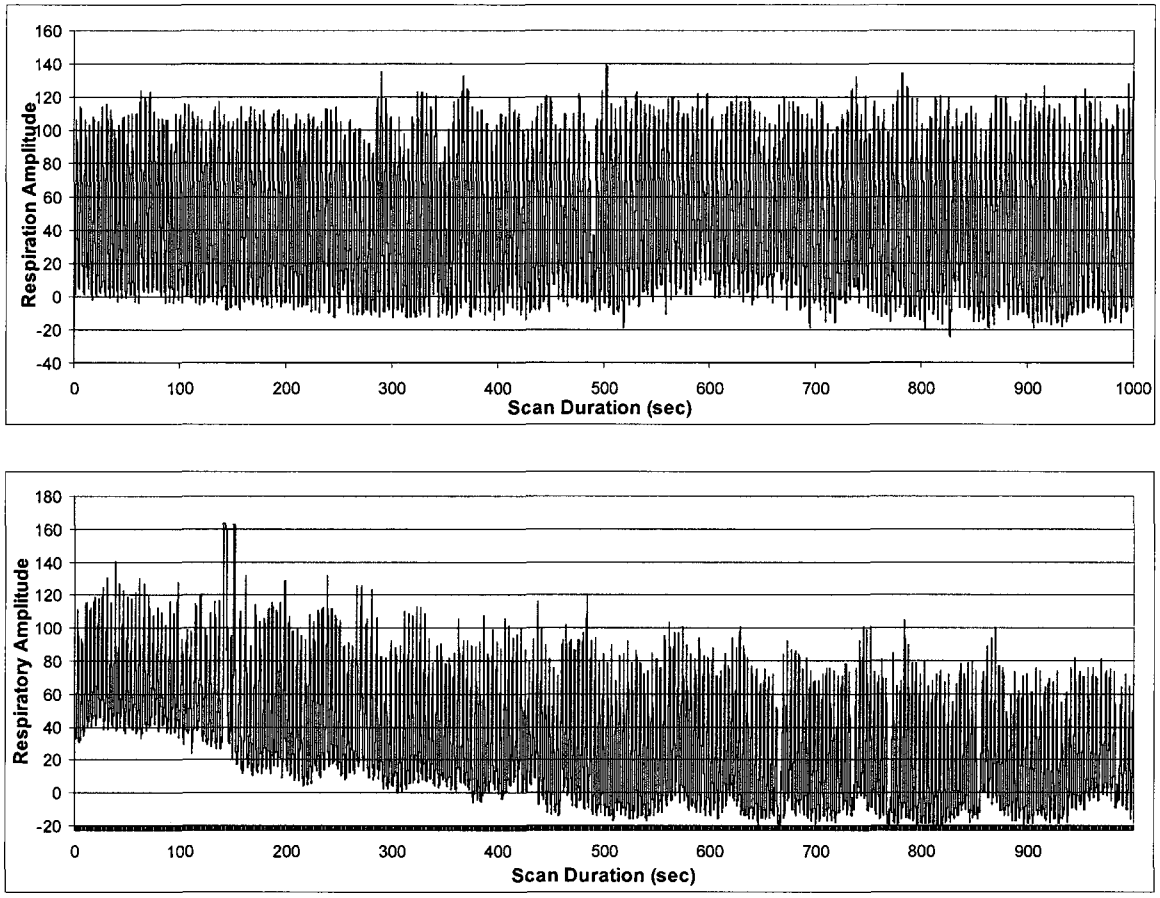

Figure 2.1: A breathing waveform without and with baseline drift respectively.

In this regard, in order to minimize the effect of this drift on matching the respiratory amplitude during the CT and PET over the area of interest (lesion location) while at the same time acquire a whole-body PET/CT, the proposed amplitude gating approach for whole-body PET/CT imaging will be based on a "PET-first" protocol as shown in Figure 2.2. In this design, the data acquisition is divided into three steps: (1) a regular PET scan over the patient's whole body but excluding the bed position that covers the lung or thoracic lesion of interest, (2) a regular whole-body CT scan, and (3) a single-

bed list-mode PET data acquisition over the area of interest (lesion location). The bed position over the area of interest is skipped in step (1) in order to reduce the overall scan duration since the same bed position is acquired in step (3). Using this protocol, the baseline drift problem of the patient's breathing cycle is automatically resolved since the duration of the regular PET scan (step 1) excluding the field-of-view (FOV) of interest usually takes 10-20 minutes (4-6 bed positions) which is long enough for the baseline drift to subside. Furthermore, the PET and CT acquisitions over the lesion location in this design are performed at close temporal proximity to one another to further minimize any remaining breathing variations.

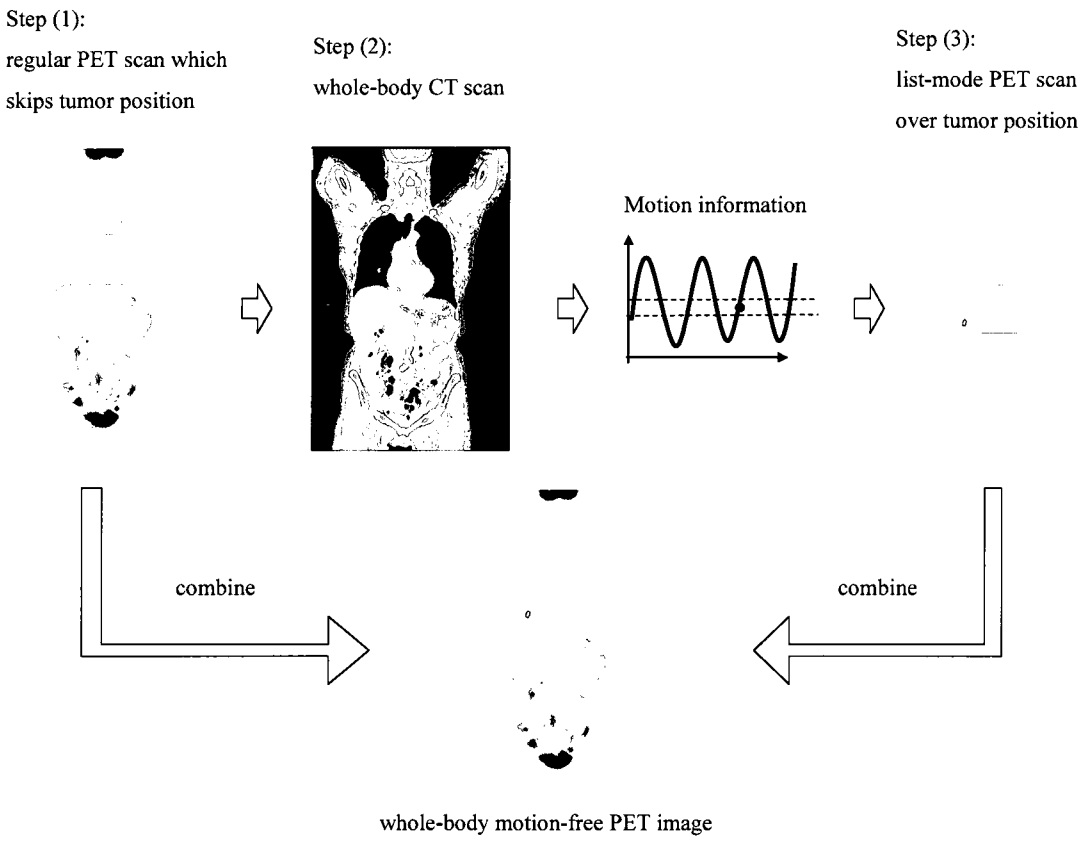

Figure 2.2: The procedures of the amplitude gating implementation. The whole-body PET/CT data acquisition process was divided into three steps: (1) a regular PET scan over the patient's whole body but excluding the bed position that covers the lung or thoracic lesion of interest, (2) a regular whole-body CT scan, and (3) a single-bed list-mode PET data acquisition over the tumor location.

Having ensured that the patient's breathing pattern during PET and CT is similar to one another, the next step in the process of implementing and automating the proposed approach is to first capture the respiratory amplitude during the CT scan and then match it to a corresponding amplitude range during the list-mode PET scan. Capturing the respiratory amplitude during the CT scan necessitates the identification of the tumor position on the CT image and the correlation of this position to the acquired patient's breathing waveform. To identify the tumor position, the whole-body CT scan is displayed to allow the technologist to select the axial slice corresponding to the center location of the tumor. The amplitude of the breathing motion corresponding to this slice location is then determined by correlating the patient respiratory waveform - as recorded by a respiratory gating device - with the start of the CT X-ray ON signal detected through a data acquisition device (both of which are described in section 2.2.2). Synchronization between the X-ray ON signal and the patient breathing cycle is performed by a trigger pulse from the respiratory gating device to the data acquisition device at the beginning of data acquisition. In this regard, the time associated with the X-ray tube passing the center of the tumor (T^R_{tumor}) can be determined from the patient's recorded breathing waveform according to:

$$T^R_{tumor} = T^R_{Trigger} + (T^D_{Xray} - T^D_{Trigger}) + T_{Xray->tumor} \tag{2.1}$$

where $T^R_{Trigger}$ and $T^D_{Trigger}$ represent the time of the synchronization trigger pulse recorded by the respiratory gating device and data-acquisition device respectively. The variable T^D_{Xray} is the starting time of the X-ray ON signal which is also recorded by the data-acquisition device while $T_{Xray->tumor}$ represents the duration from the beginning of the

X-ray ON signal until the X-ray tube passes the center of the tumor. This duration ($T_{Xray->tumor}$) is automatically determined from the location of the tumor on the CT image which can be read from the user's control panel of the PET/CT scanner. The time T^R_{tumor} calculated from (2.1) is then used to automatically search the recorded patient's respiratory waveform and determine the respiratory amplitude corresponding to T^R_{tumor}. This whole process is designed to occur following the acquisition of the whole-body CT scan and results in a motion amplitude that will be used to acquire a corresponding PET data.

Following the determination of the respiratory amplitude during the CT scan, the next step is to match this amplitude with a corresponding amplitude range of the list-mode PET scan. In order to achieve this aim, the respiratory gating device is configured to generate a gating signal whenever the patient's respiratory level falls within a ±10% range of the captured amplitude during CT. A list-mode PET scan is then acquired and automatically terminated when 3 minutes worth of PET data is accumulated within the selected amplitude range. Triggers are simultaneously injected into the PET list stream on both the beginning and ending stages of the selected amplitude range (section 2.2.2). The resultant PET list-mode data is then post-processed (details in section 2.2.2) to generate an amplitude-gated PET image. This gated image can be directly attenuation corrected by the whole-body CT data since the motion amplitudes captured in these two scans are matched with one another.

To summarize, in order to implement the proposed amplitude gating approach on current PET/CT scanners, a regular whole body PET scan is first acquired with 3 minutes per bed position (the 3-minute duration is similar to the standard scan duration per bed

position used at our institution) while skipping the bed position of interest. The a-priori knowledge of which bed position should be skipped can be derived from previous PET/CT scans of the patient or images from other diagnostic imaging modalities. Following the regular PET scan, a whole-body CT scan is then acquired while the respiratory amplitude at the time the CT scan reaches the tumor position is derived by correlating the tumor position identified on the CT image with the patient's respiratory waveform. In order to match the motion amplitudes during the CT and PET, a list-mode PET scan is then acquired over the bed position of interest while triggers are injected into the PET list stream whenever the patient's respiratory level crossed the edges of an amplitude range that is determined by the amplitude captured during CT. The resultant PET list-mode data is then post-processed and reconstructed to generate an amplitude-gated PET image after attenuation correction by the CT image. Similarly, the regular PET data is also attenuation-corrected by the CT image and is reconstructed. The regular PET image as well as the amplitude-gated image can then be combined together to generate a whole-body "motion-free" image. A flow chart of the above process for the amplitude gating implementation in whole-body PET/CT imaging is shown in Figure 2.3.

The whole process of this amplitude gating implementation, except for the identification of the tumor location from the CT image and the configuration of the respiratory gating device to output gating signals based on the selected amplitude range, is automatically performed using in-house written Labview® programs without additional user interference. Furthermore, the respiratory motion amplitudes captured during the CT scan and the amplitude-gated PET image are also automatically matched with one another without user interaction. Therefore, this amplitude gating implementation can be

automated on current PET/CT scanners. In this project, a phantom study as well as 13 patient studies will be conducted to test this amplitude gating automation approach and evaluate its ability to reduce respiratory motion artifacts.

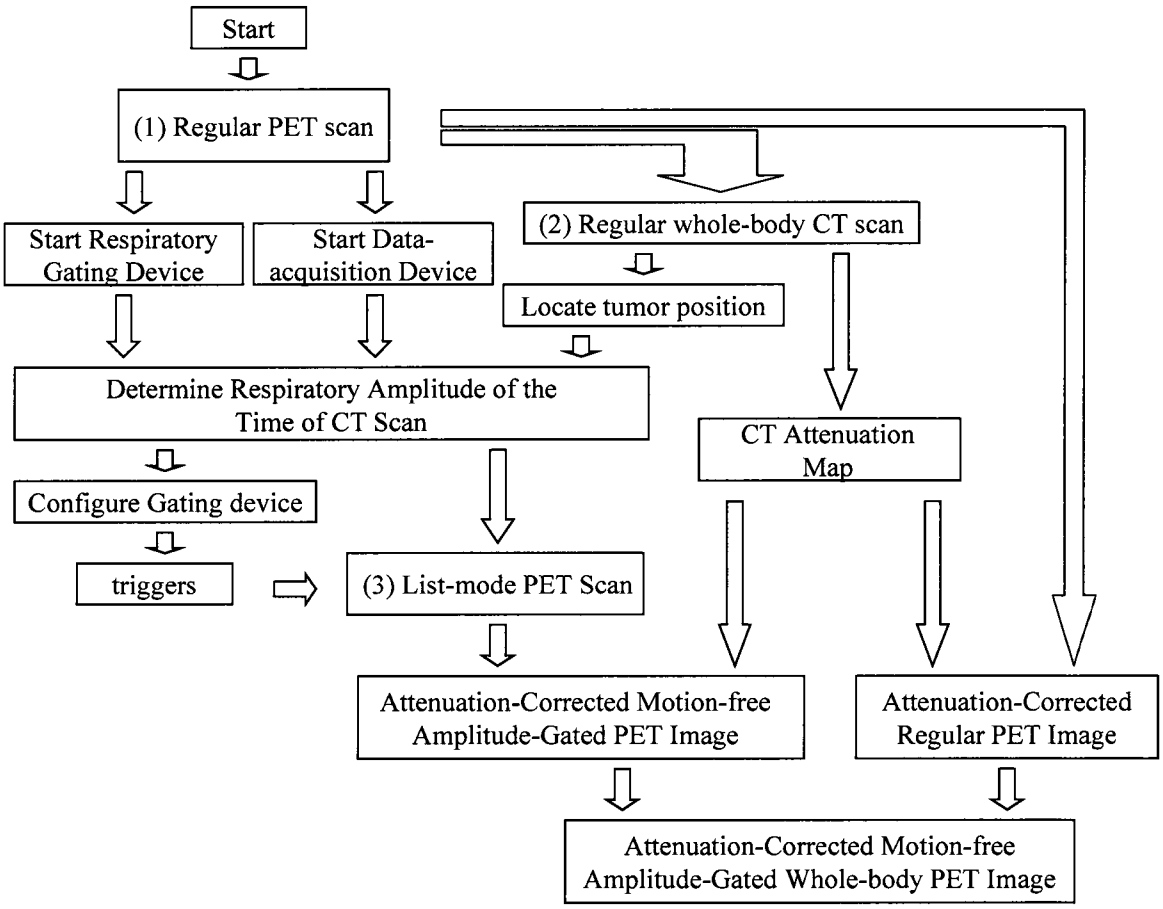

Figure 3: Flow chart of the automation approach to implement respiratory amplitude gating in whole-body PET/CT imaging.

2.2.2 Respiratory Gating Device

The respiratory gating device that was used in this paper is the Anzai device (AZ-733V; Anzai Medical Co. Ltd.). This device monitors the patient's breathing cycle via a pressure sensor placed in a belt secured around the patient's torso. This respiratory gating

device is comprised of the following components: (1) A strain gauge respiratory sensor, which tracks the pressure changes due to the patient's respiratory motion and generates a continuous respiratory signal, (2) A sensor port, which amplifies and transmits the analog signals generated by the sensor, and (3) A wave deck, which receives and digitizes the signals from the sensor port and send the digital signal to a personal computer. The respiratory sensor, sensor port, and wave deck are shown in Figure 2.4(a).

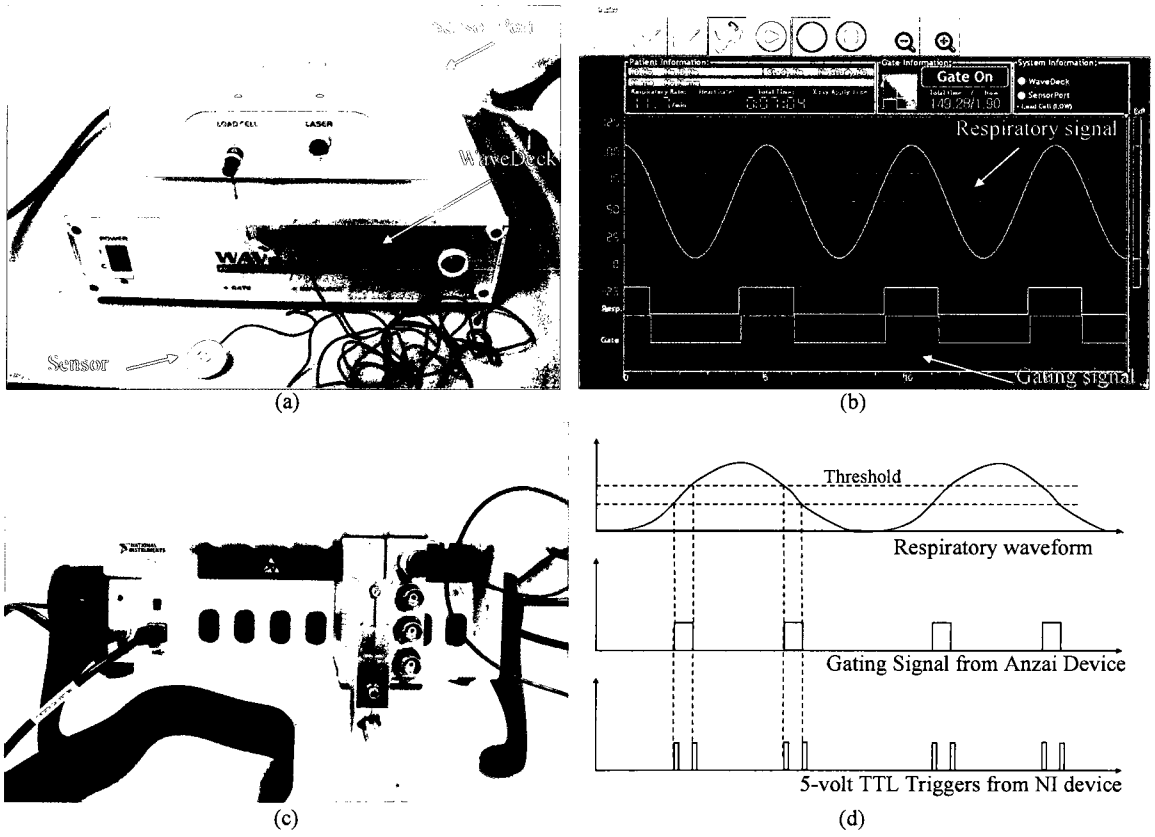

Figure 2.4: (a) The Anzai respiratory gating device: respiratory sensor, sensor port and wave deck, (b) the Anzai software showing a continuous gating signal is generated whenever the respiratory amplitude exceeds 75%, (c) NI-cDAQ-9172 device, and (d) the relationship between the respiration signal, gating signal from the Anzai system and triggers from the Labview® program.

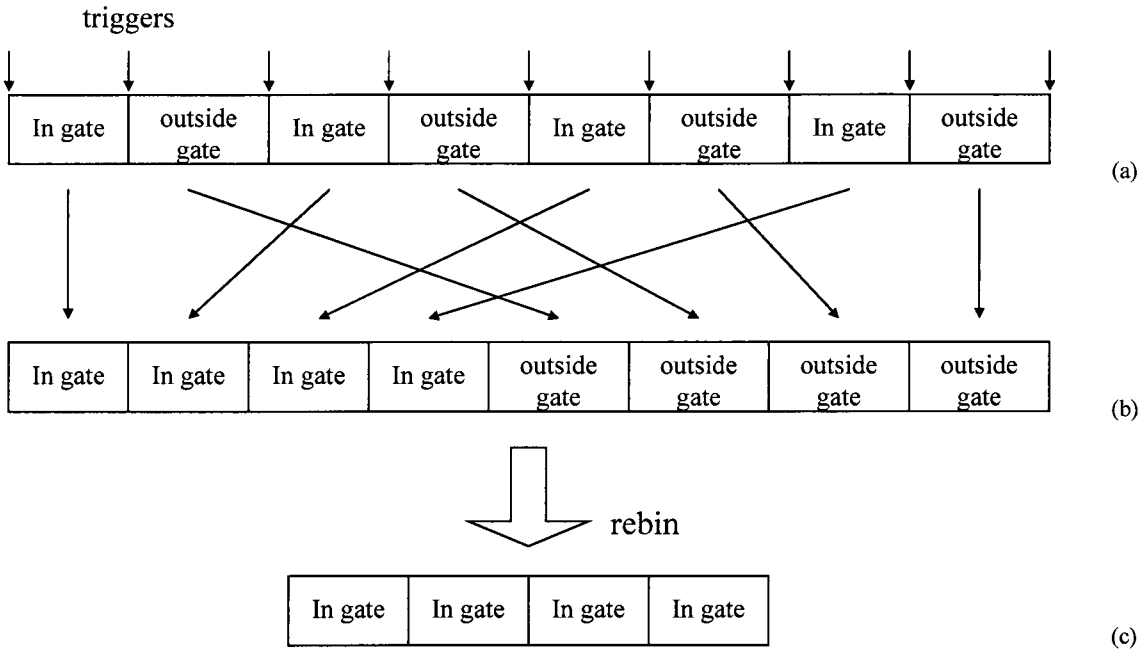

Figure 2.5: (a) The structure of the PET list-mode data with associated triggers after data acquisition, (b) list resorting process, and (c) data rebinning process.

A software program (Figure 2.4(b)) which controls and manipulates the measured signal is installed on a personal computer and is provided with the respiratory gating device. This software has the capability to generate a continuous gating signal whenever the detected motion waveform falls within a selected amplitude range. This software also has the ability of monitoring the total scan duration and the time accumulated in the preset amplitude range. However, in order to match the motion amplitude captured during CT with a corresponding amplitude range during PET, the Anzai device should send a trigger signal on both the beginning and ending stages of that preset amplitude range. Unfortunately, the Anzai device (as well as other respiratory monitoring devices) can not be configured to perform that task while simultaneously recording the accumulated time within the preset amplitude range. In this regard, the continuous gating signal from the Anzai device was coupled to a NI-cDAQ-9172 device (National Instruments, Austin, TX)

(Figure 2.4(c)) and a Labview® program was designed to inject a trigger into the PET list stream whenever it detected the rising and falling edges of the gating signal. The relationships among the respiration signal, the gating signal from the Anzai device and the triggers from the Labview® program are shown in Figure 2.4(d).

The structure of the resultant PET list stream with associated triggers is shown in Figure 2.5(a). The PET list stream contains alternating segments of data separated by triggers that were acquired within and outside the preset amplitude range (or gate). This list-mode data can then be post-processed by either rebinning as a static scan or filtered in such a way to generate a contiguous stream of PET list data acquired only within the preset amplitude range. This filtering process is necessary since the rebinning function of the PET/CT scanner can not be configured to only select events that were acquired within the preset amplitude range. In this regard, a list-resorting program was written (using the C computer language) and used to resort the list data in such a way that all events acquired at different breathing cycles but within the preset amplitude range were placed contiguously and in a chronological order in front of events that were acquired outside the selected amplitude range (Figure 2.5(b)). The list-resorting program was also designed to output the total amount of time accumulated within the selected gate. The resorted list file was then processed by the data-rebinning function of the scanner to extract the portion that was only acquired within the gated amplitude range (Figure 2.5(c)). Since the extracted PET data only contained information that was acquired when the respiratory waveform fell within the gate, it can be directly reconstructed to generate an amplitude-gated PET image after attenuation correction. An alternative approach to process the acquired list-mode data is to store the recorded data into two different

memory locations corresponding to within and outside the amplitude range respectively using a prospective gating scheme. This approach however, requires the modification of the configuration of current PET/CT scanners and therefore is not used in this paper.

2.2.3 PET/CT Scanner

A GE Discovery RX PET/CT scanner (GE Healthcare, Waukesha, Wisconsin, USA) was used in this paper. The PET gantry of this scanner consists of 24 rings of 630 detector crystals and has a trans-axial field-of-view (FOV) of 70 cm. The CT component of this scanner has a 50 cm trans-axial FOV. The description and performance characteristics of this PET/CT scanner have been published elsewhere [68]. All data in the patient studies were acquired in 3D mode and were corrected for attenuation, random, scatter and dead time and reconstructed using 3D OSEM algorithm (2 iterations, 21 subsets).

2.2.4 Phantom Study

The objective of the phantom study is to test the proposed automation approach of the amplitude gating implementation and evaluate its ability to reduce respiratory motion artifacts.

A phantom consisting of one stationary (33 mm) and two moving spheres (33 and 22 mm) placed in a water tank was used. The stationary sphere was fixed to the bottom of the tank, while the two moving spheres were attached to a computer-controlled platform [69]. The platform was driven by a sinusoidal wave and translated the two spheres in the axial direction. The input waveform had a 2 cm peak-to-peak amplitude and a period of 5

seconds. The three spheres as well as the tank were filled with ^{18}F-FDG water with a sphere-to-background contrast ratio (SBR) of 5.7:1. The activity concentration in the background was 2.8 kBq/cc. The setup of the phantom study is shown in Figure 2.6.

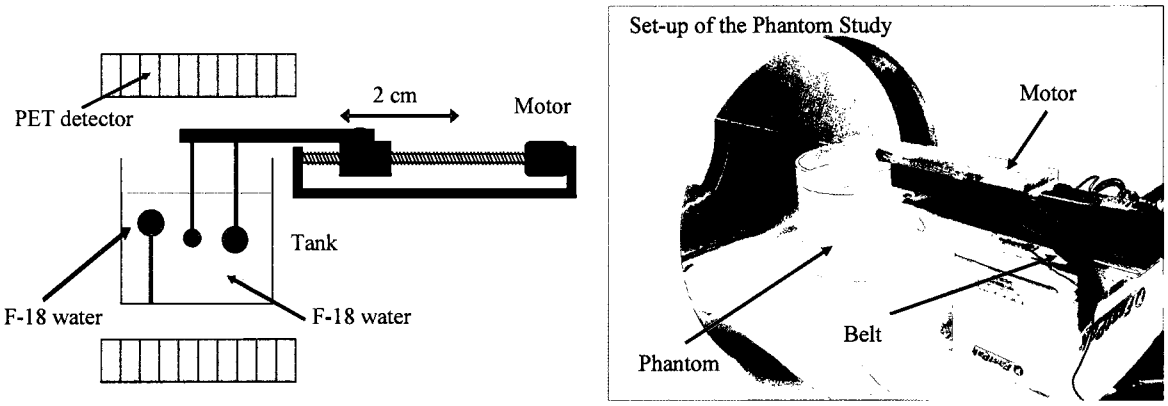

Figure 6: The setup of the phantom study.

The phantom was positioned centrally in the FOV of the PET/CT scanner and a three-bed protocol was selected to image the phantom, with each bed position covering 15.7cm. The location of the three spheres fell within the second bed position. This configuration approximated a multi-bed whole-body PET/CT scan with the patient's torso occupying the second bed position. The pressure sensor of the Anzai device was attached to the moving platform via an elastic belt and the phantom was imaged based on the procedure described in section 2.2.1 data acquisition in 2-D mode was used for both the regular and list-mode PET scans. In this investigation an amplitude range of 80-100% of the maximum motion amplitude was selected which coincided with the sphere motion amplitude (91% of the maximum amplitude) captured during the CT scan. During the list-mode PET scan, the Anzai software was configured to monitor the total time the moving spheres were within the 80-100% motion amplitude range and stop the scan

when 3 minutes worth of data were accumulated. This imaging paradigm resulted in a total acquisition time of 12 minutes for the list-mode PET scan.

The acquired list-mode data was then rebinned as a static scan (ungated) of 3 and 12 min respectively and reconstructed using OSEM algorithm (2 iterations, 21 subsets). The 12 min ungated image was generated since it consisted of all the acquired data while the 3 min ungated image was reconstructed because this duration is similar to the standard scan duration per bed position used at our institution. Furthermore, the same list-mode data was post-processed (section 2.2) and then reconstructed using the same algorithm to generate the 3 min amplitude gated image. The ungated 12 min, ungated 3 min, and amplitude gated 3 min images were then compared to one another using visual inspection. The CT anatomic information of all the spheres (location and size) was superimposed on the PET images to evaluate their positions with respect to the PET images. Line profiles were also drawn along the three spheres on both the PET and CT images. Maximum and mean activity concentration (AC) as well as the contrast ratio (CR) were then determined from the line profiles for all spheres. The mean AC was defined as the average pixel value of a region-of-interest (ROI) drawn on the sphere based on the corresponding CT image. The ROIs for the moving spheres were shifted by 1 cm (half the motion amplitude) along the motion direction of the sphere in the ungated images to account for the mismatch between the CT and ungated PET images. The contrast ratio was defined as:

$$CR = (P - T)/P \tag{2.2}$$

where P and T represent the *peak* and *trough (valley)* value across the line profile of the sphere respectively. All ACs and CRs are normalized to the AC and CR of the stationary

sphere in the ungated 12 min image. The improvements in maximum AC, mean AC and CR for the moving spheres on the gated images versus ungated images were also calculated.

2.2.5 Patient Studies

The objective of this paper is to test the proposed automation approach of the amplitude gating technique in clinical PET/CT patient studies. An institutional review board (MDACC IRB #2008-0851) was first acquired prior to the patient studies.

13 patients (5 male and 8 female, age 64±9 years old) referred for PET/CT evaluation of lung or thoracic lesions were selected to test the performance of the proposed amplitude gating approach. All patients fasted for 4 hours prior to being injected intravenously with 296-444 MBq (8-12 mCi) of ^{18}F-FDG. Imaging started 60-90 minutes post injection. The amplitude gating procedures described in section 2.2.1 was applied in these studies while the whole imaging process consisted of a regular PET scan covering 4 to 6 bed positions (excluding the bed position that covered the tumor-of-interest) depending on the patient's height, a whole-body CT scan, and a list-mode PET scan of one bed position which covered the tumor location. During the list-mode PET scan over the tumor location, the Anzai device was configured to monitor the total time the tumor fell within the preset amplitude range and stopped the scan when either 3 minutes worth of data were accumulated in the selected amplitude range or a maximum of 10 minutes of scan duration was reached. This stopping condition resulted in an average of 8.3 minutes of list-mode PET scan duration and 2.6 minutes duration within

the gate for all of the 13 patients. The information on the patients and their scan conditions are summarized in Table 2.1.

TABLE 2.1
Summary of Patient Characteristics and PET/CT Imaging Conditions

Patient ID	Sex	Age (y)	No. of tumors	Lesion site	No. of FOV in regular PET scan	List-mode PET scan duration (min)	Accumulated time within gate (min)
1	F	65	2	Left lower & right lower robe	5	10	2.4
2	M	81	2	Left lower & right lower robe	5	10	1.8
3	F	66	1	Upper liver	6	10	2.2
4	M	64	1	Upper liver	5	8.9	3.0
5	F	47	2	Right middle lobe, close to rib	6	5.6	3.0
6	F	54	1	Left lower lobe	6	10	2.1
7	F	57	1	Left upper lobe	6	10	2.2
8	F	60	1	Left middle lobe	4	5.8	3.0
9	F	68	2	Left upper & lower lobe	5	8.7	3.0
10	M	65	3	Right upper lobe & upper liver	5	4.3	3.0
11	M	71	1	Upper liver	6	5.6	3.0
12	F	71	2	Middle rib	4	10	2.4
13	M	69	2	Upper liver	6	8.8	3.0
Average	--	64	--	--	--	8.3	2.6

The acquired regular PET scan for each patient was then reconstructed using a 3D OSEM algorithm (2 iterations, 21 subsets) after attenuation correction by the CT image. In addition, the list-mode PET data was first post-processed (section 2.2.2) and then reconstructed using the same algorithm to generate the amplitude-gated image. This amplitude-gated image was combined with the regular PET image to generate a "motion-free" whole-body PET image. For comparison purposes, the same list-mode data was rebinned as a 3-minute static scan (without resorting), reconstructed using the same algorithm and combined with the regular PET image to generate an ungated whole-body PET image. The amplitude-gated and ungated images were compared to one another

using visual inspection and line profiles. The maximum SUV, mean SUV, lesion SNR and lesion volume were determined for all lesions. The mean SUV and lesion volume of each lesion were calculated based on a region-of-interest determined using a 40% maximum SUV threshold. The lesion SNR was defined as the mean SUV of the lesion divided by the SUV standard deviation of a region-of-interest drawn in the lung. A statistical T-test was performed to evaluate the significance of the improvement in maximum SUV, mean SUV, lesion SNR and lesion size on the gated images versus the ungated images.

2.3 Results

2.3.1 Results from the Phantom Study

The two moving spheres in the ungated 12 min, ungated 3 min and amplitude gated 3 min images are shown in Figure 2.7 (a)-(c) respectively. The corresponding images for the stationary sphere are shown in (d)-(f) respectively. Circles are superimposed on these images to represent the locations and sizes of the spheres on the CT images. Comparison between PET images and the CT anatomic information indicates that the two moving spheres in the gated PET images match well with their locations in the CT image, while in the ungated PET images (12 min and 3 min), the two spheres appear to be smeared and extend beyond their actual size in the CT image. The stationary sphere, however, matches well with its location in the CT image as expected in all of the three images.

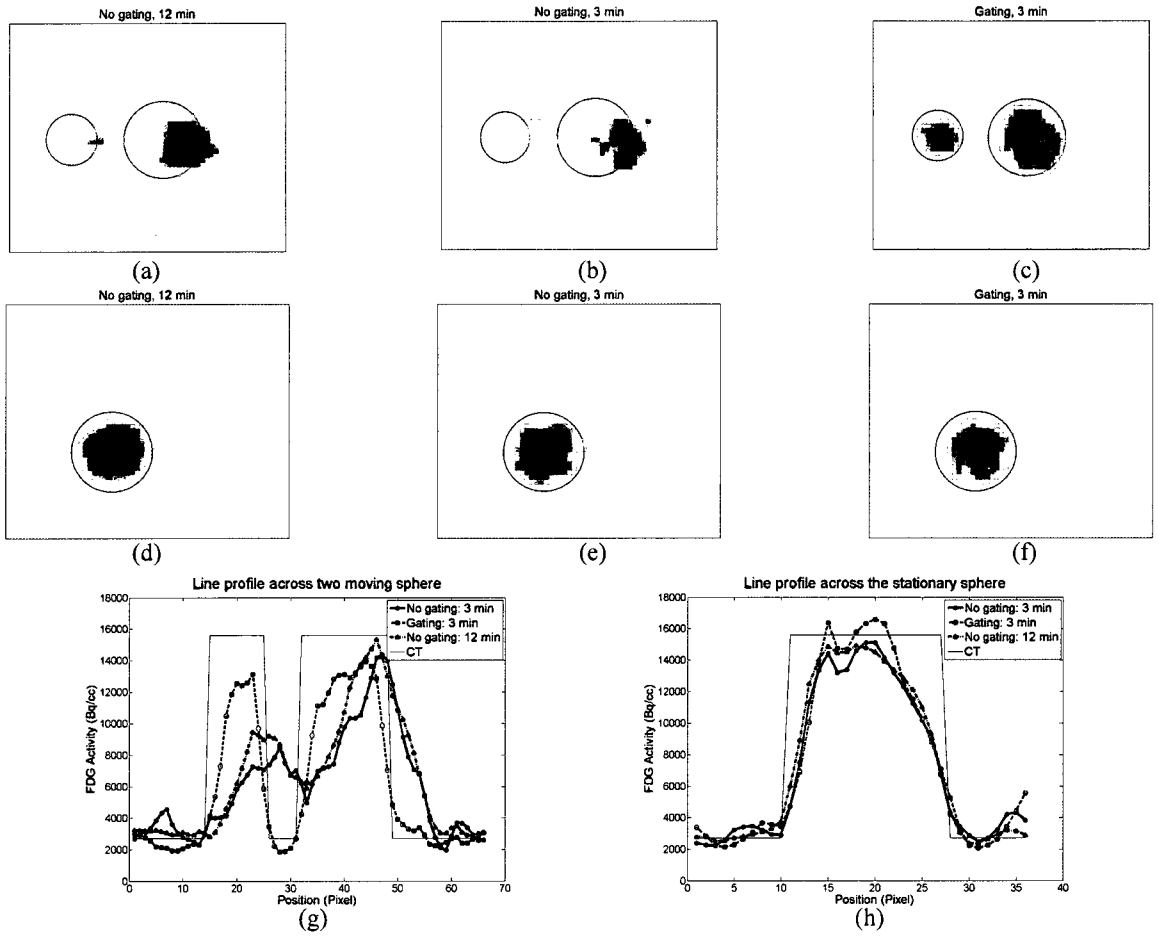

Figure 2.7: The two moving spheres for the (a) ungated 12min, (b) ungated 3min, and (c) amplitude gated 3min image. The corresponding stationary spheres are shown in (d), (e) and (f), respectively. The circles represent the positions of the spheres in the corresponding CT images. The line profiles across the two moving spheres and the stationary sphere are shown in (g) and (h), respectively.

From visual inspection, the two moving spheres are more blurred and elongated along their motion direction (axial direction) in the two ungated images (3 min and 12 min) when compared to the gated 3 min image. Furthermore, the stationary spheres in the three images show similar AC as one another. However, the background noise in these images is different as expected due to the difference in scan duration (3 vs. 12 minutes).

The maximum and mean ACs of the two moving and stationary spheres in the three PET images are summarized in Table 2.2(A). Data in this table is normalized to the

result of the stationary sphere in the 12 min ungated image. The improvements of the maximum and mean ACs in the amplitude gated image versus the ungated images (3 min and 12 min) are shown in Table 2.2(B). For the stationary sphere, the three images have similar mean and maximum AC as expected. For the 33 mm moving sphere, the amplitude gated image shows an average improvement of 10.9% and 5.2% in maximum and mean AC respectively compared to the two ungated images. These improvements increase up to 60.6% and 46.3% for the 22 mm moving sphere.

TABLE 2.2

(A) AC and CR Normalized to the 12min Stationary Sphere in Phantom Study
(*Data are normalized to the stationary sphere on the ungated 12min reference image*)

	Gated 3min	Ungated 3min	Ungated 12min
AC_{max} (Sphere 33mm)	1.12	1.03	0.99
AC_{max} (Sphere 22mm)	1.06	0.66	0.66
AC_{max} (stationary Sphere)	1.05	1.12	1.00 (ref.)
AC_{mean} (Sphere 33mm)	0.92	0.85	0.90
AC_{mean} (Sphere 22mm)	0.95	0.63	0.67
AC_{mean} (stationary Sphere)	0.97	0.96	1.00 (ref.)
CR (Sphere 33mm)	1.04	0.78	0.73
CR (Sphere 22mm)	1.05	0.52	0.45
CR (stationary Sphere)	1.05	1.00	1.00 (ref.)

(B) Improvement of AC and CR in Gated vs. Ungated Image

Improvement (%)	Gated 3min vs. Ungated 3min	Gated 3min vs. Ungated 12min	| Average |
AC_{max} (Sphere 33mm)	8.7%	13.1%	10.9%
AC_{max} (Sphere 22mm)	60.6%	60.6%	60.6%
AC_{max} (stationary Sphere)	-6.3%	5.0%	5.6%
AC_{mean} (Sphere 33mm)	8.2%	2.2%	5.2%
AC_{mean} (Sphere 22mm)	50.8%	41.8%	46.3%
AC_{mean} (stationary Sphere)	1.0%	-3.0%	2.0%
CR (Sphere 33mm)	33.3%	42.5%	37.9%
CR (Sphere 22mm)	101.9%	133.3%	117.6%
CR (stationary Sphere)	5.0%	5.0%	5.0%

Line profiles across the three spheres in all images (gated and ungated) are shown in Figure 2.7 (g) and (h). The true ^{18}F-FDG concentration was also drawn as a thin black line according to the CT anatomic information. The comparison between the PET and CT line profiles confirms that the two moving spheres match with their respective CT anatomic locations in the gated PET image but not in the ungated images. These line profiles indicate that the two moving spheres have higher CR in the gated 3 min image when compared to the two ungated images. The stationary sphere has similar results in all three images. Quantitative results in Table 2.2(B) show that the gated 3 min image has an average 37.9% and 117.6% improvement in CR for the 33 mm and 22 mm moving sphere respectively when compared to the two ungated images.

2.3.2 Results from the Patient Studies

The maximum and mean SUV, lesion SNR and volume for all the 21 tumors are summarized in Table 2.3 for both amplitude gated and ungated images. The percentage differences (%diff) of the SUV, lesion SNR and volume between the gated and ungated images are also calculated. This table shows that the maximum & mean SUV, and lesion SNR are improved in the amplitude gated images versus the ungated images. The average improvement for the maximum SUV (range 17-62%), mean SUV (range 13-77%) and lesion SNR (range -3.4-81%) is 26.8%, 28% and 26.3% respectively. The improvement in lesion SNR is primarily due to the improvement of the mean SUV of the tumor. The T-test shows that the improvement in SUV and lesion SNR are statistically significant ($p<0.05$) in the gated versus the ungated images. The lesion volumes, as shown in Table

2.3, also decreased by 37.1% on average as a result of reducing the motion blurring using the proposed amplitude gating technique. The T-test also shows that the decrease in tumor volume in the gated image is statistically significant ($p<0.05$) compared to the ungated images.

The results from two lung cancer patients are shown in Figure 2.8(A) and (B) respectively. The tumors on the ungated and the amplitude gated PET/CT fused images are indicated (arrows). The first patient has a non-small cell lung cancer (NSCLC) lesion in the lower left lobe and a big mass in the right lobe. The comparison between the ungated and gated images clearly shows that the mismatch problem between the CT and PET due to the respiratory motion has been resolved in the amplitude gated image. This result confirms that the gated PET image was acquired during the same respiratory amplitude captured in the CT scan. The maximum and mean SUV of the NSCLC lesion improved by 29.5% and 27.0% respectively after using the proposed amplitude gating technique. The second patient has a collapsed lung with two NSCLC tumors close to each other in the right middle lobe. The images in Figure 2.8(B) clearly show that the two tumors in the ungated PET images do not match their corresponding positions on the CT image (arrows) while in the gated images, the PET and CT information match well with one another. The maximum SUV for the two NSCLC lesions improved by 16.6% and 21.4% respectively. Line profiles across the three NSCLC tumors for the two patients are shown in Figure 2.8(C)-(E) respectively. The CT anatomic structures of the three tumors are superimposed on these line profiles for comparison. These line profiles support our conclusion that the PET and CT images match well with one another when the proposed amplitude gating approach is applied.

TABLE 2.3

Summary of SUV_{max}, SUV_{mean}, SNR and CR for All Tumors in the Patient Studies

Lesion No.	Patient ID	SUV_{max} ungated	SUV_{max} gated	% diff SUV_{max}	SUV_{mean} ungated	SUV_{mean} gated	% diff SUV_{mean}	SNR ungated	SNR gated	% diff SNR	Lesion volume ungated (cc)	Lesion volume gated (cc)	% diff volume
1	1	6.78	8.52	25.7%	4.22	5.30	25.6%	102.9	171.0	66.1%	2.15	1.47	31.6%
2	1	3.39	3.95	16.5%	1.71	2.34	36.8%	41.7	75.5	81.0%	5.67	1.37	75.8%
3	2	11.86	13.96	17.7%	7.84	9.26	18.1%	137.0	132.3	-3.4%	1.37	1.27	7.3%
4	2	6.32	10.26	62.3%	3.85	6.85	77.9%	67.3	97.9	45.5%	1.47	0.59	59.9%
5	3	8.71	10.58	21.5%	5.34	6.53	22.3%	84.9	87.2	2.7%	11.54	8.02	30.5%
6	4	13.44	16.06	19.5%	8.43	9.91	17.6%	89.5	109.9	22.8%	11.25	9.19	18.3%
7	5	4.53	5.28	16.6%	2.67	3.19	19.5%	33.2	33.8	1.6%	1.66	1.07	35.5%
8	5	5.37	6.52	21.4%	3.39	4.45	31.3%	42.2	47.1	11.7%	2.94	1.85	37.1%
9	6	3.12	4.04	29.5%	2.00	2.54	27.0%	35.9	44.5	23.7%	10.86	4.59	57.7%
10	7	12.32	15.28	24.0%	6.89	8.24	19.6%	91.5	125.7	37.4%	10.17	6.65	34.6%
11	8	3.78	4.73	25.0%	2.02	2.52	24.7%	28.1	34.1	21.4%	20.1	12.3	38.8%
12	9	3.01	4.09	36.0%	1.62	2.06	26.9%	17.6	18.9	7.5%	22.0	7.9	64.1%
13	9	2.59	3.38	30.6%	1.39	1.72	24.1%	15.1	15.8	4.6%	59.2	26.8	54.7%
14	10	17.89	25.41	42.1%	11.26	15.99	41.9%	178.2	243.4	36.6%	1.47	1.37	6.8%
15	10	17.05	20.04	17.5%	9.88	13.17	33.3%	156.3	200.5	28.2%	1.47	1.17	20.4%
16	10	3.48	4.43	27.3%	1.89	2.23	18.2%	29.9	33.9	13.5%	21.70	13.5	37.8%
17	11	14.17	17.86	26.0%	7.79	10.32	32.5%	89.1	120.7	35.4%	6.94	4.11	40.8%
18	12	7.07	8.56	21.1%	3.91	4.80	22.7%	92.4	128.9	39.5%	1.56	1.17	25.0%
19	12	5.41	6.46	19.3%	3.13	3.53	12.9%	73.9	94.8	28.2%	2.54	2.05	19.3%
20	13	11.74	14.60	24.4%	7.38	8.58	16.2%	93.8	105.7	12.7%	6.94	5.18	25.4%
21	13	2.84	3.96	39.4%	1.50	2.09	39.1%	19.1	25.7	35.0%	18.5	7.73	58.2%
Average		--	--	26.8%	--	--	28.0%	--	--	26.3%	--	--	37.1%

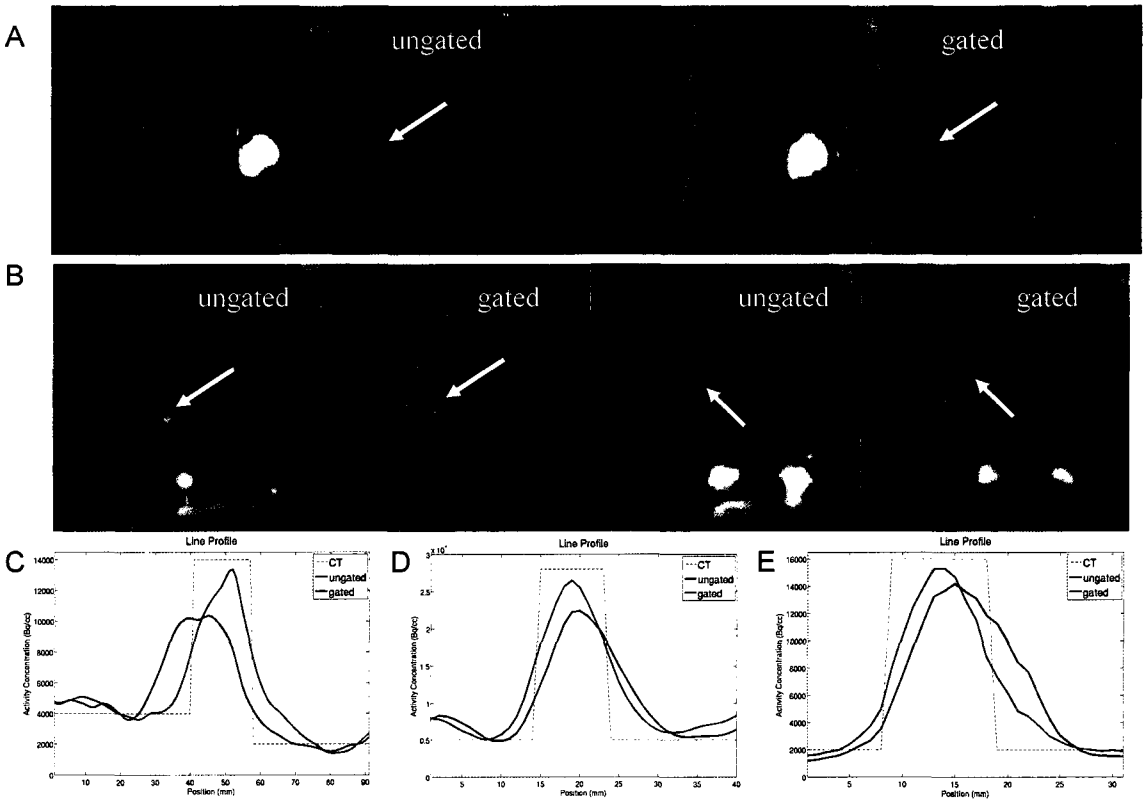

Figure 2.8: Results from two lung cancer patients are shown in (A) and (B) respectively. The tumors in the ungated and gated images are indicated (arrow). The line profiles across the three tumors are shown in (C)-(E) respectively.

2.4 Discussion

In this project, we described a procedure to automate an amplitude gating approach that can be applied in whole-body PET/CT imaging. This approach enables the automatic matching of the respiratory amplitude captured during the CT and PET scans without requiring the patients to hold their breath or maintain any specific breathing pattern. Furthermore, this amplitude gating technique retains the same advantages of DIBH with no additional X-ray exposure nor deformable image registration. In order to

test the performance of this approach, a phantom study and 13 patient studies were analyzed. The results from these studies showed that tumors/spheres on the amplitude-gated images matched well with their locations on the CT images and exhibited higher maximum and mean SUV when compared to the ungated images. Therefore, this new implementation of respiratory amplitude gating is feasible in clinical conditions and has the capability of reducing respiratory motion artifacts in PET images.

One of the objectives of this project is to automate the proposed amplitude gating approach with minimal user interactions. In our suggested approach, the acquisitions of the regular PET scan and the whole-body CT scan are already automated since they follow the same setup as a standard PET/CT protocol in current PET/CT scanners. The remaining processes that need to be automated are the determination of the lesion motion amplitude during the CT scan and the selection of a corresponding amplitude range during the list-mode PET acquisition. Both of these tasks have been automated using an in-house software program while only requiring the technologists to identify (using the mouse) the tumor location in the CT image. The output of this software program is then manually entered into the Anzai device to subsequently inject triggers into the PET list stream. The list-mode PET data acquisition is then manually initiated and is also manually terminated when either 3 minutes worth of PET list-mode data is accumulated in the selected amplitude range or a maximum of 10 minutes of scan duration is reached. The manual termination can be further automated if the manufacturer allows injecting a trigger from the gating device (Anzai system) to stop the acquisition and terminate the scan. In this regard, the whole process of our amplitude gating implementation can be fully automated except for the manual delineation of the physical tumor location, manual

entry of the amplitude range in the Anzai gating system, and the manual initiation and termination of the list-mode PET scan.

To capture the same respiratory amplitude during the CT and list-mode PET scans, the Anzai device was coupled to a data-acquisition device in order to send triggers into the PET list stream at both the beginning and ending stages of the selected amplitude range in each breathing cycle. The primary reason for the use of an additional device is due to the inability of the Anzai device to send these two separate triggers while simultaneously recording the accumulated time within the gate. As far as we know, other respiratory gating devices such as Real-time Positioning Management (RPM) system also can not achieve this objective without being interfaced to other signal processing devices. The primary reason for using the Anzai device rather than the RPM system in this paper is mainly due to the ability of the former to simultaneously monitor the total accumulated time within the gate while tracking the patient's breathing waveform. The PRM device however, does not have the ability to monitor the accumulated time within the gate which is a requirement for the implementation of the proposed amplitude gating approach.

The respiratory amplitude captured during the whole-body CT scan is determined by correlating the axial slice corresponding to the center of the tumor to the recorded patient's breathing waveform. The identification of the tumor central slice on the CT image however is relatively more difficult when the tumor is large (e.g. several centimeters) and therefore may result in inaccuracy in the selection of the position of the amplitude range for the list-mode PET scan. However, since the bed travel is relatively fast during the CT scan (11 cm/sec), a ±1 slice inaccuracy in the determination of the center of the tumor will result in less than 0.05 second inaccuracy in bed travel time.

Compared to the average period of the patient's breathing cycles (5 seconds), this inaccuracy can only result in less than 2% error when selecting the amplitude range for the list-mode PET scan and therefore does not greatly affect the accuracy of the proposed amplitude gating approach.

In the proposed amplitude gating approach, a ±10% amplitude range corresponding to the captured respiratory amplitude during CT was selected for the list-mode PET scan. This amplitude range results in a residual motion of up to 4 mm in the final PET image if the tumor has a motion amplitude of 2 cm. A narrower range such as ±5% would reduce this residual motion to 2 mm but at the cost of increased scan duration in order to accumulate a sufficient count density within the selected gate in the list-mode PET scan. Our phantom study which was based on a 2 cm motion amplitude, showed that the spheres on the gated image matched well with the CT anatomic information suggesting that the small residual motion did not result in an appreciable degradation in the quality and quantification of the gated PET image.

The data acquired from the list-mode PET scan needs to be first filtered before it can be reconstructed to generate an amplitude gated image. This filtering process is performed using a list-resorting program followed by the data-rebinning process of the PET/CT scanner. One might argue that this process can be completed using a one-step approach whereby the data acquired outside the amplitude range can be directly removed from the list-mode data and only events that fall within the specified amplitude range are left. This suggestion however affects the total count rate which eventually results in different random, scatter and dead time correction and affects SUV in the reconstructed PET image which can eventually lead to inaccurate diagnosis.

In our proposed amplitude gating approach, a retrospective resorting of the acquired data is required before it can be reconstructed. To minimize this post-processing task of the data, we suggest that the manufacturer of the scanner directly store data acquired within and outside the gate in two different memory locations similar to phase binning where data in different phases are stored in different bins. In this case, the gated PET data can then be directly reconstructed (prospectively) to generate an amplitude gated PET image thereby further shortening the implementation of amplitude gating on PET/CT scanners.

In our approach, the regular PET scan (step 1) is designed to skip one bed position over the area of interest (lesion location). This skipping step is realized by setting the scan duration of the bed position over the area of interest to the minimum allowable time (one second) since current PET/CT scanners can not be configured to skip over any bed position during a whole-body PET scan. Other approaches to realize the skipping step are possible such as acquiring two different PET scans over the patient's upper and lower body respectively separated by a gap representing the skipped bed position. The most optimal method however would be to require the manufacturer to allow the skipping of any bed position as determined from the scout scan.

Another hurdle with the bed skipping step is that it requires an a-priori knowledge about the rough location of the tumor of interest. This information can be derived from either previous PET/CT scans or from other diagnostic images of the patient. For first-time patients however, it is difficult to identify the location of the lesion of interest in advance. One method to solve this problem is to skip over the patient's whole torso during the regular PET scan (2-3 bed positions using one second per bed) since this

region is the area most affected by respiratory motion. A whole-body CT is then acquired followed by a list-mode PET acquisition over the entire torso. This method however is characterized by relatively longer scan duration since it requires additional bed positions for the list-mode PET scan. Another method to determine the tumor location for first-time patients is not to skip any bed positions but rather acquire a whole-body regular PET scan using 3 minutes per bed position. The center of the tumor can then be determined from either the regular whole-body PET image or the CT image and is then used to determine the motion amplitude that will be used during the list-mode PET scan. This method, however, increases the total scan duration by 3 minutes due to the extra bed position during the regular PET scan that would have otherwise been skipped.

One disadvantage of our proposed approach is the relatively long scan duration of the list-mode PET scan and shorter time accumulated in the selected amplitude range. The long scan duration is due to the fact that only a small portion of the acquired PET data falls within the preset amplitude range. In order to reduce the total scan duration, the list-mode PET scan was designed to be stopped when either 3 minutes worth of data are accumulated or a maximum of 10 minutes of scan duration is reached. In this case, the overall scan duration increases by only 7 minutes. Our patient studies showed that the additional scan duration for our proposed amplitude gating approach was on average 5.3 minutes (range 1.3-7.0 minutes) and therefore did not greatly impact the standard PET/CT imaging protocol. Furthermore, the limitation of 10-min overall scan duration during the list-mode PET acquisition could also result in a shorter time accumulated in gate especially when a transient amplitude (e.g. mid-inspiration) is captured during the CT scan. Our patient studies however have shown that the average accumulated time was

2.6 minutes with a range of 1.8-3 minutes suggesting that on average about 3 minutes within gate could be achieved if the total scan duration was 10 minutes. Approaches to increase the time accumulated in gate during the list-mode PET scan to make it exactly 3 minutes include further increasing the scan duration of the list-mode PET acquisition or acquire data during the patient's end-expiration which is characterized by higher duration ratio in the respiratory cycles. This second approach however will require the patients to hold their breath at end-expiration during the CT scan in order to capture the same motion amplitude during the PET scan. Such an approach on the other hand will require patient compliance and technologist-patient interaction which will have the same problems as the DIBH technique as well as capture the lungs in a collapsed state that might affect the detectability of small lesions.

2.5 Conclusion

In this project, we described the methodology, hardware and software needed to implement and automate the proposed respiratory amplitude gating technique with minimal user interactions on whole-body PET/CT scanners. In this approach, the motion amplitude captured during the CT scan is automatically matched with a corresponding amplitude during the PET data acquisition. The results from the phantom and patient studies show that this approach can be successfully implemented on current PET/CT scanners and has the ability to suppress respiratory motion artifacts.

Chapter 3

Design and Performance of a Respiratory Amplitude Gating Device for PET/CT Imaging

Objective Respiratory amplitude gating techniques have recently been implemented and automated in PET/CT scanners. These techniques however, require specialized hardware and software components that are specifically designed to interface with commercial respiratory gating devices in order to generate and send the necessary triggers to facilitate amplitude gating on PET/CT scanners. The objective of this project is to introduce an in-house device that integrates all the necessary hardware and software components as well as tracks a patient's respiratory motion to realize amplitude gating on PET/CT scanners and test its performance using volunteers and phantom studies.

Methods A piezoelectric transducer was coupled to a data-acquisition system to monitor the respiratory waveform. A Labview® program was designed to control the data-acquisition device and inject triggers into the PET list stream whenever the detected respiratory amplitude crossed a predetermined amplitude range. A timer was also programmed to stop the scan when the accumulated time within the selected amplitude range reached a user-set interval. To test the performance of this device, 10 volunteer and a phantom studies were conducted and the results were compared to those of an Anzai respiratory gating system. The volunteer studies focused on testing the ability of our device to generate respiratory waveform similar to those of the Anzai system while the aim of the phantom study was to evaluate its ability to generate the necessary amplitude triggers to suppress respiratory motion artifacts.

Results For all volunteers, the breathing waveforms generated from the two devices and their respective Fourier transforms were similar with an average correlation coefficient of 0.86 & 0.94 respectively. The two waveforms exhibited an average difference of less than 2.5% in their duration distribution in 8 amplitude ranges. In the phantom study, the amplitude-gated images from the two devices showed similar contrast (<3% difference) and activity concentration (AC) (<2% difference) and exhibited similar improvement in contrast (42.8% vs. 46.7%), AC_{max} (14.6% vs. 17.3%) and AC_{mean} (23.1% vs. 25.8%) when compared to the ungated images.

Conclusion Our in-house respiratory gating device has a similar performance to commercially available respiratory gating systems. This device can realize the proposed amplitude gating scheme without the facilitation of other devices and therefore has an added advantage of low cost.

3.1 Introduction

Respiratory gating techniques have recently been proposed in PET/CT imaging to suppress motion artifacts [58-62]. These techniques can be divided into two categories: phase gating and amplitude gating [29]. In phase gating, the respiratory cycle is divided into multiple phase ranges (or bins) and the acquired data is sorted into each bin based on its acquisition time within the respiratory cycle. This gating approach works well for patients with regular breathing cycles but results in strong artifacts with patients that have irregular respiration. As an alternative approach, amplitude gating has been proposed to divide the total respiration amplitude into different amplitude ranges (or gate) rather than

phase ranges. It has been shown that amplitude gating techniques are better at suppressing respiratory motion artifacts when compared to phase gating [29].

Current PET/CT scanners are only capable of phase gating. The use of amplitude gating in PET/CT scanners is still being developed by many research groups [64-67]. Some of these developments rely on a 4-D PET/CT acquisition where the PET and CT data are acquired in multiple amplitude ranges respectively. PET Images reconstructed from the multiple bins, following attenuation-correction by the corresponding CT images, are then registered and summed together to generate a motion-free image [64, 65]. Other methods, referred to as the motion-incorporated reconstruction techniques, are focused on incorporating the motion information among the different gates of the 4-D PET images into the statistical reconstruction algorithm to reduce motion artifacts [66, 67]. Both of these amplitude-gating approaches, however, are characterized by relatively high patient X-ray exposure due to their requirement of an additional 4-D CT acquisition as well as difficulties in registering the 4-D PET images due to their low statistical count density and high noise content. To overcome these drawbacks, deep-inspiration breath-hold (DIBH) techniques have been proposed as a variant of amplitude gating [37-39]. In this approach, patients are requested to repeatedly hold their breath at deep inspiration (only one amplitude range) for a certain period during the PET data acquisition in order to match the motion amplitude captured in the CT scan. DIBH techniques do not require an additional 4-D CT acquisition but suffer from patient non-compliance particularly when the patient is at an increased state of anxiety due to their medical condition as well as hearing and language barriers. Furthermore, recent studies have shown that approximately 60% of the lung cancer patients can not perform the DIBH technique

successfully [40]. Recently, we proposed a novel approach to implement and automate amplitude gating on current whole-body PET/CT scanners that neither suffered from high patient X-ray exposure nor patient non-compliance [70]. This approach is similar to DIBH techniques except that patients are allowed to breathe freely during the entire data acquisition process while the respiratory amplitude that is captured during the CT scan is automatically matched with a corresponding amplitude range during a list-mode PET scan.

To implement the proposed amplitude gating approach, several criteria had to be satisfied: (1) a respiratory monitoring device had to record the patient's breathing waveform, (2) triggers had to be sent to the PET list stream at the beginning and ending stages of the amplitude range corresponding to the amplitude captured during CT in each breathing cycle, and (3) a timer had to be designed to record the total accumulated time in the selected amplitude range in order to stop the scan when a predetermined accumulated time is reached. Currently there are no commercial respiratory gating systems that can accomplish all of these requirements. In this regard, the implementation of the proposed amplitude gating technique had to rely on a multitude of hardware and software components that were designed and interfaced to one another. In that implementation, an Anzai respiratory gating system (Anzai Medical Co. Ltd., Japan) running in amplitude gating mode was used to satisfy the requirement of recording the patient's breathing cycle as well as tracking the accumulated time within the selected amplitude range. Furthermore, a data acquisition and processing system along with a specialized software were designed to generate the necessary triggers and insert them into the PET list stream.

In this project, we describe an in-house respiratory gating device that has the ability to integrate all of these components into one system thereby facilitating the implementation of our proposed amplitude gating approach. The objective of this project is to introduce this device and test its performance by comparing it to the piecewise Anzai system using volunteers and phantom studies. The proposed respiratory gating device and the setup of the volunteer and phantom studies will be described in section 3.2 and the results of these studies will be presented in section 3.3. Further considerations regarding this in-house device are discussed in section 3.4. Section 3.5 concludes this project.

3.2 Materials and Methods

3.2.1 Equipments

3.2.1.1 In-house Respiratory Gating Device

An MLT-1132 respiratory belt transducer (AD Instruments Inc., Colorado Springs, CO) was used to detect the patient's respiratory signal (Figure 3.1(a)). This respiratory belt transducer consists of a piezoelectric element that transforms pressure into an electric signal. It measures the changes in thoracic or abdominal circumference during respiration which is used to derive real-time breathing phases and amplitudes when attached to the patient's torso. The transducer is a solid-state device that requires no excitation, and has a measurement sensitivity of 5 milivolts/mm. The output voltage of the transducer ranges from 20 milivolts to 400 milivolts. The MLT-1132 connects directly to a BNC (Bayonet

Neill Concelmana connector) input on any signal processing device. The detailed description of this belt transducer can be found elsewhere [71].

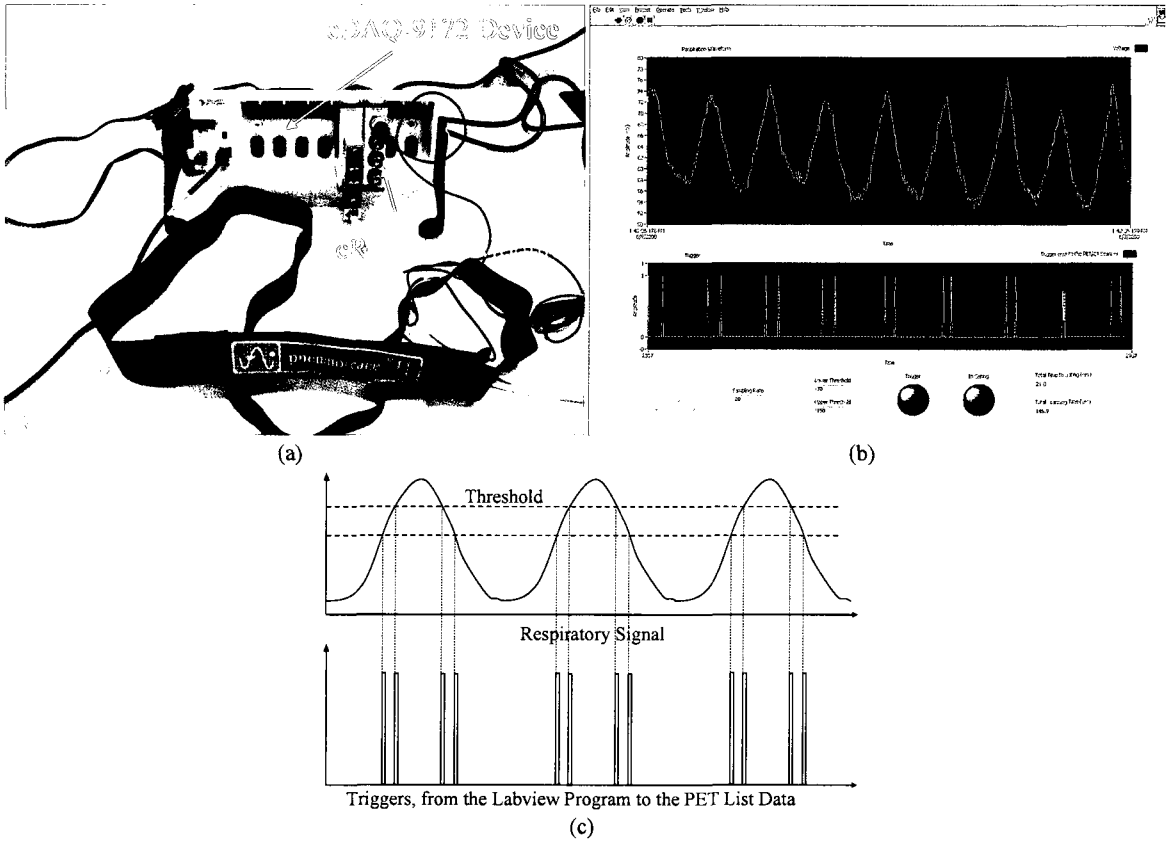

Figure 3.1: (a) The MLT-1132 piezoelectric transducer along with the NI cDAQ-9172 data-acquisition device and cRIO-9215 module, (b) the controlling and data manipulation software designed using Labview®, (c) the relationship between the respiration signal and triggers from the Labview® program.

A NI-cDAQ-9172 data-acquisition device (National Instruments Corp., Austin, TX) was used to detect the respiratory waveform generated from the MLT-1132 transducer through a CompactRIO™ cRIO-9215 module using a BNC connection (Figure 3.1(a)). The cRIO-9215 module has the capability to digitize the analog respiratory signal from the belt transducer and can measure a maximum voltage

difference of up to 10 volts. The detailed descriptions of the cDAQ-9172 device and cRIO-9215 module are available online [72, 73]. A graphical user interface (GUI) software tool (Figure 3.1(b)) was designed using Labview® (National Instruments Corp., Austin, TX) to manipulate and display the detected respiratory signal as well as to store the real-time respiratory signal into a file. Labview® is a development environment for a graphical programming language (G programming) that is usually used to create GUI software for hardware control and real-time signal display purposes. In order to enable the proposed device to acquire PET data in amplitude gating mode, the GUI software was also designed to inject a 5-volt TTL trigger into the PET list stream whenever the measured respiratory amplitude crossed the edges of a user-set amplitude range. The relationship between the respiratory signal detected from the belt transducer and the triggers generated by the Labview® software is shown in Figure 3.1(c). The occurrence of each trigger was also recorded in the saved file, which resulted in an automatic synchronization between the PET list stream and the recorded respiratory signal. A digital timer was also programmed in the Labview® software to stop the acquisition whenever the accumulated scan duration, within the gated amplitude range, reached a user-set interval. The lower and upper thresholds of the gated amplitude range as well as the sampling rate of the device can all be adjusted manually in the front panel of the software. The total scan duration and the accumulated time within the preset amplitude range are also displayed in the front panel. Using this in-house respiratory gating device, the implementation of our proposed automated amplitude gating approach [70] can be realized directly without using any additional devices.

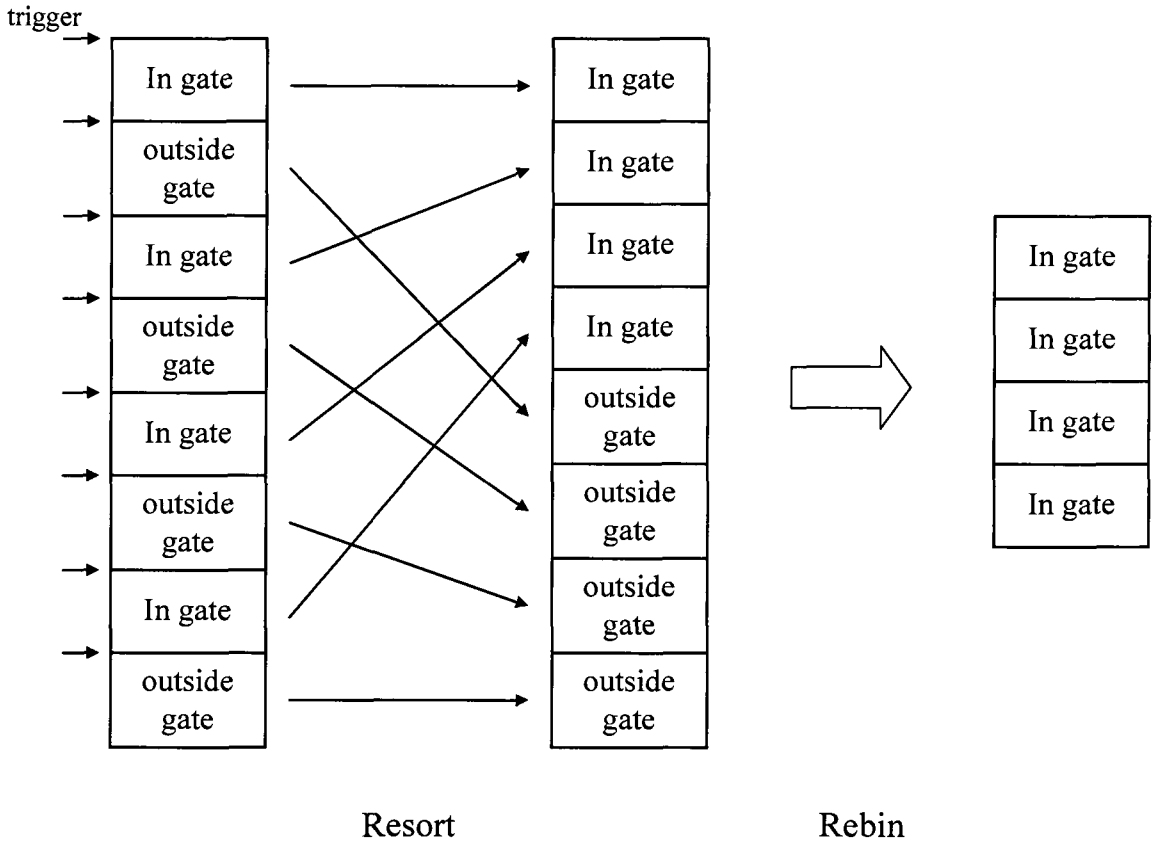

Figure 3.2: The list-resorting and data-rebinning process of the list-mode PET data.

The resultant PET list stream with associated triggers could be post-processed by either rebinning as a static scan or filtering to generate an amplitude gated scan. The filtering process was performed using a list-resorting program followed by the data-rebinning function of the PET/CT scanner, similar to the method we described in the proposed amplitude gating approach [70]. The filtering process is necessary since the rebinning function of the scanner can not be configured to only select events that were acquired within the preset amplitude range. The list-resorting program was written in C and was used to resort the list data in such a way that all events acquired at different breathing cycles but within the preset amplitude range were placed contiguously and in chronological order in front of events that were acquired outside the selected amplitude

range (Figure 3.2). This list-resorting program could also output the total amount of time accumulated within the selected gate which was then used for the data-rebinning process. The resorted list file was then processed by the data-rebinning function of the scanner to extract data that was only acquired within the gated amplitude range. This data was subsequently rebinned as a static scan, attenuation-corrected by the amplitude-matched CT attenuation map and eventually reconstructed to generate an amplitude-gated PET image.

3.2.1.2 Anzai Respiratory Gating System

The Anzai respiratory gating system (AZ-733V; Anzai Medical Co. Ltd.) was used in the volunteers and phantom studies to compare the performance of our in-house respiratory gating device to a commercially available system. The Anzai system consists of a strain gauge sensor secured in an elastic belt that is placed around the patient's torso. The sensor measures the patient's respiratory signal by detecting pressure changes. A sensor port then amplifies and transmits the analog respiratory signal to a wave deck for digitization. The digitized signal is then stored on a personal computer and the Anzai device is configured to output a continuous gate signal whenever the detected respiratory waveform falls within a preset amplitude range. In order to record both the beginning and ending stages of the selected amplitude range in the PET list stream, the NI-cDAQ-9172 data-acquisition device (section 3.2.1.1) is interfaced to the Anzai device to send triggers into the PET list data whenever it detected the rising and falling edges of the gate signal. The detailed description of the coupling between the Anzai device and the data-acquisition device is discussed elsewhere [70]. The resultant trigger-inserted PET list data

can be post-processed using the same method as described in section 3.2.1.1 and reconstructed to generate a motion-free PET image after attenuation correction.

3.2.1.3 PET/CT Scanner

A GE Discovery RX PET/CT scanner (GE Healthcare, Waukesha, Wisconsin, USA) was used for the phantom study in this paper. The PET gantry of this scanner consists of 24 rings of 630 detector crystals per ring and the ring diameter is 88.6 cm. The PET component has a trans-axial FOV of 70 cm and a 15.7 cm axial extent, and can achieve an axial and trans-axial resolution of 4.8 mm and 5.1 mm (measured as full-width half maximum (FWHM)), respectively.

The CT component of this PET/CT scanner is a 64-slice LightSpeed CT with a 50 cm trans-axial FOV and can acquire images with slice thickness ranging between 0.625 and 5.0 mm. The tube current is variable between 10 and 675 mA, and the tube voltage is variable between 80 and 140 KVp, in increments of 20 kVp. All acquired PET data were corrected for attenuation, random, scatter and dead time and reconstructed using OSEM algorithm (2 iterations and 21 subsets).

3.2.2 Performance Tests

3.2.2.1 Volunteer Studies

The objective of the volunteer studies is to investigate whether our in-house respiratory gating device can generate similar respiratory waveforms to the Anzai respiratory gating system.

The breathing cycles of 10 volunteers (6 male, 4 female, age 41±18 years old) were measured simultaneously using both the Anzai respiratory gating system and our in-house device. The Anzai strain gauge sensor was attached to an elastic belt which was placed around the volunteer's torso while the belt transducer of our in-house device was secured right below the Anzai belt. Caution was exercised so that the two belts did not overlap or interfere with one another. All the volunteers were requested to breathe freely while lying down on the patient couch of the PET/CT scanner. For each volunteer study, data acquisition lasted 6 minutes, and the two recorded waveforms were synchronized using a trigger generated from the Anzai system that was recorded by the labview® software of our in-house device. After data acquisition, the two waveforms were then compared to one another by correlating the two waveform shapes. Correlation was also conducted between the respective Fourier transform of the two waveforms to assess the similarity between their frequency responses. In order to investigate the waveform's similarity in motion amplitude distribution, the amplitude of each waveform was then divided into 8 equal amplitude ranges (0-12.5%, 12.5-25%, 25-37.5%, 37.5-50%, 50-62.5%, 62.5-75%, 75-87.5% and 87.5-100%) and the percentage duration distribution (PDD) for each amplitude range was calculated. The PDD was defined as the percent time out of the total scan duration when the respiratory amplitude fell within a specific amplitude range. Eight amplitude ranges were selected because this number has been proposed as the optimal number of gates for amplitude gating in PET/CT imaging [74].

3.2.2.2 Phantom Study

The objective of the phantom study is to test the ability of our in-house respiratory gating device to generate the necessary amplitude triggers to suppress respiratory motion artifacts. This capability was tested by assessing the performance of our system in comparison to the piecewise Anzai device.

The phantom consisted of one stationary (33 mm) and two moving spheres (33 and 22 mm) placed in a water tank. The stationary sphere was fixed to the bottom of the tank, while the two moving spheres were attached to a computer-controlled platform [69]. The platform was driven by a sinusoidal wave and translated the two spheres in the axial direction. The input waveform had a 2 cm peak-to-peak waveform and a period of 5 seconds. The three spheres as well as the tank were filled with ^{18}F-FDG water with a sphere-to-background contrast ratio (SBR) of 5.1:1. The activity concentration in the background was 3.1 kBq/cc. This setup approximated a patient with three tumors, one stationary and two moving under the influence of respiratory motion. The setup of the phantom study is shown in Figure 3.3.

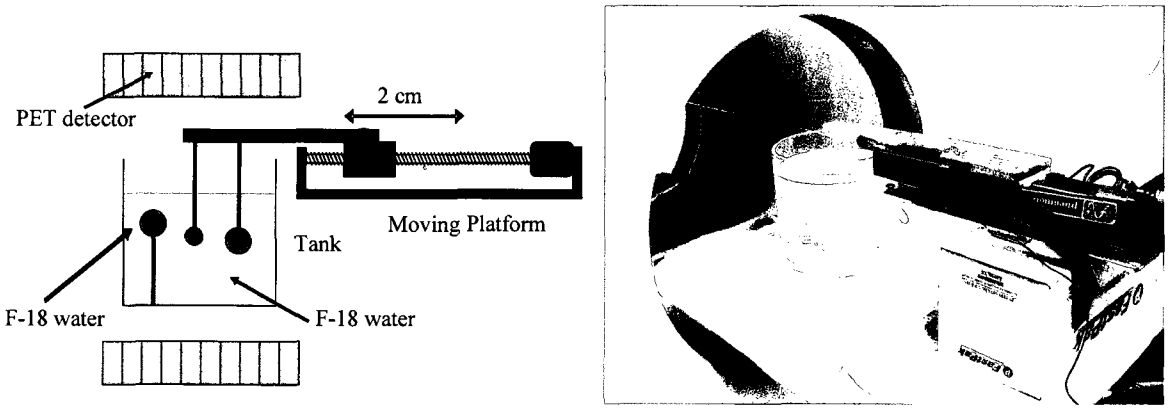

Figure 3.3: The setup of the phantom study.

The phantom was positioned in the central field-of-view of the PET/CT scanner and scanned in 3-D mode. The elastic belts of the Anzai and our in-house sensors were both strapped to the platform while making sure the two devices did not overlap or interfere with one another. List-mode PET/CT with amplitude gating was then acquired. In this case, we chose to acquire the CT data when the moving spheres were stopped at 90% of the maximum motion amplitude. In order to "freeze" the same motion amplitude as captured during the CT scan, a preset amplitude range of 80-100% of the maximum motion amplitude was selected for the list-mode PET scan. In this regard, the Labview® software was configured to send a trigger to the PET list stream whenever the sphere motion crossed the edge of this preset amplitude range. For comparison purposes, the Anzai respiratory gating system (Anzai device coupled to the data-acquisition device) was also configured to record the sphere motion and store the result in a different saved file. Note that the Anzai system was not configured to inject triggers into the PET list stream so as not to confuse these triggers with those of our in-house device. The two recorded respiratory signals were synchronized by a trigger generated from the Anzai system in the beginning of data acquisition. PET data acquisition was stopped when 3 minutes worth of data were accumulated within the preset amplitude range. The 3 minute duration was chosen since it was equivalent to our standard clinical acquisition duration per bed position at our institution. This imaging paradigm resulted in a total acquisition time of 10 minutes of the list-mode PET scan.

The acquired list-mode data was first post-processed and then reconstructed using a 3D-IR algorithm (2 iterations, 21 subsets) to generate the MLT1132-amplitude-gated image. The amplitude-gated image corresponding to the Anzai system, however, was

generated using a "retrospective" gating approach. In this case, the triggers in the original PET List data were first removed and new triggers were inserted based on the gate information derived from the respiratory signal recorded by the Anzai system. This new list-mode data was also post-processed and then reconstructed using the same algorithm to generate an Anzai-amplitude-gated image. For reference purposes, the original list-mode data was rebinned as a static scan (ungated) of 3 and 10 min respectively and reconstructed using the same algorithm. The 10 min ungated image was generated since it consisted of all the acquired data while the 3 min ungated image was reconstructed because this duration is similar to the standard scan duration per bed position used at our institution.

The two amplitude-gated images as well as the two ungated images (3min & 10min) were compared to one another using visual inspection. The CT anatomic information of all the spheres (location and size) was also superimposed on the PET images to evaluate their position with respect to the PET images. Line profiles were also drawn along the two moving spheres as well as the stationary sphere on the four images. Maximum and mean activity concentration (AC) as well as the contrast ratio (CR) were then determined from the line profiles for all spheres. The mean AC was defined as the average pixel value of a region-of-interest (ROI) drawn based on the corresponding CT image. The ROIs for the moving spheres were shifted by 1 cm (half the motion amplitude) along the sphere motion direction in the ungated images versus the gated image to account for the mismatch between the CT image and ungated PET image. The contrast ratio was defined as:

$$CR = (P - T) / P \tag{3.1}$$

where P and T represent the *peak* and *trough (valley)* value across the line profile of the sphere respectively. All ACs and CRs are normalized to the AC and CR of the stationary sphere in the ungated 10 min reference image. The percent improvements in maximum AC, mean AC and CR for the moving spheres on the gated images versus ungated images were also calculated.

3.3 Results

3.3.1 Results from the Volunteer Studies

The respiratory waveforms generated from the Anzai respiratory gating system and our in-house device for one of the volunteers are shown in Figure 3.4(a). The average amplitude of each waveform was subtracted to suppress the DC components (zero frequency). The two waveforms are also normalized to the same scale with each other for display purposes. The similarity between the two waveforms in Figure 3.4(a) suggests that our in-house respiratory gating device has the capability to generate a similar respiratory waveform as the commercially available Anzai respiratory gating system. The Fourier transforms of the respective waveforms are shown in Figure 3.4(b). This figure also indicates that the two results contain similar frequency components.

The correlation coefficients between the two waveforms and their respective Fourier transforms for all the 10 volunteers are summarized in Table 3.1(A). This table shows that the two waveforms have an average correlation coefficient of 0.86 while their respective Fourier transforms have an average correlation coefficient of 0.94. These

quantitative results support our finding that the two amplitude gating devices can generate similar respiratory waveforms. In addition, the PDDs in the eight different amplitude ranges from both respiratory waveforms for all the volunteers are summarized in Table 3.1(B). This table shows that the waveforms from the two gating systems exhibit similar PDD distribution. The average difference in PDD distribution over all the volunteers did not exceed 2.5%.

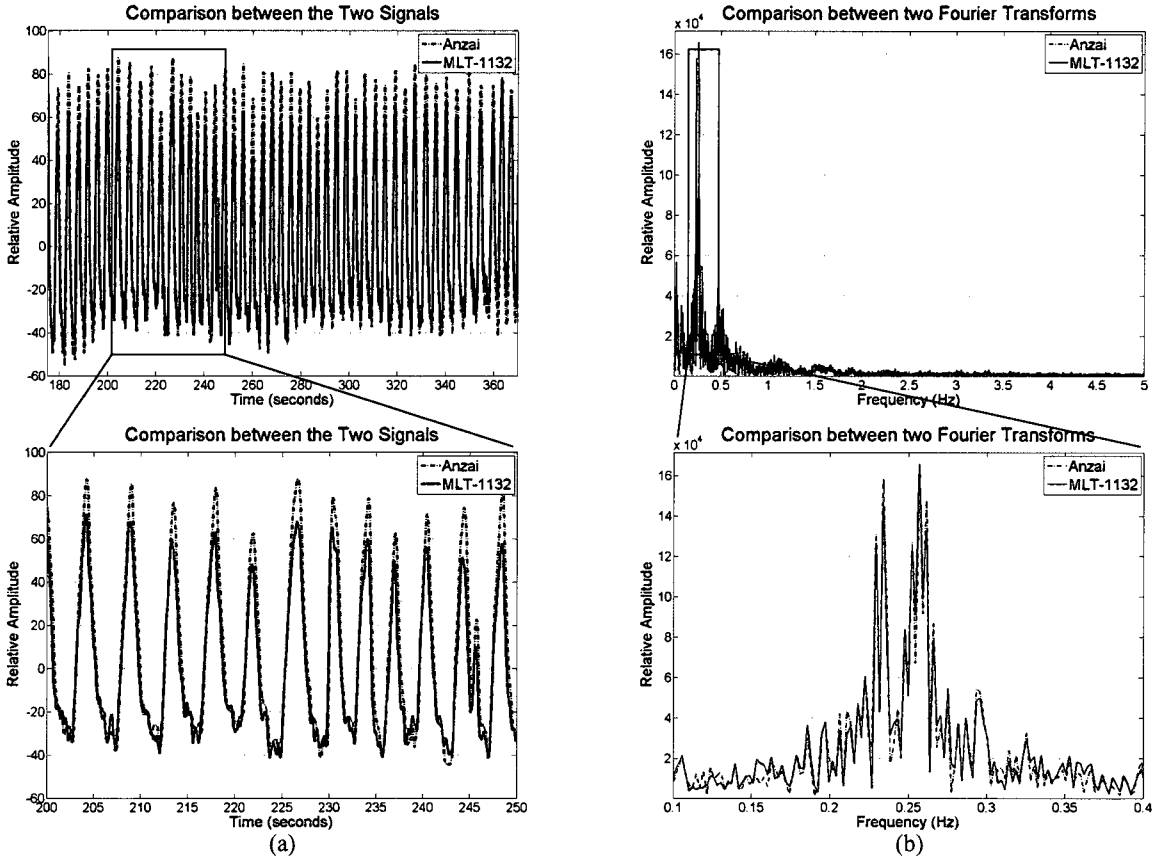

Figure 3.4: Results from the volunteer studies: (a) the respiratory waveform detected from the Anzai respiratory gating system and the in-house device. The Fourier transform of the two waveforms are shown in (b).

Table 3.1: Volunteer Studies

(A) Correlation between the two waveform shapes and their respective Fourier transform

Patient ID		1	2	3	4	5	6	7	8	9	10	Average
Correlation	Waveform shape	0.81	0.95	0.89	0.83	0.80	0.91	0.82	0.94	0.71	0.92	0.86±0.08
	Fourier transform	0.92	0.97	0.96	0.95	0.88	0.95	0.91	0.98	0.95	0.96	0.94±0.03

(B) Percentage Duration Distribution (PDD) in eight amplitude ranges

Patient ID	Percentage Durarion Distribution (PDD) of Each Amplitude Range (Anzai / MLT-1132)							
	0-12.5%	12.5-25%	25-37.5%	37.5-50%	50-62.5%	62.5-75%	75-87.5%	87.5-100%
1	18.7% / 16.2%	22.8% / 20.4%	18.0% / 15.2%	7.1% / 11.3%	6.3% / 8.3%	6.9% / 7.8%	6.8% / 8.7%	13.4% / 12.1%
2	13.9% / 15.3%	34.1% / 31.9%	11.1% / 12.7%	7.9% / 8.9%	7.8% / 7.5%	7.6% / 7.8%	8.7% / 8.9%	9.0% / 6.8%
3	18.9% / 17.1%	27.7% / 24.6%	10.6% / 12.5%	9.2% / 9.8%	8.5% / 10.2%	9.2% / 12.2%	10.9% / 6.7%	4.8% / 6.5%
4	13.9% / 12.7%	21.5% / 20.1%	12.6% / 12.1%	10.8% / 9.9%	11.4% / 9.8%	9.8% / 12.7%	9.9% / 13.1%	9.9% / 9.4%
5	17.1% / 16.9%	20.5% / 19.6%	12.1% / 14.9%	10.1% / 10.6%	10.4% / 9.8%	10.6% / 10.1%	11.2% / 11.0%	7.6% / 6.9%
6	9.2% / 8.3%	18.7% / 15.4%	15.7% / 14.8%	13.8% / 14.8%	12.7% / 11.5%	11.5% / 14.1%	13.1% / 14.1%	5.2% / 6.8%
7	14.4% / 13.5%	21.9% / 21.4%	18.4% / 16.0%	11.5% / 11.7%	8.1% / 7.6%	7.4% / 9.6%	4.1% / 2.4%	13.9% / 17.8%
8	13.1% / 14.7%	38.7% / 33.0%	12.3% / 13.1%	8.8% / 8.8%	7.6% / 8.1%	7.1% / 7.8%	7.5% / 8.3%	4.9% / 6.0%
9	5.2% / 5.4%	37.4% / 36.7%	14.0% / 14.0%	9.3% / 10.0%	8.5% / 8.0%	9.6% / 10.2%	11.0% / 11.9%	5.0% / 3.6%
10	9.2% / 7.6%	36.3% / 31.2%	13.1% / 14.9%	8.1% / 9.3%	8.4% / 9.1%	9.6% / 11.5%	11.0% / 11.5%	4.3% / 4.8%
| Diff. |	1.2%±0.7 %	2.5%±1.8 %	1.6%±1.0 %	1.0%±1.2 %	1.0%±0.6 %	1.6%±1.1 %	1.5%±1.3 %	1.5%±1.0%

Table 3.2: Phantom Study

(A) AC and CR for all images
(Data normalized to the stationary sphere in the ungated 10min reference image)

	Ungated Image 10 min	Ungated Image 3 min	Gated Image Anzai	Gated Image MLT-1132
AC_{max} (Sphere 33mm)	0.97	0.97	1.09	1.05
AC_{max} (Sphere 22mm)	0.76	0.85	0.98	0.97
AC_{max} (stationary Sphere)	1.00 (ref.)	1.05	1.01	1.02
AC_{mean} (Sphere 33mm)	0.83	0.82	0.99	0.98
AC_{mean} (Sphere 22mm)	0.72	0.74	0.96	0.93
AC_{mean} (stationary Sphere)	1.00 (ref.)	1.01	0.98	0.98
CR (Sphere 33mm)	0.73	0.73	0.97	0.95
CR (Sphere 22mm)	0.57	0.63	0.96	0.93
CR (stationary Sphere)	1.00 (ref.)	1.01	1.01	1.01

(B) Percent Improvement of AC and CR in Gated vs. Ungated Image

Improvement (%)	Anzai Gated vs. Ungated 10min	Anzai Gated vs. Ungated 3min	MLT1132 Gated vs. Ungated 10min	MLT1132 Gated vs. Ungated 3min	Average
AC_{max} (Sphere 33mm)	12.4%	12.4%	8.3%	8.3%	10.3%
AC_{max} (Sphere 22mm)	29.0%	15.3%	27.6%	14.1%	21.5%
AC_{max} (stationary Sphere)	1.0%	-3.8%	2.0%	-2.9%	-0.9%
AC_{mean} (Sphere 33mm)	19.3%	20.8%	18.1%	19.5%	19.4%
AC_{mean} (Sphere 22mm)	33.3%	29.8%	29.2%	25.7%	29.5%
AC_{mean} (stationary Sphere)	-2.0%	-2.9%	-2.0%	-2.9	-2.5%
CR (Sphere 33mm)	32.9%	32.9%	30.1%	30.1%	31.5%
CR (Sphere 22mm)	68.4%	52.4%	63.2%	47.6%	57.9%
CR (stationary Sphere)	1.0%	0.0%	1.0%	0.0%	0.5%

3.3.2 Results from the Phantom Study

The respiratory waveforms of the phantom study from the Anzai respiratory gating system and our in-house device are shown in Figure 3.5(a). The average amplitude of each waveform was subtracted to suppress the DC components (zero frequency). The two waveforms are also normalized to the same scale with each other for display purposes. The Fourier transforms of the two waveforms are shown in Figure 3.5(b). Comparisons in Figure 3.5(a)&(b) show that the two waveforms and their respective frequency responses are identical to one another indicating that the two gating systems can generate similar respiratory waveforms. The correlation coefficients between the two waveforms and their respective Fourier transforms are 0.97 and 0.99, respectively.

The two moving spheres in the ungated 10 min, ungated 3 min, Anzai-amplitude-gated and MLT1132-amplitude-gated images are shown in Figure 3.6(a)-(d) respectively. The corresponding images for the stationary sphere are shown in (e)-(h), respectively. Dashed circles are superimposed on these images to represent the locations and sizes of the spheres in the corresponding CT anatomical images. Comparisons between these PET images and the CT anatomic structure indicate that the two moving spheres match well with their locations in the CT image in both of the two amplitude gated PET images (Anzai and MLT1132), while in the ungated PET images (10 min and 3 min), the two spheres appear to extend beyond their positions in the CT image. The stationary sphere, however, matches well with its location in the CT image in all of the four images (gated and ungated) as expected.

From visual inspection, the two gated images exhibit similar contrast and AC while in the two ungated images (3 min and 10 min), the two moving spheres appear

blurred and elongated along their motion direction (axial direction) compared to the two gated images. Furthermore, the stationary spheres in the four images show similar contrast and AC to one another while the background noise in the ungated 10 min image is lower when compared to the other images due to its longer scan duration.

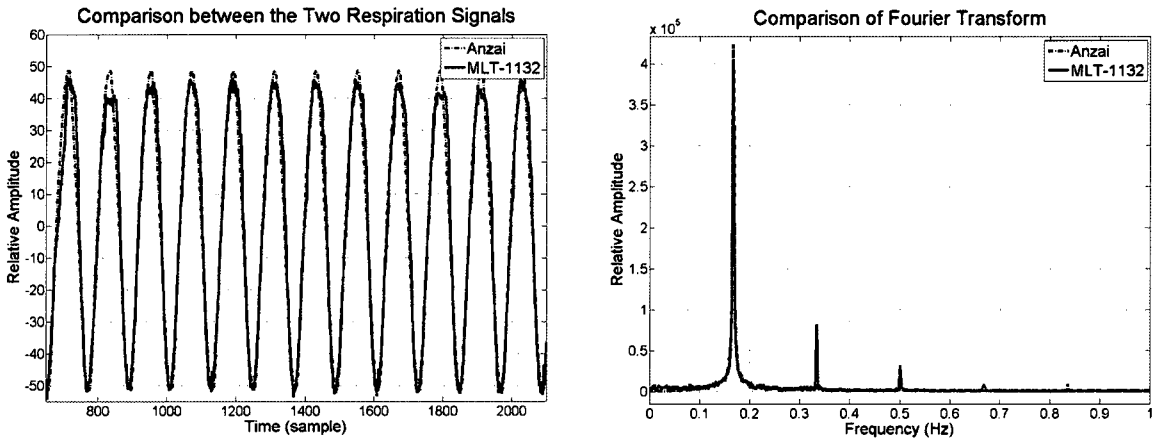

Figure 3.5: Results from the phantom study: (a) Comparison between two respiratory waveforms detected from the Anzai and MLT-1132 transducers, and (b) comparison between the two respective Fourier transforms of the two waveforms.

The maximum and mean ACs of the two moving spheres and the stationary sphere in the four PET images are summarized in Table 3.2(A). Data in this table are normalized to the result of the stationary sphere in the ungated 10 min reference image. Table 3.2(A) clearly shows that the two gated images (Anzai and MLT-1132) exhibit similar AC and have an average difference of 2.0% and 1.3% in max and mean AC, respectively. The improvements of the max and mean ACs in the two amplitude gated image versus both the 10 min and 3 min ungated images are summarized in Table 3.2(B). This table shows that the two gated images exhibit similar improvements in AC_{max} (17.3% vs. 14.6%) and AC_{mean} (25.8% vs. 23.1%) when compared to the two ungated images. For the stationary sphere, the four images have similar mean and max AC as

expected. For the 33 mm moving sphere, the two amplitude gated images have an average improvement of 10.3% and 19.4% in max and mean AC respectively when compared to the two ungated images. These improvements increase to 21.5% and 29.5% for the 22 mm moving sphere. These comparisons indicate that our in-house respiratory gating device has similar ability at recovering AC due to motion blurring as the commercially available Anzai system, especially for small spheres/tumors (22 mm). Table 3.2 also shows that the results from the 33 mm moving sphere and the stationary sphere in the gated image are similar.

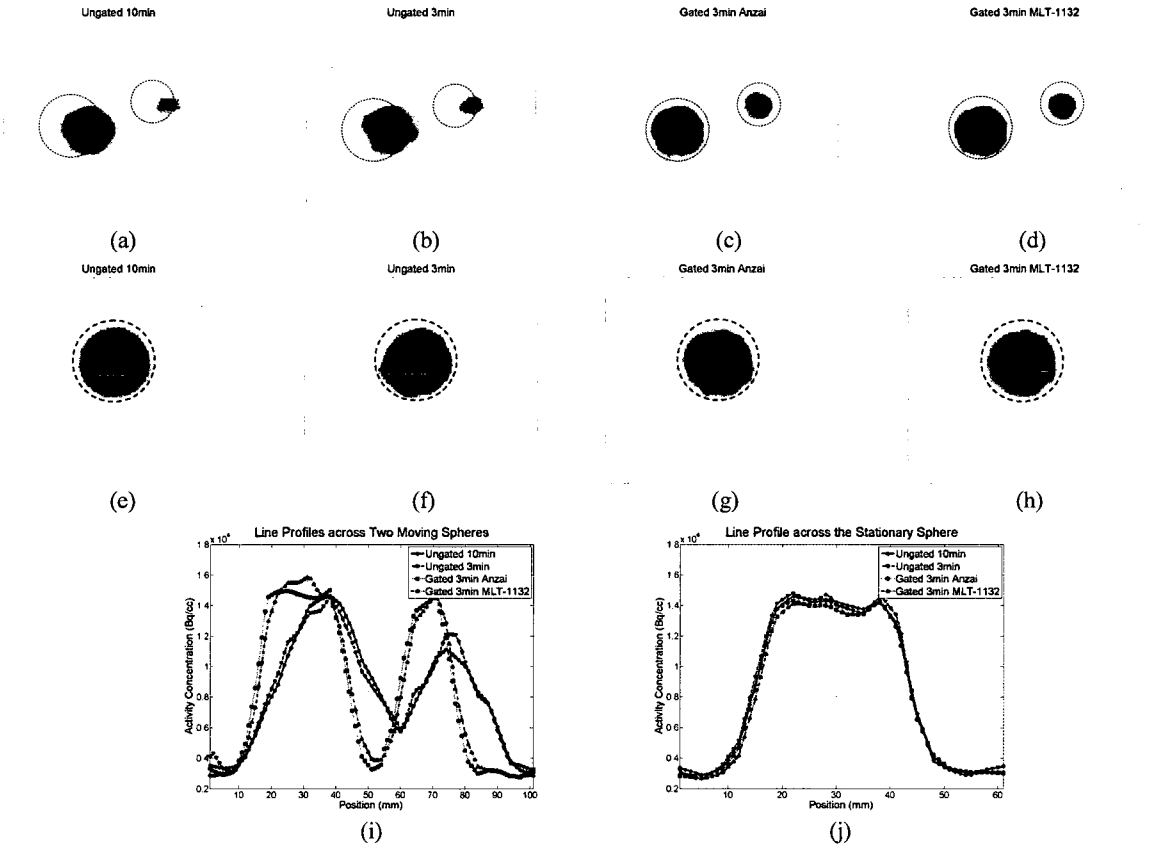

Figure 3.6: Results from the phantom study: The two moving spheres for the (a) ungated 12min, (b) ungated 3min, (c) Anzai-amplitude-gated, and (d) MLT1132-amplitude-gated image. Their corresponding images for the stationary sphere are shown in (e)-(h), respectively. The dashed circles represent the positions of the spheres in the corresponding CT images. The line profiles across the two moving spheres and the stationary sphere are shown in (i) and (j), respectively.

Line profiles across the three spheres in all images (gated and ungated) are shown in Figure 3.6 (i) and (j). These line profiles indicate that the two gated images (Anzai and MLT-1132) have similar max and min AC thereby exhibiting similar CR for the two moving spheres. The line profiles in Figure 3.6(i)&(j) also suggest that the two moving spheres have higher CR in the two gated images when compared to the two ungated images, while the stationary sphere has similar results in all the four images as expected. These results are confirmed by the quantitative comparisons shown in Table 3.2(A)&(B). Table 3.2 shows that the two gated images exhibit an average 1.6% difference in CR between each other while they have an average 31.5% and 57.9% improvement in CR for the 33 mm and 22 mm moving sphere respectively when compared to the two ungated images. These comparisons indicate that the two amplitude gating systems have similar capabilities of improving the CR in PET images.

3.4 Discussion

In this project, we described an in-house respiratory gating device that can be used to implement and automate the respiratory amplitude gating technique in PET/CT imaging that was previously described by our group [70]. This in-house device consists of a commercially available piezoelectric transducer as well as a National Instruments data-acquisition device that are controlled by a Labview® GUI software program. This device has the ability to detect the patient's respiratory waveform and send triggers to the PET list stream at predetermined amplitude settings in each breathing cycle while

simultaneously monitoring the accumulated time within the gate. In this regard, this device has the advantage of integrating a multitude of features that otherwise would have required a commercially available system such as the RPM (Real-time Positioning Management system, Varian, Palo Alto, CA) and Anzai system to be interfaced to a multitude of components to achieve the same objective. We tested the performance of this in-house device by comparing its ability at suppressing respiratory motion artifacts to a piecewise commercially available respiratory gating system (Anzai) that was previously used [70] using both volunteers and phantom studies. The results from these studies showed that our in-house respiratory gating system had similar performance as the Anzai system.

Our in-house respiratory gating system was designed specifically for amplitude gating. The reason for using this gating scheme is primarily due to its proposed benefit over phase gating techniques as has been shown by Dawood et al [29]. However, our Labview® software can also be configured to output triggers into the PET list stream whenever the detected respiratory signal crossed a user-set phase range rather than amplitude range and hence allowing the device to function as a phase gating system. In the phantom study, only one amplitude range was selected to test the performance of this device which is a requirement for our proposed automatic amplitude gating approach[12] as well as the DIBH technique. This device was not designed to generate multiple amplitude triggers as in 4D PET/CT acquisition since such gating methods are not recommended due to their disadvantages of increased X-ray exposure.

One potential advantage of our proposed gating device is its low cost when compared to other commercially available respiratory gating systems such as the Anzai

and RPM systems whose costs range in the tens of thousands of dollars. A breakdown of the total cost of the system includes: (1) $235 for the MLT-1132 piezoelectric transducer from AD Instruments Inc., (2) $1049 for the NI-cDAQ-9172 data-acquisition device from National Instruments Corp., (3) $499 for the CompactRIO™ cRIO-9215 module from National Instruments Corp., and (4) $2599 for the Labview® Full Development environment. The Labview® software is installed in a PC or laptop with the following recommended system requirements: Pentium 4 or above, 1GB memory, 40 GB hard disk, 1024x768 screen and Windows® XP or Vista operating system. The cost of a typical laptop that satisfies these requirements is about $628 (http://www.dell.com), bringing the total price of all the hardware and software components to $5010. This price constitutes less than 10% of the total cost of either the RPM or Anzai systems.

One disadvantage of our in-house respiratory gating device is its relatively higher noise and hence lower SNR in detecting respiratory waveforms when compared to the Anzai system. The high noise from the MLT-1132 transducer can be easily identified from its frequency responses shown in Figure 3.4(b) and 3.5(b). In these figures, the MLT-1132 waveforms always exhibited larger high-frequency components versus the Anzai waveforms. In our volunteer and phantom studies, the MLT-1132 transducer exhibited a noise level of less than 1 milivolt while the amplitudes of the detected respiratory waveforms were usually larger than 20 milivolts. In such cases, a SNR range of 20 to 50 was usually recorded. We believe that this SNR is acceptable for amplitude gating because the noise component constitutes less than 5% of the total detected respiratory signal. However, errors could be perceived to occur whenever the detected respiratory signal falls within the preset amplitude range due to the effects of the noise

while in reality the patient's respiration has not reached that level. Similarly, errors could also exist whenever the detected respiratory signal falls outside the preset amplitude range while in reality the patient's respiration level is still within that range. Such sources of error could potentially lead to additional blurring in the resultant gated PET images and can partly deteriorate the effects of the respiratory gating techniques. To overcome these drawbacks, filters can be designed in the Labview® software to suppress the high-frequency components in the detected waveforms. The addition of such a filter can improve the SNR of the detected respiratory signal but at the cost of a phase delay which, on the other hand, can also introduce similar errors into the gated images. Since the two amplitude gated images (MLT-1132 & Anzai) from the phantom study exhibited similar contrast and AC, we feel that the higher noise content in the MLT-1132 detected respiratory signal is within an acceptable range and does not greatly affect the image quality of the resultant gated images.

3.5 Conclusion

In this project, we described an in-house respiratory gating device that can be used to implement and automate the amplitude gating technique in PET/CT imaging without using any additional specialized devices. This device has the ability to send triggers to the PET list stream at pre-determined amplitude settings while simultaneously monitoring the accumulated time within the gate. The results from the volunteer and phantom studies show that this in-house device has similar performance as the

commercially available Anzai respiratory gating system. This device also has the added advantage of low cost ($5010 for both hardware and software).

Chapter 4

Joint Correction of Respiratory Motion Artifact and Partial Volume Effect in Lung/Thoracic PET/CT Imaging

Objective Respiratory motion artifacts and partial volume effects (PVE) are two degrading factors that affect the accuracy of image quantification in PET/CT imaging. In this paper, we propose a joint correction approach to improve PET quantification by simultaneously correcting for respiratory motion artifacts and PVE in lung/thoracic cancer. The objective of this paper is to describe this approach and evaluate its performance using simulation and phantom studies.

Methods The proposed joint correction approach incorporates a model of motion blurring, PVE and object size/shape. A motion blurring kernel (MBK) is then estimated from the deconvolution of the joint model while the activity concentration (AC) of the tumor is estimated from the normalization of the derived MBK. To evaluate the performance of this approach, a computer simulation and a phantom study were performed while a uniformly-distributed and a sinusoidal motion waveform were used to control the tumor/sphere motion respectively. The resultant MBK was compared to the true MBK by measuring a correlation coefficient between the two kernels. The measured tumor AC derived from the proposed method on the other hand was compared to the true AC as well as the ACs in images exhibiting PVE only, motion blurring only and images exhibiting both PVE and motion blurring.

Results For the simulation and phantom studies, the estimated MBK approximates the true MBK with a correlation coefficient of 0.94 and 0.92 respectively.

In both studies, the tumor ACs following the joint correction technique were similar to the true AC with an average difference of 0.4% and 1.0% respectively. Furthermore, the tumor ACs on the PVE only images, motion blurring only images and images with both effects were on average 70.2% (75%), 54.8% and 49.8% (47.5%) of the true AC respectively for the computer simulation (phantom study) study.

Conclusion The proposed joint correction approach can improve the accuracy of PET quantification by simultaneously compensating for the respiratory motion artifacts and PVE in lung/thoracic PET/CT imaging.

4.1 Introduction

Combined PET/CT imaging plays an important role in the staging and response to therapy of various types of cancers. The use of PET/CT imaging in lung/thoracic cancer, however, is limited by the patient's respiratory motion artifacts [56, 80] and partial volume effects (PVE) [81] both of which result in inaccurate PET image quantification. There are two sources of error that can exist due to respiratory motion artifacts; these are motion blurring effects and mismatch between the PET and CT images. Motion blurring in PET images is primarily caused by object motion during the long scan duration which is necessary in PET imaging, while the mismatch between the PET and CT is primarily due to the discrepancy between the scan durations of the two imaging modalities [54]. PVE, on the other hand, is mainly caused by the finite spatial resolution of PET scanners [82]. Due to this limited resolution, PET images underestimate the radiotracer uptake when the tumor size is less than 2-3 times the scanner's spatial resolution, which is

typically 4-8 mm full width at half maximum (FWHM) on current commercially available scanners.

Several approaches to correct for respiratory motion artifacts in PET/CT imaging have recently been introduced. One such approach, known as 4D PET/CT, acquires PET and CT data in multiple time frames according to the respiratory phase or amplitude captured in each frame [59, 83]. Since each frame captures only a small portion of the whole motion, these 4-D PET/CT images can be regarded as motion-free images. However, a major problem of this approach is that each single frame only contains a small amount of counts and therefore is characterized by low signal-to-noise ratio (SNR). In this regard, various deformable registration techniques have been proposed to register these frames to one another in an effort to generate a motion-free PET image with improved SNR [59, 83]. Another approach that has been proposed to achieve the same objective is to incorporate the motion vectors between the different frames as part of the reconstruction algorithm to generate a final motion-free image [66, 67]. All of these techniques however, suffer from high patient X-ray exposure due to the additional 4-D CT scan as well as inaccuracies in the image registration process due to the low SNR of each PET/CT frame. To overcome these drawbacks, techniques maximizing the acquired data in a single phase/amplitude bin such as repeated breath hold (DIBH) or increasing scan duration in a single bin have recently been proposed and implemented [37-39]. With such techniques, PET/CT data is acquired in a single phase/amplitude while maximizing the duty cycle of this specific gate and therefore results in reduced patient X-ray exposure and no requirement of deformable registration. In all of these approaches however, respiratory monitoring devices are used to acquire the patient's breathing waveform.

Furthermore, signal processing devices may be required in some of these techniques to generate triggers in order to indicate the onset of each frame or gate.

As with motion correction techniques, several methods to compensate for PVE have also been proposed in PET/CT imaging. These methods can be divided into two categories: those applied at the regional level and those applied at the pixel level [82]. The PVE correction methods applied at the regional level do not yield PVE-corrected images but rather PVE-corrected regional values (e.g. max or mean AC) which are suitable for the quantification of tumor uptake but not for visual analysis. In this regard, images with PVE correction techniques that are applied at the regional level should not be used for visual assessment. Examples of the most commonly used methods that utilize this approach are the recovery coefficient [84] and geometric transfer matrix [85] largely due to their relative ease of implementation. Both of these methods strongly rely on the technique used to measure the tumor size and shape and its corresponding accuracy, and therefore require precise delineation of the tumor since different tumor sizes and shapes may result in drastically different correction factors. Other approaches that are used to correct PVE include deconvolution [86], fitting methods [87] and modeling the PVE during reconstruction [44]. These techniques are either applied at the regional or pixel level to correct for the PVE with certain success and limitations. However, none of these approaches can simultaneously correct for PVE as well as respiratory motion artifacts as applied to lung/thoracic cancer.

Recently, a combined motion and PVE correction approach was proposed by Wiemker et al to correct for both the motion blurring and PVE effects in pulmonary nodules [88]. In that paper, both PVE and motion blurring were corrected by delineating

the tumor size and shape from the CT image while a point spread function (PSF) which incorporated both the PET image resolution and motion blurring was estimated and used to generate a corrected AC. Such an approach however, assumes that the motion blurring is a Gaussian function (which is not usually the case) and requires that a manual registration step is performed to maximize the correlation between the PET and CT data. To our knowledge, no other investigation has considered the simultaneous correction of respiratory motion and PVE.

In this project, we propose a novel approach to improve the accuracy of PET image quantification by simultaneously correcting for respiratory motion artifacts and PVE in lung/thoracic tumors. The proposed method does not make any assumptions about the motion blurring function or require any image registration step while at the same time has the ability to jointly correct for PVE and motion blurring. The proposed approach is applied at the regional rather than the pixel level to generate the corrected AC and in this regard is suitable for lesion quantification only and not image visualization. The objective of this paper is to describe how such a joint correction approach is formulated and evaluate its ability to improve the accuracy of PET image quantification using simulation and phantom studies.

4.2 Materials and Methods

4.2.1 The Joint Correction Approach

In this section, we propose a mathematical framework to correct for both the respiratory motion artifacts and PVE in lung/thoracic PET/CT imaging.

In PET/CT imaging, PET images are usually much more blurred when compared to corresponding CT images. This blurring effect, known as PVE, is primarily caused by the finite spatial resolution of the PET scanners, which is not only limited by the detector size/design (PET intrinsic resolution) but also affected by the reconstruction parameters. In this regard, the resultant PET image can be modeled as the convolution between the PSF of the PET system and the true PET image (object) that would be obtained if no PVE existed:

$$I_{obs} = I_{true} \otimes PSF \tag{4.1}$$

where I_{obs} is the observed PET image, I_{true} is the true PET image (object) and $\otimes$ represents the convolution process. The PSF represents the point spread function of the system which includes the effects of both the intrinsic resolution of the PET scanner and the reconstruction algorithm.

Under the effects of respiratory motion, lung/thoracic lesions will look even more blurred along the tumor motion direction. Since the patient's respiratory motion is usually non-rigid, a single motion blurring function is insufficient to represent the motion blurring effect of the whole body since different body parts can have different motions. However, in this study we will assume that the whole lung lesion has a locally rigid motion due to its small size. In this regard, the motion blurring effect for this lung lesion can be modeled as an additional convolution between the PVE-blurred PET image and the motion blurring kernel (MBK) defined in a region-of-interest (ROI) drawn around the tumor:

$$I_{obs} = I_{true} \otimes PSF \otimes MBK \tag{4.2}$$

This equation from here onward is referred to as the overall-blurring equation since it represents the overall blurring effect in lung/thoracic PET imaging (PVE+motion).

For lung/thoracic lesions, the following assumptions are made: (1) The lesion has a homogeneous AC distribution and any non-homogeneity in the observed PET image is due to the effect of PVE and motion blurring, and (2) negligible radiotracer uptake exists in the surrounding background since this area is mainly composed of lung tissue with very low activity. Based on these assumptions, an ideal PET image (I_{true}) of a tumor with uniform activity concentration that is not affected by PVE nor motion blurring can be represented as:

$$I_{true} = AC_{mean} \times IF \tag{4.3}$$

where IF represents the indicator function of the lung lesion which has unit values inside the lesion but zeros outside the tumor. The IF can be derived from the delineation of the tumor in the corresponding CT image. In addition, AC_{mean} represents the mean AC distribution of the lung lesion which is usually not affected as much as the maximum AC. When (4.2) and (4.3) are combined with one another, we have:

$$\begin{aligned} I_{obs} &= (AC_{mean} \times IF) \otimes PSF \otimes MBK \\ &= (IF \otimes PSF) \otimes (AC_{mean} \times MBK) \end{aligned} \tag{4.4}$$

This equation shows that the observed PET image depends on the convolution between two terms. The first term, $IF \otimes PSF$, can be derived from the tumor delineation on the CT image and measuring the PET scanner resolution respectively. The second term ($AC_{mean} \times MBK$), on the other hand, can be calculated by deconvolving the observed PET image by the first term in equation (4.4). In order to suppress the noise amplification

which is a characteristic of the deconvolution operation, we employ an expectation maximization (EM) deconvolution algorithm which is an iterative approach [60]:

$$\text{if} \quad g(x,y) = h(x,y) \otimes f(x,y)$$

$$\text{then} \quad f_{k+1}(x,y) = f_k(x,y) \times \left[h(-x,-y) \otimes \frac{g(x,y)}{h(x,y) \otimes f_k(x,y)} \right] \tag{4.5}$$

where $f_k(x,y)$ is the estimation of $f(x,y)$ during the kth iteration and any multiplication and division are point-by-point within the image. In this paper, 20 iterations were selected during the implementation of this algorithm which has been tested to be sufficient to reach convergence [60]. In the above equation, we had the following substitutes:

$$\begin{aligned} g(x,y) &= I_{obs} \\ h(x,y) &= IF \otimes PSF \\ f(x,y) &= AC_{mean} \times MBK \end{aligned} \tag{4.6}$$

Since the MBK represents the probability of a tumor to appear in a specific location, its integration over the whole space/image/ROI should be equal to unity:

$$\iint MBK(x,y)dxdy = 1 \tag{4.7}$$

In this regard, the mean activity concentration of the tumor AC_{mean} can be derived from the normalization of $f(x,y)$:

$$AC_{mean} = \iint f(x,y)dxdy = \iint (AC_{mean} \times MBK)dxdy \tag{4.8}$$

and the MBK can then be simultaneously calculated from

$$MBK = f(x,y) / AC_{mean} \tag{4.9}$$

In summary, the whole process of the proposed joint correction approach consists of the following steps: (1) delineation of the lung lesion on the CT image to generate an indicator function *IF*, (2) determination of the PET image spatial resolution *PSF*, and (3)

incorporation of *IF* and *PSF* in the overall-blurring equation (4.4) to derive the mean tumor AC and MBK by deconvolution. The by-product of this joint correction approach is the MBK which can be used for other applications such as motion control, motion extent estimation and motion trajectory monitoring. In this project, both a computer simulation and a phantom study will be performed to evaluate the ability of this proposed joint correction approach to improve PET image quantification.

4.2.2 PET Spatial Resolution

A GE Discovery STE PET/CT scanner (GE Healthcare, Waukesha, Wisconsin, USA) was used for the phantom study in this paper. The PET gantry of this scanner consists of 24 rings of 560 detector crystals per ring and the ring diameter is 88.6 cm. The PET component has a trans-axial FOV of 70 cm and a 15.7 cm axial extent.

In order to obtain the spatial resolution of a PET image reconstructed using a specific set of parameters, a point source is usually imaged and its FWHM is measured after image reconstruction using a predetermined reconstruction parameter set. In this paper, however, a more practical and automated approach is employed to measure the PET resolution which utilizes the routinely available uniform cylindrical phantom [89]. This resolution measurement approach enables the derivation of a scanner PSF from deconvolving the PET image from the corresponding CT image in Fourier transform space. The FWHM of the derived PSF is then measured using a Gaussian fit to represent the PET image resolution. This approach has been tested to be robust and accurate [89]. Figure 4.1 shows the results from the cylindrical phantom measurement for the scanner used in this paper. The CT image, PET image and the derived PSF image are shown in

Figure 4.1(A) while the results from the Gaussian fitting are shown in Figure 4.1(B) for both the radial and tangential line profiles through the PSF image. The results were based on the following reconstruction parameters: 3D OSEM (2 iterations, 20 subsets), 256 mm FOV, 256×256 matrix size, 2-mm filtering. These parameters were chosen since our phantom images were generated using these parameters. The two Gaussian fittings indicate that the radial and tangential FWHM of the PSF are 4.5 and 4.7 mm respectively. Therefore, in the phantom study of this paper, a PSF with 4.6 mm FWHM is used to represent the PET spatial resolution.

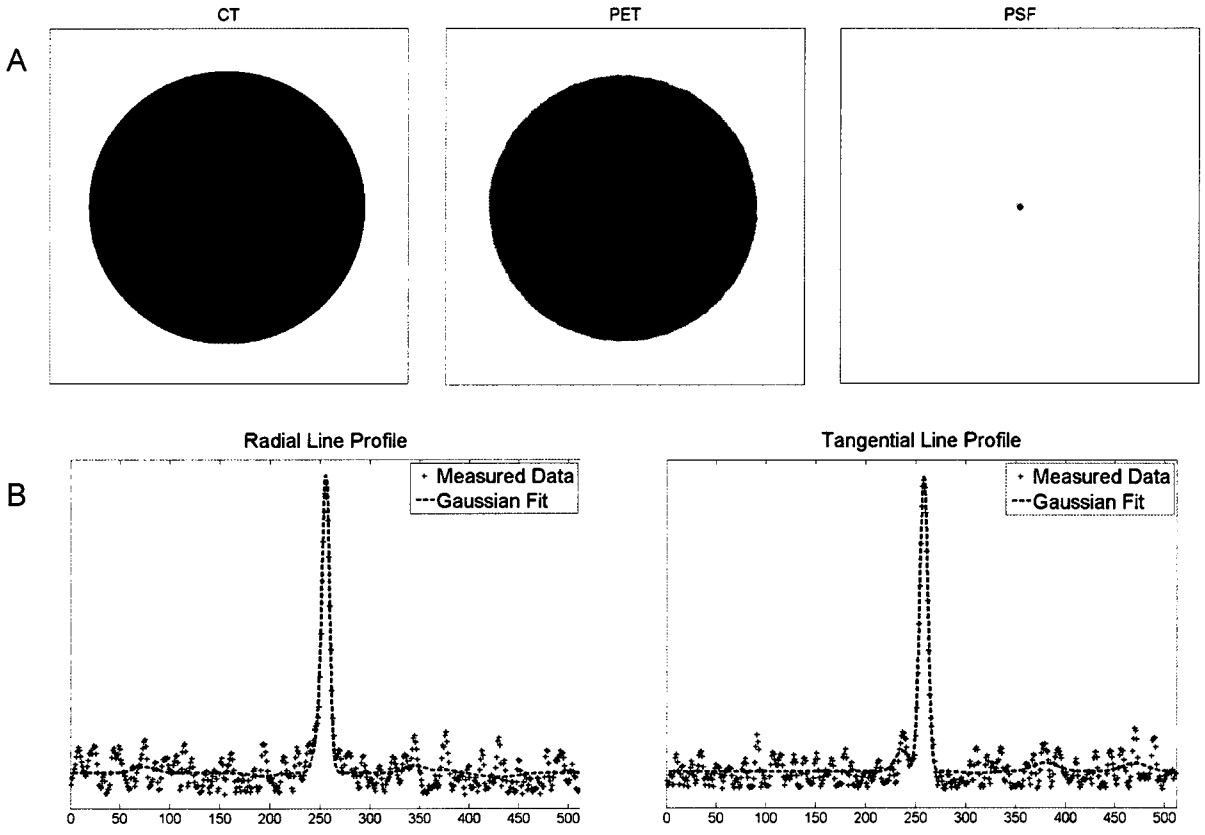

Figure 4.1: Spatial resolution measurement for the PET scanner. (A) The CT image, PET image and the derived point spread function (PSF). (B) The radial and tangential line profiles across the PSF image and the Gaussian fitting.

4.2.3 Computer Simulation

The objective of the computer simulation is to test the performance of the proposed joint correction approach and evaluate its ability to improve the accuracy in PET quantification. All the simulation codes were written in a Matlab® environment using Jeff Fessler's Image Reconstruction Toolbox [90].

A total of 9 combinations of different tumor shapes (square, circle and triangle) and sizes (side/diameter: 30, 20 and 10 mm) were simultaneously simulated in a PET/CT scanner. These tumors were simulated to contain 10 kBq/cm^3 radioactivity concentration. No background radioactivity was simulated in this study. A CT image was first captured when the tumors were stationary while during the PET scan, a 2-cm uniformly distributed motion function was applied in the vertical direction to control the motions of all the simulated tumors. A PSF with 5 mm FWHM Gaussian distribution was applied during the PET acquisition to simulate the finite spatial resolution or PVE of the PET scanner. After data acquisition, the CT and PET images were reconstructed using FBP and OSEM algorithms (2 iterations, 21 subsets) respectively. The reconstruction FOV was selected as 256 mm while a 256×256 and 512×512 matrix size were used for PET and CT reconstructions respectively. The reconstructed PET image was then upsampled to a 512×512 matrix size corresponding to the CT image. For each simulated tumor, a square ROI was drawn around the tumor and an IF was delineated on the corresponding CT image. The derived IF as well as the scanner PSF (5 mm FWHM Gaussian) were then incorporated into equations (4.4) and (4.5) to estimate the PET AC and MBK.

For each simulated tumor (shape and size), the estimated AC obtained using the proposed joint correction approach was compared to the true simulated AC. Furthermore,

the estimated MBK was compared to the true MBK by calculating the correlation coefficient between the two MBKs to represent a measurement of their similarity. For reference purposes, a PET image that had PVE only (no motion was simulated) as well as a PET image that had motion blurring only (no PVE was simulated) were also simulated in this study and reconstructed using the same reconstruction parameters. The average AC for each simulated tumor on these two PET images was also calculated based on a ROI drawn on the CT anatomical image. The same simulation was repeated 50 times and a standard deviation was calculated for each tumor AC on each PET image. An ANOVA test was conducted among the tumor ACs derived from the joint correction approach, PVE only images, motion only images and PET images with both motion blurring and PVE in order to determine whether their differences were statistically significant.

4.2.4 Phantom Study

The objective of the phantom study is to evaluate the performance of the proposed joint correction approach in a controlled pseudo-clinical environment.

The phantom consisted of two moving spheres (33 and 22 mm diameter) which were attached to a computer-controlled platform [69]. The platform was driven by a sinusoidal waveform which translated the two spheres in the left-right direction on the transaxial plane. The input waveform had a 2 cm peak-to-valley amplitude and a period of 5 seconds. The two spheres were filled with ^{18}F-FDG water with an activity concentration of 39.7 kBq/cm^3. This setup approximated two moving lung lesions. The setup of the phantom study is shown in Figure 4.2 with the two spheres placed one after the other along the axial direction (the smaller sphere is hidden behind the bigger sphere).

The phantom was placed in the central FOV of the PET/CT scanner and a CT scan was first captured when the two spheres were stationary. PET data were acquired twice using 3-D mode. During the first scan, the phantom was moving according to the controlled motion waveform while during the second scan no motion waveform was applied. The duration of both scans was set to 3 minutes based on the standard clinical protocols in our institution. The aim of the second PET scan was to generate a PET image without any motion blur (PVE only image) for reference purposes. After data acquisition, the two PET images as well as the CT image were reconstructed using OSEM (2 iterations, 20 subsets, and default filter) and FBP respectively. The matrix size used for PET and CT reconstructions were 256×256 and 512×512 respectively while the PET image was then upsampled to a 512×512 size corresponding to the CT image. All reconstructions were performed using a FOV of 256 mm.

For each sphere, a cubic volume-of-interest (VOI) was drawn around the sphere and an IF was delineated based on the CT image. The sphere segmentation was based on CT numbers of ±8 that represented water which was then further refined by the comparison between the segmented and the true sphere volumes. The derived IF as well as the measured scanner PSF in section 4.2.2 were then incorporated into equations (4.4) and (4.5) to estimate the true PET AC and MBK. For reference, the maximum and mean AC of both spheres on the PET image with PVE only and the PET image with both motion blurring and PVE were also calculated. Furthermore, the derived MBK was compared to the true MBK and a correlation coefficient was determined.

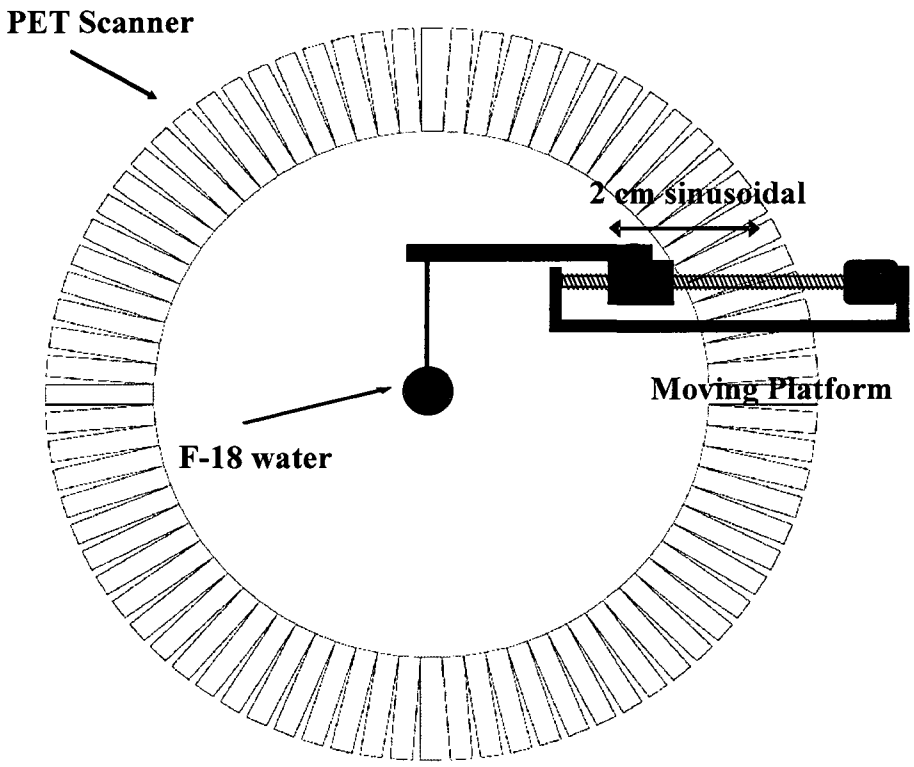

Figure 4.2: The setup of the phantom study.

4.3 Results

4.3.1 Computer Simulation

The CT image and PET image reconstructed from one of the 50 simulations are shown in Figure 4.3(A) and (B) respectively. All the simulated shapes in Figure 4.3(B) exhibit an elongated blurring artifact in the vertical direction due to motion. The MBK estimated from the joint correction approach is displayed in Figure 4.3(C). This MBK indicates that the motion of these tumors is uniformly distributed along the vertical direction and has an amplitude of 2 cm (40 pixels with 0.5 mm/pixel). This result

matches the true motion blurring function applied in this simulation study. The correlation coefficients between the estimated and true MBK for all the tumors in the 50 simulations are summarized in Table 4.1. This table shows that the average correlation coefficient between the two MBK is 0.94±0.004 suggesting that the MBK derived from the proposed joint correction method approximates the true MBK very well.

The PET images with PVE only, motion blurring only and the PET image after joint correction are displayed in Figure 4.3(D)-(F) respectively. These three PET images as well as the reconstructed PET image in Figure 4.3(B) are displayed using the same color scale. One thing to note here is that the PET image after joint correction (Figure 4.3F) is not a real PET image but rather only a binary image (IF) multiplied by the derived ACs (Equation 4.3). Since the proposed joint correction approach is applied at the regional rather than the pixel level, the results produce a corrected AC value rather than an image. We have however opted, to show this corrected value using a visual representation (Figure 4.3F) in addition to the numerical result shown in Table 4.1. The average ACs for all tumors on the four PET images are summarized in Table 4.1. These results indicate that the PET image generated using the joint correction method can recover the tumor AC to an average of 99.6±0.7% of the true AC while the PET images with PVE only and motion blurring only can only recover the tumor AC to 70.2±0.7% and 54.8±0.6% of the true tumor AC respectively. The PET image with both motion blurring and PVE, on the other hand, only exhibits around 49.8±0.5% of the true tumor AC in this simulation. The result from the ANOVA test shows that the AC differences among these four PET images are statistically significant ($p<0.05$).

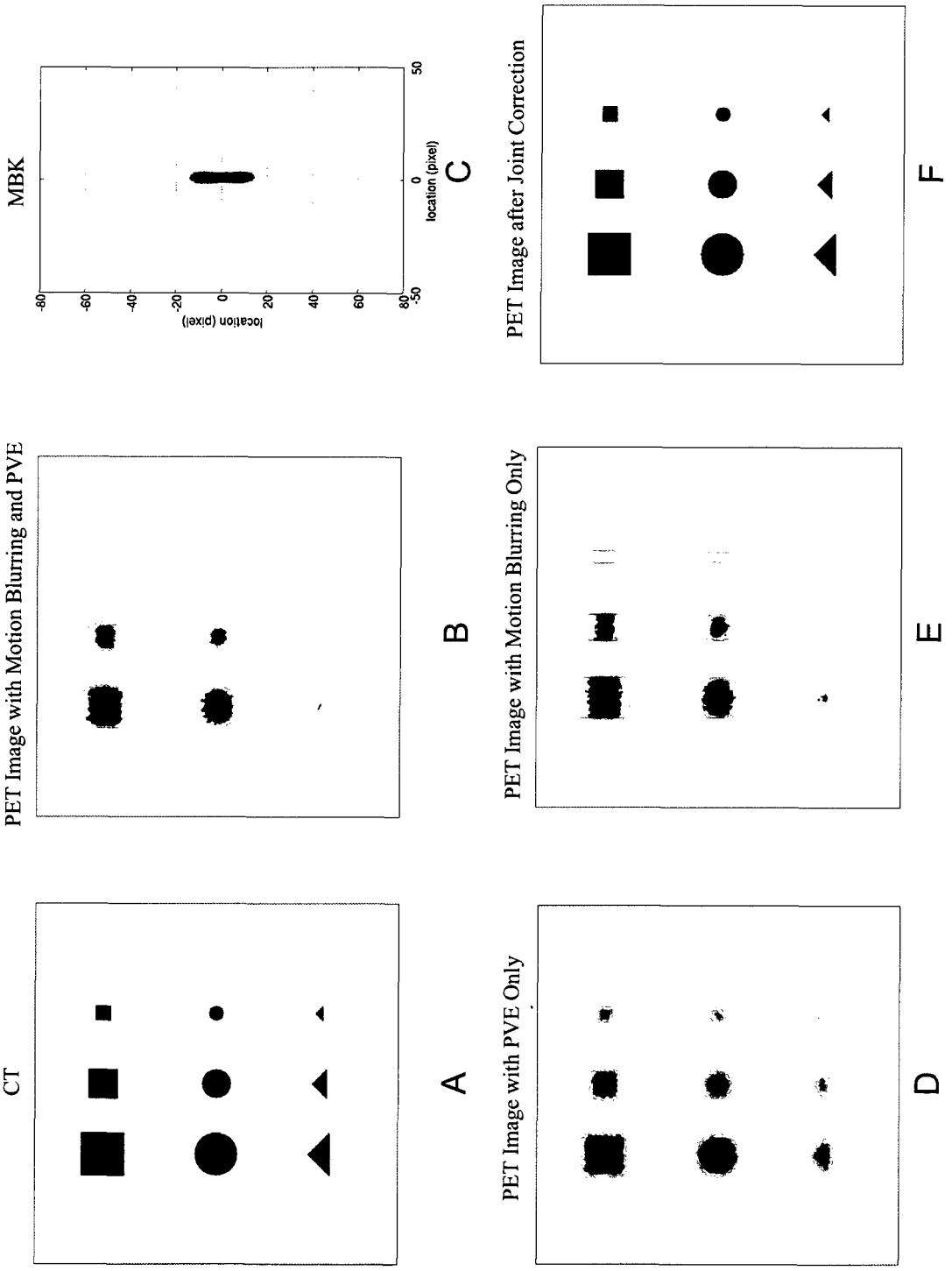

Figure 4.3: Results from the computer simulation. (A) The CT image, (B) the PET image with motion blurring and PVE, (C) the derived motion blurring kernel (MBK), (D) the PET images with PVE only, (E) the PET image with motion blurring only and (F) the PET image generated using the joint correction method.

Table 4.1
Results from the Simulation Study
(All AC data are normalized to the true AC)

Tumor Shape	Tumor Size (mm)	Activity Concentration (AC) Normalized to true AC				Correlation Coefficient between the estimated and true MBKs
		Joint Correction	PET image with PVE Only	PET image with Motion Only	PET image with Motion and PVE	
Square	30	99.7 ± 0.4 %	87.1 ± 0.3 %	81.3 ± 0.3 %	76.9 ± 0.3 %	0.93 ± 0.002
	20	100.5 ± 0.4 %	81.0 ± 0.5 %	73.1 ± 0.4 %	66.7 ± 0.4 %	0.93 ± 0.002
	10	99.2 ± 1.1 %	65.8 ± 0.8 %	49.4 ± 0.8 %	40.8 ± 0.7 %	0.95 ± 0.003
Circle	30	99.8 ± 0.3 %	86.6 ± 0.5 %	78.2 ± 0.4 %	74.6 ± 0.4 %	0.92 ± 0.003
	20	100.6 ± 0.7 %	80.0 ± 0.5 %	68.1 ± 0.5 %	62.5 ± 0.5 %	0.93 ± 0.003
	10	100.1 ± 1.1 %	61.6 ± 0.9 %	41.9 ± 0.8 %	34.4 ± 0.6 %	0.94 ± 0.005
Triangle	30	99.2 ± 0.6 %	71.6 ± 0.5 %	49.1 ± 0.5 %	46.1 ± 0.4 %	0.95 ± 0.002
	20	100.5 ± 0.8 %	60.7 ± 0.9 %	34.6 ± 0.7 %	31.9 ± 0.5 %	0.95 ± 0.006
	10	97.3 ± 1.4 %	37.7 ± 1.1 %	17.9 ± 0.8 %	14.1 ± 0.5 %	0.93 ± 0.009
Average		99.6 ± 0.7 %	70.2 ± 0.7 %	54.8 ± 0.6 %	49.8 ± 0.5 %	0.94 ± 0.004

4.3.2 Phantom Study

The PET images that had both motion blurring and PVE, PVE only and the image following the proposed joint correction method (Equation 4.3) are shown in Figure 4.4(A)-(C) respectively for both spheres (top row: 33 mm spheres, bottom row: 22 mm spheres). All the PET images are normalized to the same color scale for display. Similar to Figure 4.3(F), Figure 4.4(C) does not represent a real PET image but rather is used for reference only. Quantitative results of the AC for both spheres in all the PET images are shown in Table 4.2. This table indicates that the average AC derived from the joint correction approach approximates the true AC very well with an average difference of only 1%. The other two PET images (with PVE only and with both motion blurring and PVE) however, exhibit an average of 25% and 53% decrease in their average AC from the true values respectively.

Table 4.2
Results from the Phantom Study: Activity Concentration (AC)
(*All data are normalized to the true AC*)

	True	Joint Correction	Motion Correction Only	No Correction
Average AC (33 mm sphere)	1.00	0.99	0.77	0.52
Average AC (22 mm sphere)	1.00	0.99	0.73	0.43
Maximum AC (33 mm sphere)	N/A	N/A	0.95	0.89
Maximum AC (22 mm sphere)	N/A	N/A	0.85	0.72

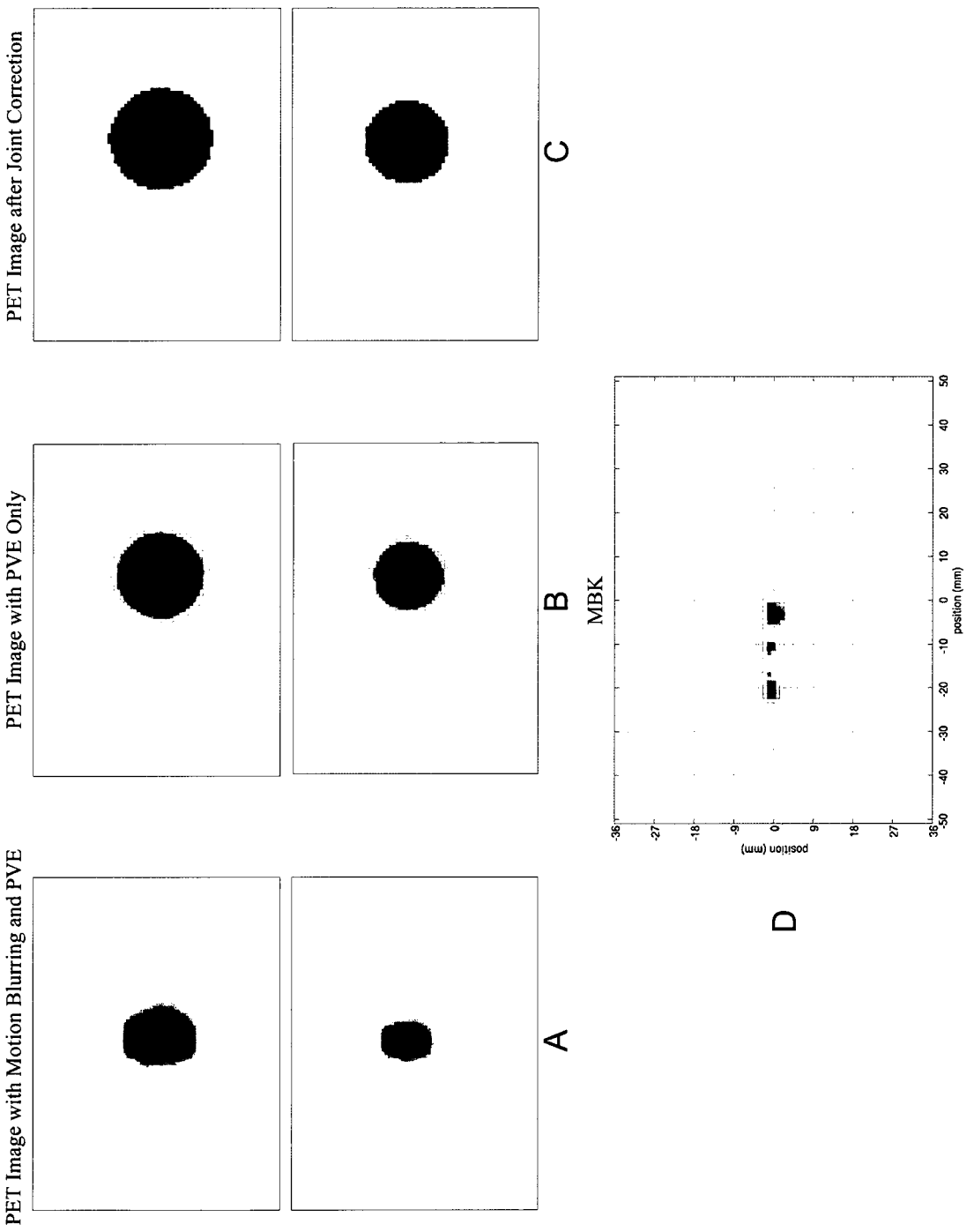

Figure 4.4: Results from the phantom study. The two spheres (top row: 33 mm and bottom row: 22 mm) on (A) the PET image with motion blurring and PVE, (B) the PET image with PVE only, and (C) the PET image generated using the joint correction method. The estimated MBK from the joint correction approach is shown in (D).

The estimated MBK from the proposed joint correction approach is displayed in Figure 4.4(D). This MBK has a 2-cm amplitude and also shows a non-uniform distribution consistent with the sinusoidal motion profile that was applied to the spheres. The correlation coefficient between the estimated and true MBK is 0.92 indicating that the estimated MBK approximates the true MBK very well.

4.4 Discussion

In this project, we proposed a novel approach to improve the accuracy of PET image quantification by jointly correcting for respiratory motion artifacts and PVE in lung/thoracic PET/CT imaging. This method incorporates a model for PVE, motion blurring and object size/shape to estimate the true tumor AC and MBK using an EM deconvolution algorithm. In order to test the performance of this approach and evaluate its ability to improve the accuracy in PET quantification, a computer simulation and a phantom study were conducted. The results from these studies showed that the corrected tumor AC on the resultant PET images and the derived MBKs approximated the true injected tumor AC and the true MBKs very well.

The proposed joint correction approach is classified among those techniques that are applied at the regional rather than the pixel level [82]. In this regard, this approach produces a corrected AC or SUV *value* rather than a corrected PET *image*. In this regard, the proposed joint correction approach should be utilized to improve the accuracy of PET lesion quantification and not to generate a corrected image that is adequate for visualization. The corrected AC or SUV value, on the other hand, can then be multiplied

by the IF (Equation 4.3) to generate a "pseudo" PET image that is both motion- and PVE-corrected. This pseudo PET image however, should only be used for quantification purposes and not for visualization

One of the main advantages of this proposed technique is that it can correct for respiratory motion artifacts and PVE without the need to acquire the patient's respiratory waveform and therefore does not necessitate the use of motion monitoring devices. Furthermore, unlike other motion correction techniques, this approach does not require a 4D CT scan and therefore does not result in high patient X-ray exposure nor require the use of deformable registration. Another advantage of this technique is that the trajectory and extent of the lesion motion (which are usually important components for radiation therapy planning using PET/CT) can be determined from the MBK, which is the by-product of the proposed approach, since it represents the probability distribution of the tumor position at a specific location. The caveat in this advantage however, is that the direction of motion can not be determined from the MBK.

Wiemker et al [88] have proposed a similar approach to correct for respiratory motion blurring and PVE in PET/CT imaging which also does not require the acquisition of the patient's motion waveform nor a 4D CT scan. Their approach however, necessitates a local registration refinement step to maximize the correlation between the PET and CT images which could be affected by the noise content in the PET images. Our proposed approach, on the other hand, does not require such a registration step but rather automatically resolves any such mismatch during the joint correction process which is represented by the probability distribution of the derived MBK. Figure 4 proves this capability by showing that although the PET and CT were acquired with a 1cm mismatch

(Figure 4D shows that the average location of the MBK has a 1cm position shift with respect to the CT), the results of the proposed joint motion and PVE correction technique can automatically resolve this mismatch accurately as shown on Figure 4.4C and table 4.2. Furthermore, the approach of Wiemker et al [88] assumes that the motion blurring in the PET image can be approximated by a Gaussian blurring function. An analysis of the patient's respiratory motion blurring functions however shows that the MBK can not be described using a Gaussian function but rather using a motion blurring function that is caused by a near-sinusoidal respiratory motion. Furthermore, since different patients have different respiratory styles and can exhibit different motion blurring effects, the MBK can not be accurately estimated unless the patient's respiratory waveform is acquired using respiratory monitoring devices. Our joint correction approach, on the other hand, does not impose any specific restrictions to represent the MBK but rather treats this MBK as an unknown in the overall-blurring equation and estimates it during the joint correction process. In this regard, this joint correction approach does not suffer from any inaccuracies in the estimation of the motion blurring function.

An implicit assumption of the proposed technique is that the true tumor volume on the PET image can be derived from the corresponding CT image. Such an assumption although debatable is the basis behind the well established and popular "recovery coefficient" approach for correcting for PVE as well as all segmentation techniques that rely on CT images to derive the PET tumor volume for PTV determination [84, 88, 91-93]. In these techniques, tumors are usually assumed to be spherical and the diameters of the tumors are estimated from CT while the uptake is assumed to be uniform throughout the tumor. This assumption allowed us to accurately delineate the tumor boundaries on

the CT rather than on the PET image to derive the IF necessary to calculate the corrected mean activity concentration and MBK. The delineation of the tumor boundary from the CT image was relatively easy to accomplish and had been automated in both of our computer simulation and phantom studies since the CT numbers of the simulated tumors or spheres were largely different from those of the background. In real clinical scans however, this process may be more difficult to achieve, especially when the lesion is attached to other organs such as the lung wall, hilum or diaphragm. In such cases, the aid of manual delineation techniques will be required and necessitate more user interaction. Techniques to achieve this task have been discussed elsewhere with various degrees of success [94-97].

In this project, no clinical studies were performed to evaluate the performance of the proposed joint correction technique, primarily due to the fact that the true tumor AC or SUV is not known a-priori. However, in order to assess the effect of the proposed approach on clinical data, the SUVs of 2 patient studies with 3 lung lesions were evaluated using the joint correction approach and the results were compared to those derived for the PET images without any correction as well as those with motion-corrected PET images using a respiratory amplitude gating approach [70]. The results from these studies showed that the tumor SUVs from the joint correction approach (7.5, 8.9 and 6.3) are higher than both of the PET images without correction (4.5, 5.4 and 3.1) and the amplitude-gated images (5.3, 6.5 and 4.0). These results suggest that the proposed joint correction approach may improve the accuracy of PET image quantification if used in clinical studies.

One simplification that was adopted for the computer simulation and the phantom study in this paper was that the motions of the tumors/spheres were defined as a 1D motion. However, our proposed joint motion-PVE joint correction method can also be applied to 2D and 3D motions with similar performance. This was confirmed using computer simulations (data not shown).

One disadvantage of the joint correction approach is that no background activity was assumed in the derivation of the overall-blurring equation. This assumption was based on the fact that the radiotracer uptake in the lung background is relatively negligible particularly in F18-FDG imaging. This assumption however, is sometimes not exactly true and might affect the accuracy of the proposed approach especially when the lesion is close to other organs with high activity concentration. One method to solve this problem is to modify the IF in the overall-blurring equation by incorporating the contributions of the surrounding tissues in the IF based on a measured tumor-to-background ratio (TBR). The measurement of TBR for lung lesion however, is also affected by the PVE and motion blurring and can not be accurately estimated before motion and PVE correction.

One limitation of the proposed approach in this paper is that the PSF used in the overall blurring equation is associated with a specific scanner and can only be used for a specific combination of reconstruction parameters: 3D OSEM, 2 iterations, 20 subsets, 256 mm FOV, 256×256 matrix size and 2-mm filtering. For other scanner models and reconstruction parameters, a different PSF has to be derived. A practical method to do this is to create PSF look-up tables corresponding to various scanner models and reconstruction parameter combinations. PSFs for reconstruction parameters that are not

part of a look-up table can then be interpolated or extrapolated from the existing data points.

Another limitation of the proposed approach is its implicit assumption that the tumor is confined to rigid motion only throughout the CT and PET data acquisitions. This assumption is necessary to ensure that the contour corresponding to the lesion segmentation form the CT image maintains its same shape and size the same on the PET image. Such an assumption is valid for solid lesions which do not undergo any deformations during the patient's respiratory cycle. For non-solid lesions however, the tumor AC will be over- or under-estimated depending on the tumor size and shape that is captured on the CT image due to its expansion or compression. This over- or under-estimation in tumor AC eventually can lead to inaccurate PET image quantification. One approach to solve this problem is to acquire phase matched CT and PET images since such a process can capture a similar tumor size and shape during the two imaging modalities. This approach however, suffers from the same problems as 4D PET/CT acquisition and therefore is not recommended in this project.

3.5 Conclusion

In this project, we proposed a joint correction approach which can simultaneously compensate for the respiratory motion artifacts and PVE in lung/thoracic PET/CT imaging. It has the potential to increase the accuracy of PET quantification and improve PET image resolution and contrast.

Chapter 5

Summary and Future Work

5.1 Summary

In this thesis, I presented techniques that can be used to compensate for respiratory motion blurring artifacts in lung/thoracic PET/CT imaging. The primary contributions of this thesis are as follows:

1. An automated respiratory amplitude gating approach is proposed in order to implement the amplitude gating technique which is current unavailable in any PET/CT scanners. This approach can automatically match the respiratory amplitude capture during CT and PET acquisition. This proposed approach does not suffer from the limitations of other existing respiratory gating techniques: increase of patient radiation exposure, inaccuracy of deformable registration, patient non-compliance problem, and extensive interaction between patients and technologists during PET/CT acquisition.
2. An in-house respiratory gating hardware/software system is designed and implemented. Compared to other commercially available device, this system is able to generate the necessary triggers while simultaneously monitoring the accumulated time within the preset amplitude range in order to facilitate the implementation of amplitude gating. This trigger generation scheme is unavailable in any other commercially available device.

3. A joint motion blurring and partial volume blurring correction approach is proposed which can improve the accuracy of PET image quantification by simultaneously eliminating the effects from the respiratory motion and PET finite spatial resolution in lung/thoracic PET/CT imaging. This joint correction approach is the first approach that simultaneously compensates for all of the following effects in one single correction process: PET-CT mismatch, PET motion blurring, and finite spatial resolution of PET scanner.

Based on these contributions, this thesis is divided into three major sections. The first section focused on the methodology design of an automated respiratory amplitude gating approach that is used in whole-body PET/CT scanners. This respiratory amplitude gating approach is referred to as the free-breathing amplitude gating (FBAG) approach. The design features of this FBAG approach include:

- This FBAG approach is used to implement the respiratory ***amplitude*** gating technique in PET/CT imaging which is currently unavailable in any PET/CT scanners, rather than ***phase*** gating approach which has already been accepted as standard gating approach in PET/CT scanners.
- This FBAG approach can automatically select a matched amplitude range (gate) during the list-mode PET scan corresponding to the respiratory motion amplitude captured during the CT scan thereby ensuring accurate attenuation correction for PET data and generation of respiration-matched PET/CT images.
- The proposed FBAG approach does not require any interaction between the patient and technologist. In this regard, the patients can breathe freely during the

entire PET/CT data acquisition and the patient's non-compliance problem in DIBH techniques is automatically resolved.

- The proposed FBAG approach does not require the acquisition of either 4-D CT scan or 4-D PET scan, therefore this approach does not increase the patient X-ray radiation exposure or require any deformable image registration methods which are characterized by inaccuracy and non-convergence.
- The proposed FBAG approach does not suffer from the baseline-drift problem of the patient's respiratory waveform which exists in all PET/CT respiratory gating approaches (phase gating and amplitude gating). This FBAG approach resolves this baseline-drift problem by using a PET-first protocol while the whole PET session is divided into two parts: regular PET and list-mode PET. The CT session is acquired following the regular PET acquisition but before the list-mode PET scan thereby ensuring the matched motion amplitude captured during CT and list-mode PET.

The performance of the proposed FBAG approach is tested and evaluated using a phantom study as well as patient studies. The results from these studies show that this proposed FBAG approach can be used to suppress the respiratory motion artifacts and improve the accuracy of PET image quantification.

The second section of this thesis focused on the hardware and software design and implementation of an in-house cost-efficient respiratory gating device. This respiratory gating device can be used to facilitate the implementation and automation of the proposed FBAG approach in the first topic. The design features of this in-house device are:

- The in-house respiratory gating device consisted of a piezo-electric respiratory transducer coupled to a National Instruments signal processing device which is under the control of an in-house Labview® software program.
- The in-house respiratory gating device can detect the patient's respiratory cycles and generate the necessary triggers corresponding to both the beginning and ending stages of a preset amplitude range while simultaneously monitoring the total accumulated time within this preset amplitude range. This trigger generation scheme is currently unavailable in any commercial respiratory gating devices.
- An in-house program is designed using C/C++ programming in order to resort the acquired PET data sequence in such a way that only the PET data acquired within the preset amplitude range can be extracted and reconstructed in order to generate an amplitude-gated PET image.
- The in-house respiratory gating device has the added advantages of low cost and simplicity. The same capabilities will require the commercially available respiratory gating devices to be interfaced to other signal processing devices in order to generate the necessary triggers to realize the FBAG approach proposed in the first section.

This in-house cost-efficient respiratory gating device has been tested using volunteer studies and a phantom study. The results from these studies show that this respiratory gating device can detect similar respiratory waveforms to commercially available devices and is able to generate the necessary triggers to facilitate the implementation of the proposed FBAG technique.

The third section of this thesis focused on the mathematical manipulation and algorithm design for a joint correction approach that can improve the accuracy of PET image quantification by simultaneously compensating for the respiratory motion artifacts and partial volume effect (PVE) in PET/CT imaging. The design features of this joint correction approach are:

- The proposed joint motion-PVE correction approach consists of a motion blurring model, a PVE blurring model and the lung/thoracic lesion size/shape. The true tumor activity concentration (AC) as well as the tumor motion blurring kernel (MBK) can be estimated by deconvolution of an overall-blurring equation.
- An expectation maximization (EM)-type algorithm is employed to deconvolve the overall-blurring equation to estimate the true tumor AC and MBK. The EM-type algorithm is specifically used in this joint correction approach to suppress the noise amplification which is a character of any deconvolution method.
- A point spread function (PSF) needs to be determined for the PET component of the PET/CT scanner before the application of the proposed joint correction approach. The determination of the PSF is based on a deconvolution method in Fourier transform space and a Gaussian fit method applied to the derived PSF image.

The performance of this proposed joint motion-PVE correction approach is tested and evaluated using computer simulations as well as a phantom study. The results from these studies show that this joint correction approach can be used in lung/thoracic PET/CT imaging to correct for both the respiratory motion artifacts and PVE simultaneously thereby improving the accuracy of PET image quantification.

5.2 Future Work

Approach to compensate for respiratory motion artifacts in PET/CT imaging remains to be a popular research topic in recently years. This is primarily due to the reason that respiratory motion artifacts can greatly affect the accuracy of quantification of PET/CT images which eventually results in inaccurate lung/thoracic cancer diagnosis, staging and evaluation of therapy responses. As can be seen from the three major sections of this thesis (Chapter 2-4), each proposed motion compensation method or technique has its own advantages but still suffers from other drawbacks or limitations. Currently there are no methods that can solve all the existing problems without introducing new limitations. In this regard, this section will focus on presenting some fresh ideas that may become future research topics in PET/CT motion compensation field.

5.2.1 Free Breath Hold Technique

The motivation of the proposed FBAG approach in Chapter 2 of this thesis is that the existing DIBH technique requires an extensive patient-technologist interaction in order to acquire the CT and PET data when the patients are holding their breath at deep inspiration. Using the proposed FBAG approach, the patients can breathe freely and no patient non-compliance problem exists any more since this technique does not require any interaction between the patients and technologist. However, this free-breathing scheme also poses a new limitation: the duty cycle of a preset amplitude range will be very low if inappropriate motion amplitudes are captured during the CT acquisition, i.e. the mid-inspiration or mid-expiration. In such cases, either insufficient amount of

coincidence events can be acquired within the preset amplitude range or longer scan duration will be required to accumulate sufficient counts (3 minutes of data).

In order to avoid capturing such inappropriate motion amplitudes during CT scan and use these motion amplitudes to select a corresponding amplitude range during the list-mode PET scan as used in the FBAG approach, a technique similar to DIBH but requires some patient training session can be proposed as follows: (1) capture the patient's respiratory motion amplitude when the patient is holding his/her breath at end-inspiration or end-expiration during the CT scan, (2) provide visual feedback to the patient during the list-mode PET acquisition and request the patient to try his/her best to repeatedly hold the breath at a similar motion amplitude level (or amplitude range) as captured during CT, (3) generate the same triggers as the FBAG approach in both the beginning and ending stages of the preset amplitude range and insert the triggers into the PET list-mode data. This technique only requires the patient's compliance during the CT acquisition rather than the whole PET/CT sessions which is required by the DIBH technique. In this regard, capturing inappropriate motion amplitude (mid-inspiration / expiration) can be avoided during the CT scan. Furthermore, although this technique requires the patient to hold his breath at a certain amplitude level either during the PET scan, there will be no trouble if the patient fails to hold his breath since triggers will be generated if the patient's respiration falls out of the preset amplitude range.

This proposed amplitude gating technique can be referred to as the "visual feedback free breath hold" or "free breath hold" since this technique does not require the patients to hold their breath for any certain amount of time but rather request them to "freely" hold their breath. As the FBAG approach, this free breath hold technique does

not require extensive interaction between the patients and technologist either but has the added advantage of higher duty cycles of the preset amplitude range since no inappropriate motion amplitude will be captured during the CT scan. Unlike the FBAG approach, this free breath hold technique does require the interaction between the patient and technologist during the CT scan. However, since the CT scan usually takes a very short time (5-15 seconds) to complete when compared to the PET scan (3 minutes/bed), we believe that this interaction does not greatly affect the implementation of this free breath hold technique. The performance of this free breath hold technique needs to be tested and evaluated using patient studies in the future.

5.2.2 Clinical Evaluation of the Joint Correction Approach

Although the proposed joint motion-PVE correction approach in Chapter 4 has been tested and evaluated using a computer simulation and a phantom study, no clinical evaluation of the performance of this approach has even been conducted. When applied to patient applications, this joint correction approach may suffer from the following problems or limitations:

- Difficulties to delineate the lung lesions from the CT image. When the lesion is attached to other organs such as lung wall, it may become difficult to segment the tumor from such organs. A GUI software can be designed to facilitate the delineation of the tumor from the CT image.
- Effects of background activity. Although the activity concentration in the lung is relatively low in FDG-PET imaging, its effect is not negligible. Removal of the

background activity can be realized by thresholding the lesion based on an estimated average activity in the background.

- Lack of gold standard. In patient studies, the true tumor activity concentration is never known, which becomes a restriction to the performance evaluation of the joint correction approach in patient studies.

Although there are several restrictions in its clinical evaluation, this proposed joint motion-PVE correction approach is prospective in both diagnostic imaging and radiation therapy applications. In diagnostic imaging especially nuclear medicine imaging, the accuracy of the quantification of nuclear medicine images can greatly affect the accuracy of lesion staging and therapy responses. Since the proposed joint correction approach can simultaneously compensate for respiratory motion artifacts and PVE, this approach will be beneficial to improve the quantification capability of nuclear medicine imaging because both of the two effects can affect the quantification accuracy of the images. In radiation therapy, this proposed joint correction approach can be beneficial for treatment planning purposes because the by-product of this approach, the MBK, can also be estimated during the joint correction process which is directly related to the tumor motion extend or trajectory. The motion extent or trajectory is an important factor in treatment planning since such an extent will be used to delineate the tumor boundary to be treated. Usually a 4-D CT scan is required to derive this tumor boundary which is characterized by increased patient exposure. In this regard, this joint correction approach has the added advantage of reducing the high patient X-ray exposure due to the acquisition of a 4-D CT scan.

Bibliography

[1] P. Price, "PET as a potential tool for imaging molecular mechanisms of oncology in man," Trends in Molecular Medicine, vol. 7, no. 10, pp. 442–446, 2001.

[2] R. Kumar, M. R. Nadig, and A. Chauhan, "Positron emission tomography: clinical applications in oncology. part 1," Expert Review of Anticancer Therapy, vol. 5, no. 6, pp. 1079–1094, 2005.

[3] R. Kumar and A. Chauhan, "Positron emission tomography: clinical applications in oncology. part 2," Expert Review of Anticancer Therapy, vol. 6, no. 4, pp. 625–640, 2006.

[4] K. Herholz and W. D. Heiss, "Positron emission tomography in clinical neurology," Molecular Imaging and Biology, vol. 6, no. 4, pp. 239–269, 2004.

[5] M. Schwaiger, S. Ziegler, and S. G. Nekolla, "PET/CT: Challenge for nuclear cardiology," Journal of Nuclear Medicine, vol. 46, no. 10, pp. 1664–1678, 2005.

[6] A. Bhatnagar, R. Hustinx, and A. Alavi, "Nuclear imaging methods for noninvasive drug monitoring," Advanced Drug Delivery Reviews, vol. 41, no. 1, pp. 41–54, 2000.

[7] S. R. Deans, The Radon Transform and Some of Its Applications. NewYork: John Wiley & Sons, 1983.

[8] F. Natterer and F.Wˆubbeling, Mathematical Methods in Image Reconstruction. SIAM: Society for Industrial and Applied Mathematics, 2001.

[9] T. Kauppinen, M. O. Koskinen, S. Alenius, E. Vanninen, and J. T. Kuikka, "Improvement of brain perfusion SPECT using iterative reconstruction with

scatter and non-uniform attenuation correction," European Journal of Nuclear Medicine, vol. 27, no. 9, pp. 1380–1386, 2000.

[10] E. Etchebehere, H. A. Macapinlac, M. Gonen, J. Humm, H. W. D. Yeung, T. Akhurst, H. I. Scher, and S. M. Larson, "Qualitative and quantitative comparison between images obtained with filtered back projection and iterative reconstruction in prostate cancer lesions on F-18-FDG PET," Quarterly Journal of Nuclear Medicine, vol. 46, no. 2, pp. 122–130, 2002.

[11] C. T. Mesina, R. Boellaard, G. Jongbloed, A. W. van der Vaart, and A. A. Lammertsma, " Experimental evaluation of iterative reconstruction versus filtered back projection for 3D [O-15]water PET activation studies using statistical parametric mapping analysis," Neuroimage, vol. 19, no. 3, pp. 1170–1179, 2003.

[12] H. H. Barrett and K. Myers, Foundations of Image Science. Wiley-Interscience, 2003.

[13] J. Qi, R. M. Leahy, S. R. Cherry, A. Chatziioannou, and T. H. Farquhar, "High resolution 3D bayesian image reconstruction using the microPET small animal scanner," Physics in Medicine and Biology, vol. 43, no. 4, pp. 1001–1013, 1998.

[14] J. Qi, R. M. Leahy, C. Hsu, T. H. Farquhar, and S. R. Cherry, "Fully 3D bayesian image reconstruction for the ECAT EXACT HR+," IEEE Trans. Nucl. Sci., vol. 45, no. 3, pp. 1096–1103, Jun. 1998.

[15] R. M. Leahy and J. Y. Qi, "Statistical approaches in quantitative positron emission tomography," Statistics and Computing, vol. 10, no. 2, pp. 147–165, 2000.

[16] L. A. Shepp and Y. Vardi, "Maximum likelihood reconstruction for emission tomography," IEEE Trans. Med. Imag., vol. 1, no. 2, pp. 113–122, 1982.

[17] H. M. Hudson and R. S. Larkin, "Accelerated image reconstruction using ordered subsets of projection data," IEEE Trans. Med. Imag., vol. 13, pp. 601–609, 1994.

[18] C. L. Byrne, "Convergent block-iterative algorithms for image reconstruction from inconsistent data," IEEE Trans. Image Processing, vol. 6, no. 9, pp. 1296–1304, 1997.

[19] Charles L. Byrne, "Accelerating the EMML algorithm and related iterative algorithms by rescaled block-iterative methods," IEEE Trans. Image Processing, vol. 7, no. 1, pp. 100–109, 1998.

[20] J. A. Sercarz, J. W. Bailet, E. Abemayor, Y. Anzai, C. K. Hoh, and R. B. Lufkin, "Computer coregistration of positron emission tomography and magnetic resonance images in head and neck cancer," American Journal of Otolaryngology, vol. 19, no. 2, pp. 130–135, 1998.

[21] Miles N. Wernick and John N. Aarsvold, "Emission Tomography," Chapter 10, pp. 179–194, 2004.

[22] F. J. Lagerwaard, J. R. V. de Koste, M. R. J. Nijssen-Visser, R. H. Schuchhard-Schipper, S. S. Oei, A. Munne, and S. Senan, "Multiple 'slow' CT scans for

incorporating lung tumor mobility in radiotherapy planning," International Journal of Radiation Oncology Biology Physics, vol. 51, no. 4, pp. 932–937, 2001.

[23] T. Pan, O. Mawlawi, D. Luo, H. Liu, P. C. M. Chi, M. V. Mar, G. Gladish, M. Truong, J. Erasmus, Z. Liao, and H. A. Macapinlac, "Attenuation correction of PET cardiac data with low-dose average CT in PET/CT," Med. Phys., vol. 33, no. 10, pp. 3931–3938, 2006.

[24] F. J. Lagerwaard, J. R. V. de Koste, M. R. J. Nijssen-Visser, R. H. Schuchhard-Schipper, S. S. Oei, A. Munne, and S. Senan,"Multiple 'slow' CT scans for incorporating lung tumor mobility in radiotherapy planning," International Journal of Radiation Oncology Biology Physics, vol. 51, no. 4, pp. 932–937, 2001.

[25] T. Pan, O. Mawlawi, D. Luo, H. Liu, P. C. M. Chi, M. V. Mar, G. Gladish, M. Truong, J. Erasmus, Z. Liao, and H. A. Macapinlac, "Attenuation correction of PET cardiac data with low-dose average CT in PET/CT," Med. Phys., vol. 33, no. 10, pp. 3931–3938, 2006.

[26] Y. Picard and C. J. Thompson, "Motion correction of PET images using multiple acquisition frames," IEEE Trans. Med. Imag., vol. 16, pp. 137–144, 1997.

[27] O. Mawlawi, "A method for correcting head motion artifact in positron emission tomography," Ph.D. dissertation, Columbia University, 1998.

[28] G. Klein, B. Reutter, and R. Huesman, "Four-dimensional affine registration models for respiratory-gated PET," IEEE Trans. Nucl. Sci., vol. 48, no. 3, pp. 756–760, Jun. 2001.

[29] M. Dawood, F. Buther, N. Lang, O. Schober, and K. P. Schafers, "Respiratory gating in positron emission tomography: A quantitative comparison of different

gating schemes," Med. Phys., vol. 34, no. 7, pp. 3067–3075, 2007

[30] D. S. Lalush, L. Cui, and B. M. W. Tsui, "A priori motion models for fourdimensional reconstruction in gated cardiac SPECT," in 1996 IEEE Nuclear Science Symposium Conference Record, vol. 3, Nov. 1996, pp. 1923–1927.

[31] J. Qi and R. H. Huesman, "List mode reconstruction for PET with motion compensation: A simulation study," in Proc. IEEE Int. Symp. Biological Imaging, 2002, pp. 413–416.

[32] D. R. Gilland, B. A. Mair, J. E. Bowsher, and R. J. Jaszczak, "Simultaneous reconstruction and motion estimation for gated cardiac ECT," IEEE Trans. Nucl. Sci., vol. 49, no. 5, pp. 2344–2349, Oct. 2002.

[33] Z. Cao, D. R. Gilland, B. A. Mair, and R. J. Jaszczak, "Three-dimensional motion estimation with image reconstruction for gated cardiac ECT," IEEE Trans. Nucl. Sci., vol. 50, no. 3, pp. 384–388, Jun. 2003.

[34] M. W. Jacobson and J. A. Fessler, "Joint estimation of image and deformation parameters in motion-corrected PET," in Proc. IEEE Nucl. Sci. Symp. Med. Imag. Conf., vol. 5, 2003, pp. 3290–3294.

[35] D. R. Gilland, B. A. Mair, and J. Sun, "Joint 4D reconstruction and motion estimation in gated cardiac ECT," in Proc. Intl. Mtg. on Fully 3D Image Recon. in Rad. and Nuc. Med, 2005, pp. 303–306.

[36] E. Gravier and Y. Yang, "Motion-compensated reconstruction of tomographic image sequences," IEEE Trans. Nucl. Sci., vol. 52, no. 1, pp. 51–56, Feb. 2005.

[37] S. A. Nehmeh, Y. E. Erdi, G. S. P. Meirelles, et al, "Deep-inspiration breath-hold PET/CT of the thorax," J. Nucl. Med., vol. 48, no. 1, pp. 22–26, 2007

[38] G. S. P. Meirelles, Y. E. Erdi, S. A. Nehmeh, et al, "Deep-inspiration breath-hold PET/CT: clinical findings with a new technique for detection and characterization of thoracic lesions," J. Nucl. Med., vol. 48, no. 5, pp. 712–719, 2007

[39] T. Kawano, E. Ohtake, and T. Inoue, "Deep-inspiration breath-hold PET/CT of lung caner: maximum standardardized uptake value analysis of 108 patients," J. Nucl. Med., vol. 49, no. 8, pp. 1223–1231, 2008

[40] P. J. Keall, G. S. Mageras, J. M. Balter, et al, "The management of respiratory motion in radiation oncology report of AAPM Task Group 76," Med. Phys., vol. 33, no. 10, pp. 3874–3900, 2006

[41] E. J. Hoffman, S. C. Huang and M. E. Phelps, "Quantitation in positron emission computed tomography: 1. Effect of object size," J. Comput. Assist. Tomogr., vol.3, pp. 299–308, 1979.

[42] E. J. Hoffman, S. C. Huang, D. Plummer and M. E. Phelps, "Quantitation in positron emission computed tomography: 6. Effect of nonuniform resolution," J. Comput. Assist. Tomogr., vol.6, pp. 987–999, 1982.

[43] R. M. Kessler, J. R Ellis and M. Eden, "Analysis of emission tomographic scan data: limitations imposed by resolution and background," J. Comput. Assist. Tomogr., vol.8, pp. 514–522, 1984.

[44] K. Baete, J. Nuyts, K. Van Laere et al, "Evaluation of anatomy based reconstruction for partial volume correction in brain FDG-PET," Neuroimage, vol. 23, pp. 305–317, 2004.

[45] J. Nuyts, A. Maes, M. Vrolix et al, "Three-dimensional correction for spillover and recovery of myocardial PET images," J. Nucl. Med., vol. 37, pp. 767–774, 1996.

[46] H. R. Tang, A. J. Da Silva, K. K. Matthay et al, "Neuroblastoma imaging using a combined CT scanner-scintillation camera and ^{131}I-MIBG," J. Nucl. Med., vol. 42, pp. 237–247, 2001

[47] L. Geworski, B. O. Knoop, M. L. de Cabrejas, W. H. Knapp and D. L. Munz, "Recovery correction for quantitation in emission tomography: a feasibility study," Eur. J. Nucl. Med., vol. 27, pp. 191–169, 2000

[48] D. Lardinois, W. Weder, T. F. Hany TF, et al, "Staging of non-small-cell lung cancer with integrated positron-emission tomography and computed tomography," N. Engl. J. Med., vol. 348, pp. 2500–2507, 2003

[49] H. Schoder, S. M. Larson, H. W. Yeung, "PET/CT in oncology: integration into clinical management of lymphoma, melanoma, and gastrointestinal malignancies," J. Nucl. Med., vol. 45(suppl. 1), pp. 72–81, 2004

[50] G. K. von Schulthess, "Positron emission tomography versus positron emission tomography/computed tomography: from 'unclear' to 'new-clear' medicine," Mol. Imaging Biol., vol. 6, pp. 183–187, 2004

[51] P. E. Kinahan, D. W. Townsend, T. Beyer and D. Sashin, "Attenuation correction for a combined 3D PET/CT scanner," Med. Phys., vol. 25, no. 10, pp. 2046–2053, 1998

[52] T. Beyer, G. Antoch, S. Muller, et al, "Acquisition protocol considerations for combined PET/CT imaging," J. Nucl. Med., vol. 45(suppl 1), pp. 25S–35S, 2004

[53] T. M. Blodgett, B. M. McCook, and M. P. Federle, "Positron emission tomography/computed tomography: protocol issues and options," Semin. Nucl. Med., vol. 36, pp. 157–168, 2006

[54] O. R. Mawlawi, S. C. Kappadath, T. Pan, E. Rohren, and H. A. Macapinlac, "Factors Affecting Quantification in PET/CT Imaging," Current Med. Imag. Rev., vol. 4, no. 1, pp. 34–45, 2008

[55] I. Sarikaya, H. W. Yeung, Y. Erdi, and S. M. Larson, "Respiratory artefact causing mal-positioning of liver dome lesion in right lower lung," Clin. Nucl. Med., vol. 28, pp. 943–944, 2003

[56] S. A. Nehmeh, Y. E. Erdi, C. C. Ling, et al, "Effects of respiratory gating on quantifying PET images of lung cancer," J. Nucl. Med., vol. 43, pp. 876–881, 2002

[57] Y. E. Erdi, S. A. Nehmeh, T. Pan T, et al, "The CT motion quantitation of lung lesions and its impact on PET-measured SUVs," J. Nucl. Med., vol. 45, pp. 1287–1292, 2004

[58] S. A. Nehmeh, and Y. E. Erdi, "Respiratory motion in positron emission tomography/computed tomography: a review," Semin. Nucl. Med., vol. 38, pp. 167–176, 2008

[59] L. Boucher, S. Rodrigue, R. Lecomte, and F. Benard, "Respiratory gating for 3-dimensional PET of the thorax: feasibility and initial results," J. Nucl. Med., vol. 45, no. 2, pp. 214–219, 2004

[60] I. E. Naqa, D. A. Low, J. D. Bradley, M. Vicic, and J. O. Deasy, "Debluring of breathing motion artifacts in thoracic PET images by deconvolution methods," Med. Phys, vol. 33, no. 10, pp. 3587–3600, 2006

[61] F. Lamare, T. Cresson, J. Savean, et al, "Respiratory motion correction for PET oncology applications using affine transformation of list mode data," Phys. Med. Biol., vol. 52, pp. 121–140, 2007

[62] R. A. Bundschuh, A. Martinez-Moller, M. Essler, S. G. Nekolla, S. I. Ziegler, and M. Schwaiger, "Local motion correction for lung tumors in PET/CT – first results," Eur. J. Nucl. Med. Mol. Imaging, vol. 35, no. 11, pp. 1981–1988, 2008

[63] G. M. P. Masselli, "Design and evaluation of a methodology to perform personalized visual biofeedback for reducing respiratory amplitude in radiation treatment", Med. Phys., vol. 36, no. 5, pp. 1467-1472, 2009

[64] G. J. Klein, B. W. Reutter, M. H. Ho, J. H. Reed, and R. H. Huesman, "Real-time system for respiratory-cardiac gating in position tomography," IEEE Trans. Nucl. Sci., vol. 45, pp. 2139–2143, 1998

[65] K. P. Schafers and L. Stegger, "Combined imaging of molecular function and morphology with PET/CT and SPECT/CT: image fusion and motion correction," Basic Res. Cardiol., vol. 103, pp. 191–199, 2008

[66] T. Li, B. Thorndyke, E. Schreibmann, Y. Yang, and L. Xing, "Model-based image reconstruction for four-dimensional PET," Med. Phys., vol. 33, no. 5, pp. 1288–1298, 2006

[67] F. Qiao, T. Pan, J. W. Clark, and O. R. Mawlawi, "A motion-incorporated reconstruction method for gated PET studies," Phys. Med. Biol., vol. 51, pp. 3769–3783, 2006

[68] B. J. Kemp, C. Kim, J. J. Williams, A. Ganin, and V. J. Lowe, "NEMA NU 2-2001 performance measurements of an LYSO-based PET/CT system in 2D and 3D acquisition modes," J. Nucl. Med., vol. 47, no. 12, pp. 1960–1967, 2006

[69] M. J. Fitzpatrick et al, "A novel platform simulating irregular motion to enhance assessment of respiration-correlated radiation therapy procedures," J. of Applied Clinical Med. Phys., vol. 6, no. 1, pp. 13–21, 2005

[70] G. Chang, T. Chang, T. Pan, J. W. Clark, and O. R. Mawlawi, "Implementation of an automated respiratory amplitude gating technique for PET/CT imaging: clinical evaluation," J. Nucl. Med., vol. 51, no. 1, pp. 16–24, 2010

[71] Available at http://www.adinstruments.com/products/product.php?id=MLT1132

[72] Available at http://sine.ni.com/nips/cds/view/p/lang/en/nid/202545

[73] Available at http://sine.ni.com/nips/cds/view/p/lang/en/nid/14166

[74] M. Dawood, F. Buther, L. Stegger, X. Jiang, O. Schober, M. Schafers and K. Schafers, "Optimal number of respiratory gates in positron emission tomography: A cardiac patient study," Med. Phys., vol. 36, no. 5, pp. 1775–1784, 2009

[75] G. Chang, T. Chang, T. Pan, E. Rohren, J. W. Clark, and O. R. Mawlawi, "Automation of Respiratory Amplitude Gating in Whole-body (WB) PET/CT Imaging," J. Nucl. Med., vol. 50(Supplement 2), pp. 15P, 2009

[76] G. Chang, T. Chang, J. Jackson, J. W. Clark, and O. R. Mawlawi, "Performance Comparison of an In-house and a Commercially Available Amplitude Gating Device for PET imaging," Med. Phys., vol. 36, no. 6, pp. 2469, 2009

[77] G. Chang, T. Chang, J. W. Clark, and O. R. Mawlawi, "A Cost-Efficient Respiratory Amplitude Gating Device for PET/CT Imaging," J. Nucl. Med., vol. 50(Supplement 2), pp. 311P, 2009

[78] G. Chang, T. Pan, J. W. Clark Jr, and O. R. Mawlawi, "Feasibility of Implementing Amplitude Gating in PET Imaging Using a Commercial Respiratory Gating Device," IEEE Med. Imag. Conference Record, M10–410, 2008

[79] G. Chang, T. Pan, J. W. Clark, Jr. and O. R. Mawlawi, "A low cost prospective amplitude gating device for PET imaging," J. Nucl. Med., vol. 49(Supplement 1), pp. 410P, 2008

[80] I. Sarikaya, H. W. Yeung, Y. Erdi, S. M. Larson, "Respiratory artefact causing malpositioning of liver dome lesion in right lower lung," Clin. Nucl. Med., vol. 28, pp. 943-944, 2003

[81] O. G. Rousset, Y. Ma, A. C. Evans, "Correction for partial volume effects in PET: principles and validation," J. Nucl. Med., vol. 39, pp. 904-911, 1998

[82] M. Soret, S. L. Bacharach, I. Buvat, "Partial-volume effect in PET tumor imaging," J. Nucl. Med., vol. 48, pp. 932-945, 2007

[83] B. Thorndyke, E. Schreibmann, A. Koong, and L. Xing, "Reducing respiratory motion artifacts in positron emission tomography through retrospective stacking," Med. Phys., vol. 33, pp. 2632-2641, 2006

[84] H. Vesselle, R. A. Schmidt, J. M. Pugsley, et al, "Lung cancer proliferation correlates with [F-18]fluorodeoxyglucose uptake by positron emission tomography," Clin. Cancer Res., vol. 6, pp. 3837-3844, 2000

[85] V. Frouin, C. Comtat, A. Reilhac, M. C. Gregoire, "Correction of partial-volume effect for PET striatal imaging: fast implementation and study of robustness," J. Nucl. Med., vol. 43, pp. 1715-1726, 2002

[86] B. K. Teo, Y. Seo, S. L. Bacharach, et al, "Partial-volume correction in PET: validation of an iterative postreconstruction method with phantom and patient data," J. Nucl. Med., vol. 48, pp. 802-810, 2007

[87] D. C, Yu, S. C. Huang, S. T. Grafton, et al, "Methods for improving quantification of putamen uptake constant of FDOPA in PET studies," J. Nucl. Med., vol. 34, pp. 679-688, 1993

[88] R. Wiemker, T. Paulus, S. Kabus, et al, "Combined motion blur and partial volume correction for computer aided diagnosis of pulmonary nodules in PET/CT," Int. J. CARS, vol. 3, pp. 105-113, 2008

[89] M. A. Lodge, A. Rahmin, R. L. Wahl, "A practical, automated quality assurance method for measuring spatial resolution in PET," J. Nucl. Med, vol. 50, pp. 1305-1314, 2009

[90] J. A. Fessler. Image reconstruction toolbox [Online]. Available at website: http://www.eecs.umich.edu/fessler/code.

[91] M. Hickeson, M. Yun, A. Matthies, H. Zhuang, L. E. Adam, L. Lacorte, and A. Alavi, "Use of a corrected standardized uptake value based on the lesion size on

CT permits accurate characterization of lung nodules on FDG-PET," Eur. J. Nucl. Med. Mol. Imaging, 29(12), 1639-1647, 2002.

[92] S. Basu and A. Alavi, "Feasibility of Automated Partial-Volume Correction of SUVs in Current PET/CT Scanners: Can Manufacturers Provide Integrated, Ready-to-Use Software?" J. Nucl. Med, 49(6), 1031-1032, 2008.

[93] S. M. Srinivas, T. Dhurairaj, S. Basu, G. Bural, S. Surti, and A. Alavi, "A recovery coefficient method for partial volume correction of PET images," Ann. Nucl. Med, 23(4), 341-348, 2009.

[94] M. Kakar, D. Olsen, "Automatic segmentation and recognition of lungs and lesion from CT scans of thorax," Compu Med Imag and Graph, vol. 33, no. 1, pp. 72-82, 2009

[95] C. C. McCullock, R. A. Kaucic, P. R. S. Mendonca, D. J. Walter, R. S. Avila, "Model-based detection of lung nodules in computed tomography exams: thoracic computer-aided diagnosis," Academic Radiology, vol. 11, no. 3, pp. 258-266, 2004

[96] B. Buerke, M. Puesken, G. Beyer et al. "Semiautomatic lymph node segmentation in multislice computed tomography: impact of slice thickness on segmentation quality, measurement precision, and interobserver variability," Investigative Radiology, vol. 45, no. 2, pp. 82-88, 2010

[97] K. Suzuki, "Segmentation of lesions with improved specificity in computer-aided diagnosis using a massive-training artificial neural network (MTANN)," Proc of the 2008 7th Int Conf on Machine Learning and App, pp. 523-527, 2008